2016-12-01

Structural Analysis of Cell Signaling Complexes

Takuma Aoba
Brigham Young University

BYU ScholarsArchive Citation

Aoba, Takuma, "Structural Analysis of Cell Signaling Complexes" (2016). *All Theses and Dissertations*. 6583.
https://scholarsarchive.byu.edu/etd/6583

Structural Analysis of Cell Signaling Complexes

Takuma Aoba

A dissertation submitted to the faculty of
Brigham Young University
in partial fulfillment of the requirements for the degree of

Doctor of Philosophy

Barry M. Willardson, Chair
Gregory F. Burton
Joshua L. Andersen
Kenneth A. Christensen
Joshua L. Price

Department of Chemistry and Biochemistry

Brigham Young University

ABSTRACT

Structural Analysis of Cell Signaling Complexes

Takuma Aoba
Department of Chemistry and Biochemistry, BYU
Doctor of Philosophy of Science

Bardet-Biedl syndrome (BBS) is a rare genetic disease that causes retinal degradation, obesity, kidney dysfunction, polydactyly, and other cilium-related disorders. To date, more than 20 BBS genes, whose mutants cause BBS phenotypes, have been identified, and eight of those (BBS1-2, 4-5, 7-9, and 18) are known to form the BBSome complex. Recent studies have revealed that the BBSome is closely involved in the trafficking of signaling proteins in the primary cilium. Mutations in BBS genes are highly pathogenic because trafficking in the primary cilium is not fully functional when BBS mutations impair assembly of the BBSome. However, the functional links between onset of BBS and BBSome assembly are not well understood. To address this gap in knowledge, we examined the structure of a BBSome assembly intermediate, the BBSome core complex (BBS2, 7, and 9). We employed a combination of chemical crosslinking coupled with mass spectrometry (XL-MS) and electron microscopy (EM) to determine the structure. We applied this structural information to BBS mutations in the core complex to understand how these mutations might cause the disease. These results provide the first structural model of the BBSome core complex and give insight into the molecular basis of Bardet-Biedl syndrome.

We have also investigated the mechanism of assembly of the two mTOR kinase complexes (mTORC1 and 2). mTOR is a master regulator of cell metabolism, growth and proliferation. As such, mTOR is a high-value drug target. We investigated the mechanism of assembly of these mTOR complexes and found that the cytosolic chaperonin CCT contributes to mTOR signaling by assisting in the folding of mLST8 and Raptor, components of mTORC1 and mTORC2. To understand the function of CCT in mTOR complex assembly at the molecular level, we have isolated the mLST8-CCT complex and performed a structural analysis using chemical cross-linking couple with mass spectrometry (XL-MS) and cryogenic EM. We found that mLST8 binds CCT deep in its folding cavity, making specific contacts with the CCTα and γ subunits and forming a near-native β-propeller conformation. This information can be used to develop new therapeutics that regulate mTOR activity by controlling mTOR complex assembly.

Keywords: BBS, primary cilia, BBSome core complex, EM, XL-MS, CCT, mTORC, PhLP1

ACKNOWLEDGEMENTS

I extend much appreciation to Dr. Willardson, who was insightful and a great mentor throughout my graduate studentship. Besides his responsibility as a professor of biochemistry, advisor of many other students, and principal investigator, he sacrificed a significant amount of time helping me compose and refine the present dissertation. Other members of his lab, Grant Ludlum and Madhura Dhavale made significant contribution to the findings presented herein as well. It is certain that I would not have been able to accomplish this work without collaboration of José Valpuesta's lab at the Centro Nacional de Biotecnología in Madrid and Sarah Franklin's lab at the University of Utah.

I would like to give my deepest gratitude to my daughters and my wife, Akiko, who were always faithful, patient, and supportive in unaccustomed cultures during my graduate research.

TABLE OF CONTENTS

TITLE PAGE i

ABSTRACT ii

ACKNOWLEDGEMENTS iii

TABLE OF CONTENTS iv

LIST OF FIGURES vii

ABBREVIATIONS viii

CHAPTER 1: BBS AND BBSOME 1

- Summary 1
- Introduction 2
  - Bardet-Biedl syndrome 2
  - BBS genes 3
  - Cilium as cellular antenna 4
  - Physiological role of the BBSome 6
  - Assembly of the BBSome 9
  - Homology between BBSome core subunits and COP proteins 11
  - Cryogenic electron microscopy 12
  - Chemical crosslinking coupled with mass spectrometry 12
  - Unnatural amino acid photo-crosslinking 15
- Conclusion 17

CHAPTER 2: STRUCTURAL ANALYSIS OF THE BBSOME CORE COMPLEX 19

- Summary 19
- Introduction 20
- Methods 22
  - Purification of the BBSCC 22
  - Crosslinking coupled with mass spectrometry 23
  - Mass spectrometry 24
  - XL-MS analysis 25
  - Unnatural amino acid crosslinking 25
  - Mutagenesis 27
  - Protein separation for EM sampling 28

EM grid preparation and data collection 28
Image processing, particle selection and 2D classification 29
3D reconstruction 29
Generating a structural model 29
Results 30
Purification of the BBSCC 30
Electron microscopy 31
Structures of BBS2, 7, and 9 domains 32
BBS2 and BBS7 interact through a coiled-coil domain 34
Structural model of the BBS2-BBS7 dimer 37
Structural model of the BBSCC 39
Effects of BBS-linked mutations 40
Discussion 43
CHAPTER 3: MTOR SIGNALING AND MTORC ASSEMBLY 45
Summary 45
Introduction 46
mTOR signaling 46
mTORC1 and mTORC2 47
The mTOR kinase 47
mLST8 51
mTORC1 components 51
mTORC2 components 52
mTORC1 signaling 53
mTORC2 signaling 55
Chaperones and mTORC assembly 56
CCT—possible chaperone for mTORC components 57
mTOR signaling and CCT 58
CCT 58
PhLP1 as a co-chaperone of CCT 61
Conclusion 61
CHAPTER 4: MTORC FOLDING AND ASSEMBLY 63
Summary 63
Introduction 64

Methods 66
- Purification of the mLST8-CCT, PhLP1-mLST8-CCT, and Raptor-CCT complex 66
- Cryo-EM 67
- Transfection, immunoprecipitation, and immunoblotting 68
- siRNA knockdown 69
- CRISPR knockdown 69
- Ubiquitin assay 70
- Insulin signaling 70

Results 70
- mLST8 forms a ternary complex with CCT and PhLP1 70
- Raptor interacts with CCT and PhLP1 72
- CCT is required for assembly of mTORC1 and mTORC2 75
- PhLP1 contributes to mTORC1 assembly 77
- Contributions of CCT and PhLP1 on mTOR signaling 78
- PhLP1 contributes to Raptor degradation 80
- Purification of mLST8-CCT and PhLP1-mLST8-CCT for structural analysis 81
- Cryo-EM analysis of mLST8-CCT and PhLP1-mLST8-CCT 81
- XL-MS analysis of mLST8-CCT 83

Discussion 85
- Role of CCT in mLST8 and Raptor folding 85
- Functional implications of the mLST8-CCT structure 86
- Scheme for CCT-dependent mTOR complex assembly 87
- Role of PhLP1 in mLST8 and Raptor folding 88

Conclusion 89

REFERENCES 91

LIST OF FIGURES

Figure 1.1 The model of BBSome mediated IFT process in primary cilia....................................8
Figure 1.2 Assembly of the BBSome 10
Figure 1.3 XL-MS work scheme 14
Figure 1.4 The methodology of UAA-XL 17
Figure 2.1 Purification and EM reconstruction of the BBSCC 31
Figure 2.2 Domain structural model of the components of the BBSCC 33
Figure 2.3 Specific interaction between BBS2 and BBS7..36
Figure 2.4 BBS2-BBS7 dimer 38
Figure 2.5 The structure of the BBSCC..41
Figure 2.6 Effects of mutations on BBSome core assembly 42
Figure 3.1 Structures and domain maps of mTORC components 50
Figure 3.2 The mTOR signaling pathway...55
Figure 3.3 Architecture of CCT 60
Figure 4.1 PhLP1 and mLST8 form a ternary complex with CCT..72
Figure 4.2 Raptor independently binds CCT and PhLP1 74
Figure 4.3 CCT contributes to mTORC formation...76
Figure 4.4 PhLP1 contributes to mTORC1 formation..78
Figure 4.5 Effects of depletion of CCT and PhLP1 on mTORC1 and mTORC2 signaling.........79
Figure 4.6 PhLP1 facilitates Raptor degradation..80
Figure 4.7 Purification of the PhLP1-mLST8-CCT and mLST8-CCT complexes 82
Figure 4.8 Cryo-EM analysis of the mLST8-CCT and PhLP1-mLST8-CCT complexes............83
Figure 4.9 Structural comparison of Gβ-CCT and mLST8-CCT 84
Figure 4.10 CCT contributes to mTOR signaling..88

ABBREVIATIONS

2D	two dimensional
3D	three dimensional
40S	eukaryotic small ribosomal subunit
4EBP	eukaryotic translation factor 4E binding protein
α-helix	protein secondary structure motif of a right-handed coil
ADP	adenosine diphosphate
AGC group	group of protein kinases including PKA, PKG, and PKC
AKT	Ak virus strain thymoma protein, also called protein kinase B
AMPK	adenosine monophosphate kinase
ARL6	ADP-ribosylation factor-like protein 6, also called BBS3
ATM	ataxia telangiectasia mutated
ATP	adenosine triphosphate
ATR	ataxia- and Rad3-related
β-propeller	protein tertiary structure motif of 4-8 β-sheets that form a toroid
β-sheet	protein secondary structure motif of extended residues held adjacent and in a planar conformation by hydrogen bonds between backbone atoms
BBS	Bardet-Biedl syndrome
BBSCC	BBSome core complex
BBSome	protein complex consists of BBS1-2, 4-5, 7-9, and 18
BzF	p-benzoyl-L-phenylalanine
C-terminus	amino acids at the protein carboxyl terminus
Cas9	CRISPR associated protein 9
CCD	charge coupled device
CCT	chaperonin containing tailless polypeptide 1, also called TRiC
cDNA	complementary DNA
CHAPS	3-[(3-cholamidopropyl)dimethylammonio]-1-propanesulfonate
CL-BBS	chaperonin like BBS complex
c-Myc	avian myelocytomatosis virus oncogene cellular homolog
COP	coat protein

CRIM	conserved domain in middle
CRISPR	clustered regularly interspaced short palindromic repeats
CTF	contrast transfer function
D	deuterium
D-1	dopamine receptor 1
DEPTOR	DEP domain-containing mTOR-interacting protein
DNA	deoxyribonucleic acid
DNA-PKcs	DNA-dependent protein kinase catalytic subunit
DSG	disuccinimidyl glutetate
DSS	disuccinimidyl suberate
DTT	dithiothreitol
EDTA	ethylenediaminetetraacetic acid
eEF	eukaryotic translation elongation factor
eIF	eukaryotic translation initiation factor
EM	electron microscopy
ERK	extracellular signal-required kinase
FAT	FRAP, ATM, TRRAP
FATC	FAT domain at C-terminus
FBS	fetal bovine serum
FSC	Fourier shell coefficient
G protein	guanine nucleotide binding signaling protein
GAE	γ-adaptin ear
GAPDH	glyceraldehyde 3-phosphate dehydrogenase
GβL	Gβ-like, also called mLST8
GC	guanylyl cyclase
GFP	green fluorescent protein
Gβ	G protein β subunit
Gγ	G protein γ subunit
GLI	protein related to human glioblastoma
GPCR	G protein coupled receptor
GSK3β	glycogen synthase kinase 3 β

GTP	guanosine triphosphate
GTPase	enzyme that hydrolyzes GTP to GDP
HA	hemagglutinin
HEAT	Huntingtin, EF3A, ATM, TOR
HEK	human embryonic kidney
HEPES	4-(2-hydroxyethyl)-1-piperazineethanesulfonic acid
HEPG2	liver hepatocellular carcinoma
H	hydrogen
Hh	hedgehog
His_6	hexahistidine
HPC4	Ca^{2+}-dependent protein C epitope
HSC	heatshock cognate
HSP	heatshock protein
IFT	intraflageller transport
IGF	insulin-like growth factor
JNK	c-Jun N-terminal kinase
KD	kinase domain
Kif-7	kinesin family member 7
LBE	LST binding element
LCA	Leber Congenital Amaurosis
LC-MS/MS	liquid chromatography followed by tandem mass spectrometry
LTQ	linear ion trap quadrupole
LZTFL1	leucine zipper transcription factor-like 1, also called BBS17
Mchr1	melanin concentrating hormone receptor 1
MEKK2	mitogen-activated protein kinase kinase kinase 2
MG132	Benzyl N-[(2S)-4-methyl-1-[[(2S)-4-methyl-1-[[(2S)-4-methyl-1-oxopentan-2-yl]amino]-1-oxopentan-2-yl]amino]-1-oxopentan-2-yl]carbamate
mLST8	mammalian lethal with Sec13 protein 8
MS	mass spectrometry
mSIN1	mammalian stress-activated protein kinase interacting protein 1
mTOR	mechanistic target of rapamycin

mTORC	mTOR complex
N-Myc	v-myc avian myelocytomatosis viral oncogene neuroblastoma derived homolog
NP-40	nonyl phenoxypolyethoxylethanol
NTD	N-terminal domain
OSM-9	osmotic avoidance abnormal family member 9
p53	cellular tumor antigen p53
PAGE	polyacrylamide gel electrophoresis
PBS	phosphate buffered saline
PC1	polycystin 1
PCR	polymerase chain reaction
PDCD5	programmed cell death 5
PDE	phosphodiesterase
PDK1	3-phosphoinositide dependent protein kinase-1
PEI	polyethylenimine
PH	pleckstrin homology
PhLP1	phosducin-like protein 1
PI3K	phosphatidylinositol 3-kinase
PIKK	phosphatidylinositol 3-kinase-related kinases
PIP2	phosphatidylinositol 4,5-bisphosphate
PIP3	phosphatidylinositol (3,4,5)-trisphosphate
PKCα	protein kinase C alpha
PKD2	polycystin 2
PLD	phospholipase D
PMSF	phenylmethane sulfonyl fluoride or phenylmethylsulfonyl fluoride
PRAS40	proline-rich Akt substrate of 40 kDa
PTCH1	Patched 1
PTEN	phosphatase and tensin homolog
Rag	Ras-related GTPase
Raptor	regulatory associated protein of mTOR
Ras	rat sarcoma
RBD	ribosome binding domain

RBD	Ras-binding domain
REDD1	regulated in development and DNA damage responses 1
Rheb	Ras homolog enriched in brain
Rictor	rapamycin-insensitive companion of mTOR
RNA	ribonucleic acid
RNC	Raptor N-terminal conserved
S6	ribosomal protein S6
S6K	S6 kinase
SDS	sodium dodecyl sulfate
SEC	size exclusion column
SGK	serum/glucocorticoid regulated kinase 1
sgRNA	small guide RNA
siRNA	small interference RNA
SKAR	S6K Aly/REF-like target
SMG1	suppressor of morphogenesis in genitalia
SMO	Smoothened
SSTR3	somatostatin receptor 3
SST	somatostatin
STAT	signal transducers and activators of transcription
SUFU	suppressor of fused homolog
TAP	tandem affinity purification
TCEP	tris(2-carboxyethyl)phosphine
TEM	transmission electron microscopy
TEV	tobacco etch virus
TFA	trifluoroacetic acid
TOS	TOR signaling
TRD	tetratricopeptide repeats
tRNA	transfer RNA
TRRAP	transformation/transcription domain-associated protein
TSC	tuberous sclerosis complex
TTT-R2TP	Tel2-Til1-Til2 and Rvb1/2-Tah1-Pih1
UAA-XL	unnatural amino acid photo-crosslinking

UV	ultra violet
VHL	von Hippel Lindau tumor repressor
WAC	WW domain containing adaptor with coiled-coil
WD40	protein primary sequence motif of 40 amino acids often ending in WD, successive WD40 repeats create β-propeller structure
XL-MS	chemical crosslinking coupled with mass spectrometry

Chapter 1: BBS AND BBSOME

Summary

Mutations in BBS proteins cause Bardet-Biedl syndrome, a disease that exhibits multiple ciliary dysfunctions such as retinal degradation, obesity, kidney dysfunction, polydactyly, and other disorders. Eight BBS proteins (BBS1-2, 4-5, 7-9, and 18) are assembled into a large complex referred to as the BBSome and facilitate intraflagellar transport in primary cilia. Three of the BBSome subunits BBS2, 7, and 9 make up the BBSome core complex, a BBSome assembly intermediate that serves as a scaffold for other BBSome proteins. A hybrid structural analysis of the purified BBSome core complex using cryogenic electron microscopy, crosslinking coupled with mass spectrometry, and unnatural amino acid crosslinking, revealed a parallel arrangement of BBS2 and 7 with direct interactions between their coiled-coil domains and association between BBS2 and 9 through their α-helical domains in the BBSome core complex. These molecular details are needed to understand why mutations in BBS2, 7 and 9 disrupt BBSome function and are essential to develop molecular therapeutics for the ciliopathies associated with Bardet-Biedl syndrome.

Introduction

Bardet-Biedl syndrome

Bardet-Biedl syndrome (BBS) is an autosomal recessive and rare genetic disorder found about one in every 150,000 individuals [1, 2]. There are various symptoms observed among each patient, even patients of the same family. A BBS diagnosis is determined by the following criteria: patients exhibiting four of the primary BBS features such as rod-cone dystrophy, polydactyly, obesity, learning disabilities, hypogonadism (in males), and renal anomalies; or three primary features and two secondary features such as speech abnormalities, brachydactyly/syndactyly, polydipsia/polyuria, ataxia, diabetes mellitus, hepatic fibrosis, developmental delay, left ventricular hypertrophy/congenital heart disease, abnormal dentition/palatal defects, and strabismus/cataracts/astigmatism [3-5]. Some BBS features in human patients are obvious at birth, some features become apparent only in late years and make diagnosis difficult. For example, obesity, a major feature of BBS, is only observable at around 2-3 years after birth although a significant weight gain is frequently observed within the first year. Another main feature of BBS, vision loss including night blindness, occurs as a result of gradually progressive retinal degeneration. Night blindness usually appears by age seven to eight years, and the legal blindness tends not to appear until a mean age of 15.5 years. Learning impairment is also a symptom of BBS which is not directly lethal to the patients [6, 7]. A principal cause of mortality in BBS patients is renal dysfunction [8-10]. While kidney dysfunction appears at the age of 70s in normal individuals, 50 % of BBS patients who died with renal problem were less than 44 years old [1]. Kidney failure in BBS patients is not diagnosed until first decade of their age in most cases, and discovery of the symptom in the early childhood is relatively rare [5, 11]. Though the first known case of BBS was reported more than a century ago, the low number of cases of this rare genetic disorder caused delays in defining symptoms and establishing criteria for accurate diagnosis. The details of how these phenotypes are developed and become visible are still unclear.

BBS genes

There are more than 20 genes identified to encode BBS proteins, and the number continues to grow over the time [4]. Mutations in any of those genes result in BBS phenotypes. The statistics show that BBS1 is the most frequently mutated gene found in BBS patients (>23 %). BBS10 mutants contribute 20 % of the BBS cases. BBS2, 4, 6-9, and 12-13 each account for 1-10 % of all BBS cases. Less than 1 % of BBS mutations are attributed to the other BBS genes, and the cause of BBS is not known in about 25 % of BBS patients. Researchers believe that the wide distribution of BBS symptoms and severity of the disease derives not only from mutations in BBS genes but also from mutations in additional non-BBS genes. This analysis of the genes involved in BBS has tracked the source of the disease to a ~ 500 kDa complex called the BBSome, which is made up of eight of the BBS proteins (BBS1-2, 4-5, 7-9, and 18). The BBSome facilitates biogenesis and maintenance of primary cilia in cells. Three other BBS proteins (BBS6, 10, and 12) form a complex called the chaperonin-like BBS complex (CL-BBS) that is crucial in the assembly of the BBSome [4, 6]. Considering that these 11 BBS genes essential for BBSome formation are mutated in more than 73 % of all BBS cases and that five more additional BBS genes are known to be necessary for BBSome function, it is certain that understanding BBSome function provides deeper insight into the cause of Bardet-Biedl syndrome. The lack of a functional BBSome, due to mutations in any of those BBS proteins, impairs cilia biogenesis and results in BBS, hence BBS is categorized as a ciliopathy, a disease resulting from ciliary malfunction.

Cilium as cellular antenna

Every eukaryotic cell has a primary cilium [12]. Primary cilia function as cellular antennae to detect the extracellular environment, while secondary cilia such a flagella and motile cilia function as motors to drive cell motility. Both types of cilium consist of circularly ordered nine pairs of microtubule scaffolding called the axoneme, covered by membrane and anchored in the cell by a basal body. Primary cilia are distinguished from motile cilia by their relatively short protrusion and lack of the central microtubule pair of the axoneme. Not like the secondary cilia observed in only a few cell types such as sperm, epithelia cells, and ependymal cells, the primary cilia are found in all cell types, which explains the widespread physiological dysfunction that occurs when primary cilia are absent due to genetic causes. The surface of the individual primary cilium is concentrated with receptor molecules to sense signals from other cells and the external environment in the form of chemicals, light, and kinetic forces [5, 12-14].

Hedgehog signaling is a canonical example of the primary cilium as a center of signal transduction [15]. The pathway is crucial for embryonic development and adult tissue homeostasis, renaturation and renewal. Hedgehog (Hh) proteins are ligands for the receptor Patched (PTCH1) and their interaction with PTCH1 initiates a pathway for cell growth, apoptosis, differentiation in a concentration- and time-dependent manner. Once PTCH1 receives its ligand on the ciliary membrane, it exits the cilium. Subsequently, the G protein-coupled receptor (GPCR)-like membrane protein Smoothened (SMO) is freed from inhibition by PTCH1, accumulates in the cilium, and activates GLI proteins, the transcription regulators for the Hh signaling pathway. There are three types in GLI proteins, GLI1, GLI2, and GLI3. While GLI1 and 2 up-regulate transcription of the targets for the Hh pathway, GLI3 suppresses their transcription. Without enriched SMO in cilia, GLIs are transported through cilia by Kif-7 and

SUFU and proteolytically processed to form the truncated GLI3 protein that represses Hh gene transcription. On the contrary, with SMO in cilia GLIs are dissociated from Kif-7 and SUFU and are not cleaved. Full length GLI1/2 are transported to the nucleus where they induce transcription of the targets of Hh pathway and other transcription factors such as PTCH1, GLI1, N-Myc, and FOXM1 [4, 16-18]. Localization and transportation of proteins in cilia must be strictly regulated for this kind of signaling to function properly. Recent studies have revealed that BBS proteins contribute to hedgehog signaling by regulating PTCH1 and SMO transport [19, 20].

Various types of GPCRs are also found in primary cilia. Somatostatin receptor type 3 (SSTR3) is one of the seven membrane spanning GPCRs especially found in the primary cilia of neurons in the mammalian brain [21]. SSTR3 controls neurotransmission and cell proliferation via its peptide hormone ligand, somatostatin (SST). Melanin-concentrating hormone receptor 1 (Mchr1), dopamine receptor 1 (D1), serotonin receptor 6 and the leptin receptor are other examples of ciliary GPCRs in neurons which require BBS proteins for their localization in cilia [22-25]. In addition, the outer segments of photoreceptor rod and cone cells are large primary cilia that function as sensitive detectors of photons of light [26]. Protein trafficking in and out of the photoreceptor cell outer segment is important for regulation of the phototransduction system. Proteins involved in phototransduction such as opsin, G protein, phosphodiesterase (PDE), guanylyl cyclase (GC), opsin kinase and arrestin must be localized at proper places in photoreceptor cells to ensure proper phototransduction. Activation of opsin GPCRs by light induces the G protein transducin to initiate the signal transduction cascade of vision. Important light adaptation processes involve moving arrestin into the outer segment to deactivate opsin and moving transducin out to inhibit phototransduction [27, 28].

These examples demonstrate that receptors, signaling proteins, and building blocks of the cilium must be constantly expressed, transported, and localized via a highly regulated transport system. Such a system in the cilium is called intraflagellar transport (IFT) [12, 14]. In IFT, numerous protein cargos are carried along the microtubule rails both to the tip (anterograde) and to the base (retrograde) so that homeostasis of the cilium and necessary ciliary signaling are maintained (**Figure 1.1**). The kinesin-2 complex is the main motor for anterograde IFT, and the dynein complex is responsible for retrograde IFT movement. Proteins associated with IFT are usually parts of IFT complex (IFT A/B), and some BBS proteins are recognized as IFT proteins [4, 29]. Recent studies have revealed that BBSome is closely involved in regulation, stabilization, and assembly of the components in this delivery system [22, 23, 25, 30, 31].

Physiological role of the BBSome

The function of the BBSome is being studied extensively, and an understanding of its role is beginning to emerge (**Figure 1.1**). The BBSome is known to localize at the centriolar satellite and the ciliary body [4, 32]. Most other BBS genes also localize to cilia and have been observed to interact with ciliogenesis-associated proteins [1]. However, proper cilia formation is independent of the BBSome components, suggesting an indirect relationship between BBSome function and ciliogenesis [4, 20, 29, 33-35]. A number of BBSome binding partners have been found, and many of them are of components of the IFT complex [30, 36]. Furthermore, several studies show that the BBSome assembles and co-migrates with IFT complexes, indicating that the BBSome is involved in ciliary transport [36-38]. What is not clear is whether the BBSome is primarily involved in transport of cargos into or out of the cilium. Several studies show that the BBSome is required for entry of receptors such as polycystin 1 (PC1) and SSTR3 into the cilium [22, 35]. In contrast, several recent studies show that the BBSome is required for the removal of membrane proteins such as phospholipase D (PLD), D1, and proteins of the Hh pathway including SMO, PTCH1, PKD2, and OSM-9 from the cilium [23, 29, 33, 39, 40]. Furthermore, loss of BBSome function in photoreceptor cells resulted in accumulation of 138 proteins in the outer segment cilium, while only eight proteins were reduced [26]. These findings suggest that the BBSome is responsible for the import of select proteins and the export of numerous proteins from the cilium.

The BBSome appears to contribute to transport by linking membrane protein cargos to the IFT machinery. The BBSome reversibly associates with the membrane through the binding of BBS1 to the small GTPase ARL6 (BBS3) in its GTP-bound form [34, 35]. In the presence of ARL6-GTP, the BBSome associates with the lipid bilayer, providing an opportunity to bind membrane proteins. The BBSome in turn associates with the IFT complex through a linker protein LZTFL1 (BBS17) that binds both the BBSome and the IFT27 subunit of the IFT complex [20, 36]. In this manner, the BBSome links membrane proteins to the IFT complex for transport.

IFT27 has also been proposed to control the change in direction of the BBSome from anterograde to retrograde transport that occurs at the tip of the cilium [38]. This reversal in movement has been proposed to occur by the following mechanism. During anterograde transport toward the tip of the cilium, GTP hydrolysis on ARL6 dissociates the BBSome from the membrane and the IFT complex, allowing the release of BBSome cargos in the cilium. At the tip of the cilium, IFT27 dissociates from the IFT complex, and the free IFT27 promotes nucleotide exchange on ARL6, reloading ARL6 with GTP and allowing the BBSome to reassociate with the membrane and an IFT complex for retrograde transport out of the cilium.

This mechanism is consistent with the accumulation of BBSomes and their cargos in the cilium when IFT27 is genetically deleted [34].

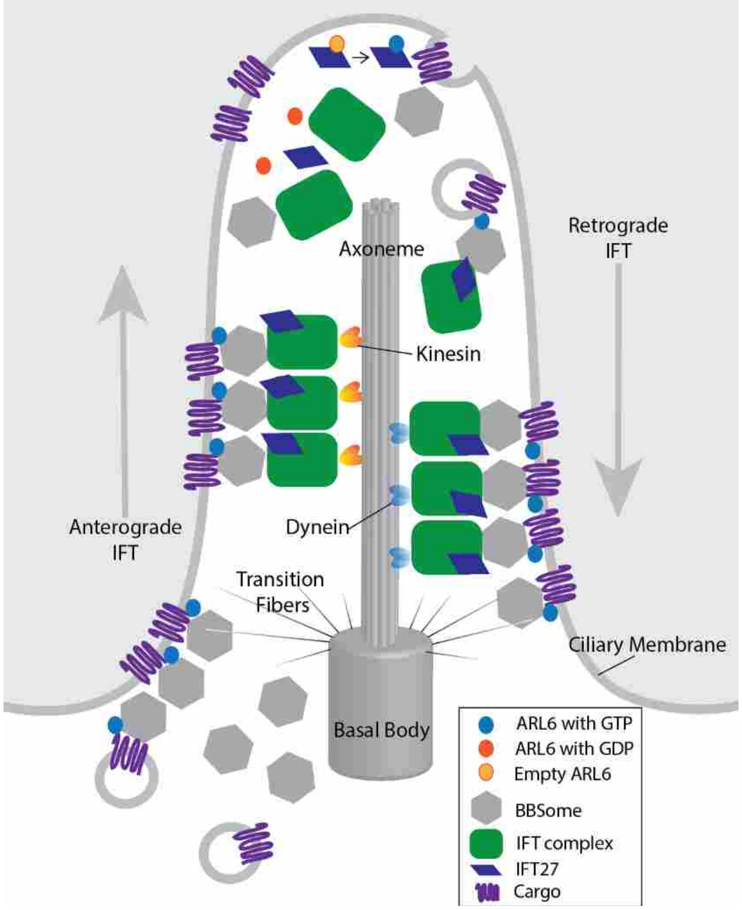

Figure 1.1 The model of BBSome mediated IFT process in primary cilia BBSome plays critical roles in transporting cargoes through primary cilia. BBSome enters into cilia by passing through the transition barrier at ciliary base with GTP-bound ARL6 and cargo. Anterograde movement is facilitated by IFT complex and kinesin walking along with the microtubule rail, axoneme. Once ARL6 hydrolyze GTP, the complex dissociates and the cargo is released to the ciliary membrane. IFT27 promotes nucleotide exchange on ARL6, and GTP-ARL6 assemble BBSome and IFT complex for retrograde transport.

The critical role of BBS1 in binding ARL6 and mediating association of the BBSome with the membrane has been demonstrated [41]. However, all eight subunits are required for its full function, but the specific contribution of the other subunits is unknown. These subunits could be involved in numerous functions including binding cargos, binding LZTFL1, providing a structural scaffold, and determining ciliary localization. The studies described in Chapter 2 provide a structural basis for understanding the function of three of the BBSome subunits BBS2, BBS7 and BBS9 that constitute the core of the complex.

Assembly of the BBSome

In order for the BBSome to function, it must be assembled from its individual components. This is a complex process and involves many proteins. The assembly mechanism of the BBSome has been studied by siRNA depletion and co-immunoprecipitation experiments [42]. These studies show that the cytosolic chaperonin containing tailless polypeptide 1 (CCT, also called TRiC) plays a key role in BBSome assembly. CCT, also named TRiC, is a eukaryotic molecular chaperone composed of 16-subunits arranged in a double ring structure with a folding cavity at the center of each ring. CCT is a major chaperone in the eukaryotic cytosol, specializing in folding proteins with complex folding patterns [43]. A unique feature of CCT is that many of its substrates contain a structure called a β-propeller fold [44]. Interestingly, several members of the BBSome (BBS1, 2, 7, and 9) have β-propeller domains, and BBS2 and BBS7 are known to interact with CCT. In addition to CCT, the BBSome requires a second chaperonin complex consisting of BBS6, 10, and 12 in the initial step of BBSome assembly [45]. These CL-BBS proteins share structural homology with CCT but whether they share CCT's protein folding mechanism is unknown. In the current model of BBSome assembly, the process begins with the association of BBS7 with BBS6 and 12. BBS10 then interacts with this complex to promote transfer of BBS7 to CCT (**Figure 1.2**). BBS2, which may have been folded in a similar manner by BBS6, 10 and 12, then associates with BBS7 on CCT. The BBS2/BBS7 dimer dissociates from CCT and binds BBS9 to form a stable complex termed the BBSome core complex (BBSCC). Other components of the BBSome (BBS1, 4, 5, 8 and 18) are subsequently recruited to the core complex to form the complete BBSome. Immunoprecipitation of BBS9 pulled down all the subunits of the BBSome indicating that the BBS9 serves as a hub in the complex. Substantially greater amounts of BBS2 and 7 were pulled down compared with the other BBSome subunits, indicating that the complex of BBS2, 7 and 9 is a scaffold in the assembly process. Cellular depletion of BBS9 did not affect the interaction between BBS2 and 7, but it reduced the association of the other BBSome subunits, demonstrating that BBS2 binds to BBS7 prior to its association with BBS9 to form the core complex [42].

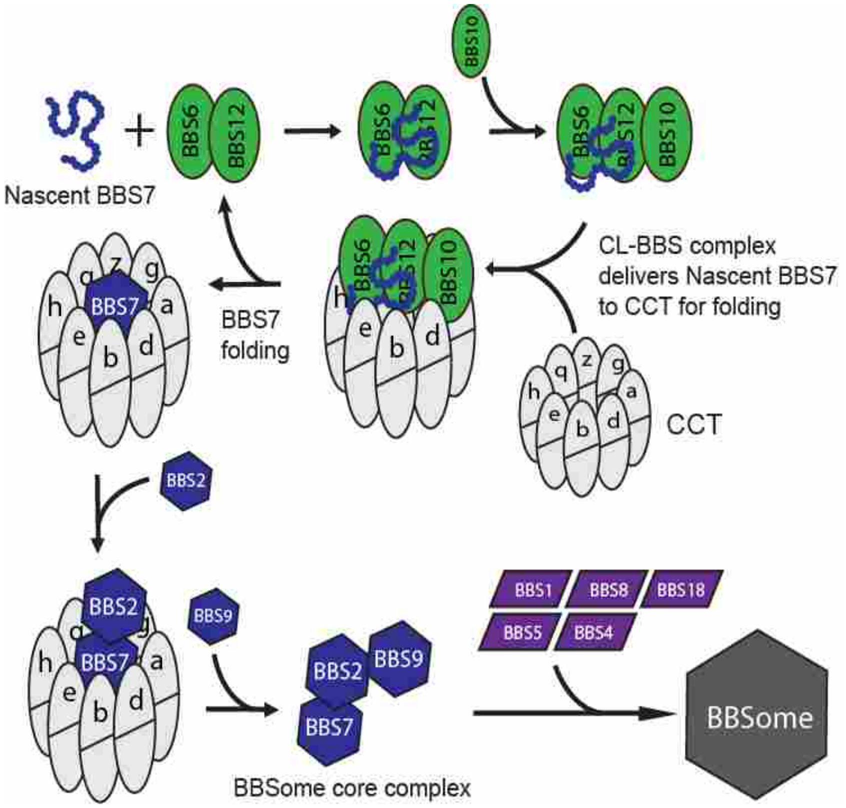

Figure 1.2 Assembly of the BBSome Nascent BBS7 is first stabilized by CL-BBS (BBS6, 10, and 12). According to co-immunoprecipitation analysis, sub-stoichiometric amount of BBS10 is found in the complex indicating that its weak interaction. BBS7 is further folded by CCT and interacts with BBS2 and 9 to form the BBSCC. The core complex serves as a scaffold providing binding sites for BBS 1, 4, 5, 8, and 18, to complete a formation of BBSome.

This model predicts that dysfunction of CCT would also cause BBS similar to loss of the CL-BBS proteins, but CCT subunits have not been identified as BBS genes. This observation can easily be explained by the fact that CCT is essential in the cell and folds up to 10 % of proteins in the proteome. Thus, deletion of or inactivating mutations in CCT proteins would be lethal [46].

Homology between BBSome core subunits and COP proteins

BBSCC is a scaffolding complex and first intermediate in the BBSome assembly process [42]. Its components, BBS2, 7, and 9 share similar molecular sizes (~100kDa) and structural homology with the same arrangement of five structural domains beginning with an N-terminal β-propeller, followed by a coiled-coil, a γ-adaptin ear (GAE), an α/β platform, and a C-terminal α-helical domains [47]. The GAE motif followed by α/β platform is a so-called appendage domain. A similar set of domains is seen in some clathrin adaptors and in COP proteins involved in vesicle transport [48, 49]. COP complexes are programmed to form cages around membrane vesicles that transport membrane proteins between compartments within the cell and the plasma membrane. The Sec13 and Sec31 subunits are the principal cage forming proteins in COPII complexes, and they share significant structural homology with BBS2, 7, and 9. Those observations suggest that the BBSCC is responsible for the membrane coat structures formed by the BBSome. In an effort to understand the structural basis of BBSome function and to reveal the molecular basis of Bardet-Biedl syndrome, we performed a structural analysis of the BBSCC. To achieve this goal, we employed an integrative approach using several structural techniques including cryogenic electron microscopy (cryo-EM), chemical crosslinking coupled with mass spectrometry (XL-MS) and unnatural amino acid crosslinking. The methods are introduced below, and the results are presented and discussed in Chapter 2.

Cryogenic electron microscopy

Cryo-EM is an advanced application of transmission electron microscopy (TEM). Instead of staining specimens by metal reagents used in conventional negative staining for TEM analysis such as uranylacetate and ammonium molybdate, cryo-EM samples are fixed in vitrified buffer under cryogenic temperature [50]. Preservation of the specimen in such conditions during observation protects protein samples from the energy of the electron beam emitted from the source, which easily brakes covalent bonds of the sample [51]. Compared with X-ray crystallography, which requires milligrams of highly purified and concentrated protein, cryo-EM requires only 10-50 μg of the protein sample. Some proteins, especially conformationally flexible ones and complexes with multiple subunits, are extremely difficult to crystallize. Moreover, only one conformation of the protein is captured in the crystal state, while cryo-EM can visualize the multiple conformations that some proteins have in solution. In the past, the main shortcoming of cryo-EM was low resolution compared with X-ray crystallography. However, new direct electron detectors enable cryo-EM to determine protein structures at near atomic resolution (3-4 Å). This resolution is high enough to observe the protein backbone and the side chain density to generate an accurate atomic model of the protein structure. Considering that the BBSCC is a multimeric protein complex with several flexible regions and that the BBSCC can only be isolated in microgram quantities from human cell lines, cryo-EM with direct electron detection is the only hope to determine its structure at high resolution.

Chemical crosslinking coupled with mass spectrometry

Even with direct electron detection it is often difficult to obtain high-resolution structures of protein complexes by cryo-EM if the complexes exhibit heterogeneity. This heterogeneity can stem from impurities, loss of subunits during purification or multiple conformational states within the complex. Recently, XL-MS has become a valuable complimentary approach to cryo-EM (**Figure 1.3**) [52-54]. Crosslinking molecules with various arm lengths and reactivity with specific target residues have been created and are commercially available, which enables researchers to optimize the experimental procedures to suit their purposes. For example, a lysine specific crosslinker that contains an N-hydroxysuccinimide ester group at each end, such as disuccinimidyl suberate (DSS), can efficiently form a covalent crosslink between two different lysines. DSS has an 11.4 Å linker arm between the nitrogens of the lysine side chains [55]. Each lysine side chain contributes another 6 Å to give a total crosslink length of 23.4 Å between the Cα atoms of the lysine residues with no flexibility in the peptide chain backbone. This length is long enough to form several crosslinks between subunits in a typical protein complex and is short enough to avoid crosslinks between proteins that do not interact if the crosslinker concentration is kept below 400 μM. After crosslinking, the protein is digested with protease, the crosslinked peptides are enriched by chromatography, and the sample is analyzed by MS. The position of the crosslinked lysine in the protein is detected with database searches, and the identified crosslinks are mapped on the model of the protein complex to refine the structure of the complex.

Several techniques can be applied to obtain confident crosslinks from a database search. First, the purer the sample, the higher quality of the data set. Tandem affinity purification (TAP) of the protein complex substantially increases sample purity. Second, higher protein concentration (~2 g/L) and amount (>200 μg) in the crosslinking reaction significantly ameliorate crosslink efficiency and peptide recovery after enrichment procedures. Third, isotopic labeling of the crosslinker greatly increases crosslink identification [54, 56]. A 50:50 mixture of hydrogen:deuterium labeled crosslinkers produce an equal amount of light and heavy crosslinked species, allowing the crosslinked peptides to be identified as doublet m/z peaks in the MS1 spectra. These doublet peaks are separated by an m/z margin that is equal to the difference between the heavy and light crosslinker molecules. The mass difference of the peaks varies depending on crosslinkers. For instance, a deuterated DSS crosslinker has a 12 Da mass difference from its undeuterated counterpart. This technique significantly enhances the ability to find crosslinked peptide species from the pool of the MS signals whose main components are non-crosslinked peptides.

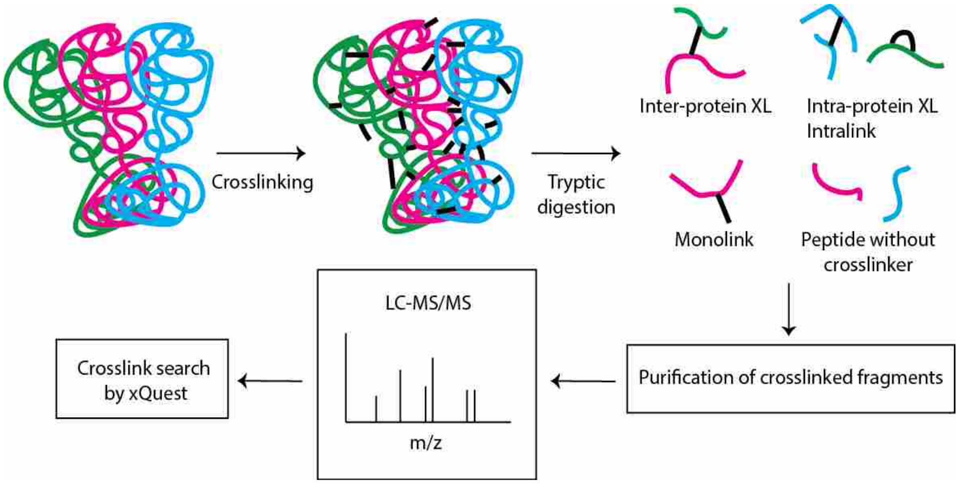

Figure 1.3 XL-MS work scheme Crosslinking of purified protein complex sample is followed by digestion by trypsin. Crosslinked peptide fragments are enriched by column purified by purification procedures such as gel filtration. The heavy and light isotope labeled crosslinking reagent gives doublet peaks upon analysis by mass spectrometry, and such peaks are searched by xQuest.

One crucial tool in the XL-MS analysis is a search engine termed xQuest [57-59]. The software was developed for finding isotopically crosslinked peptides from complex samples in an automated manner. xQuest first sorts MS1 spectra into “crosslinked-ions,” the paired peaks of the isotopically labeled crosslinks, and “common-ions,” non-paired peaks and peaks of the peptides without any crosslinker. Then it searches MS2 spectra for candidate peptides in a database of all possible digested peptide fragment pairs that is generated by xQuest from the amino acid sequence information of the proteins in the sample. Lastly, the spectra are matched and scored to evaluate the statistical confidence of the identified crosslinks.

xQuest identifies lysines that reacted with the crosslinker. If both ends of the crosslinker react with the lysines in the protein, it will produces either inter-protein crosslinks, products of the reaction between different polypeptides, or intra-protein crosslinks, products of the reaction within a single polypeptide. Inter-protein crosslinks are extremely useful to understand the relative orientation of the components of the complex. Intra-protein crosslinks help modeling structures of individual protein molecules and may be compared against the available structural data to know the degree to which the proteins have achieved a stable fold. For example, if the distance between the crosslinked lysines is longer that the allowable crosslink distance, then the protein backbone in that region must be flexible and conformationally dynamic. Finally, if one end of the crosslinker doesn't react, it results in a monolink. A propensity for monolinks at a particular lysine indicates that the residue is exposed on the surface of the protein complex with no adjacent lysines within crosslinking distance. This structural information from XL-MS can confirm structural models from high-resolution cryo-EM or it can guide the orientation of subunits within lower resolution cryo-EM electron density envelopes.

Unnatural amino acid photo-crosslinking

Unnatural amino acid photo-crosslinking (UAA-XL) can be used to identify regions of close contact between proteins. The technique uses amber stop codon suppression to insert a photo-reactive crosslinking amino acid such as p-benzoyl-L-phenylalanine (BzF) at any position in a protein sequence [60, 61]. BzF is activated by UV-light to produce 2-3 Å crosslinks with adjacent amino acids [62]. In order to incorporate BzF in a protein's primary sequence, a specific site in the target protein is genetically modified to encode the amber stop codon (TAG) (**Figure 1.4**). The cell is transfected with the modified gene along with a tRNA that has been modified to accept BzF and an engineered aminoacyl tRNA synthetase specific for the modified tRNA. BzF is then added to the cell to initiate its incorporation into the modified gene. The BzF loaded tRNA frequently binds to UAG, suppressing the amber stop codon and incorporating BzF into the target protein. However, this process is not 100 % efficient and the majority of the modified gene expresses a truncated protein due to the amber stop codon, while a fraction (~20 %) of the target protein incorporates BzF and expresses a full length form. To capture the interactions of the proteins as they are in cell, UV-light is applied immediately after the cells are lysed. Exposure to UV-light causes BzF's ketone group to be activated as a radical intermediate that reacts with any C-H bonds in close proximity to form a short covalent bond [57]. The crosslinked proteins are then isolated by immunoprecipitation and visualized in immunoblotting. Obviously, one of the advantages of this method is its high resolution structural information.

The short range crosslinking between proteins provides definitive evidence that they are directly interacting at a specific site in a cellular context. Another strength of UAA-photo-crosslinking is that the reaction is inducible by UV-light, enabling weak and transient interactions to be captured [63]. The disadvantage of UAA-XL is that it is difficult to find close contact sites between proteins in complexes without prior structural information. However, cryo-EM and XL-MS data can be used to identify potential interaction regions to search with UAA-XL.

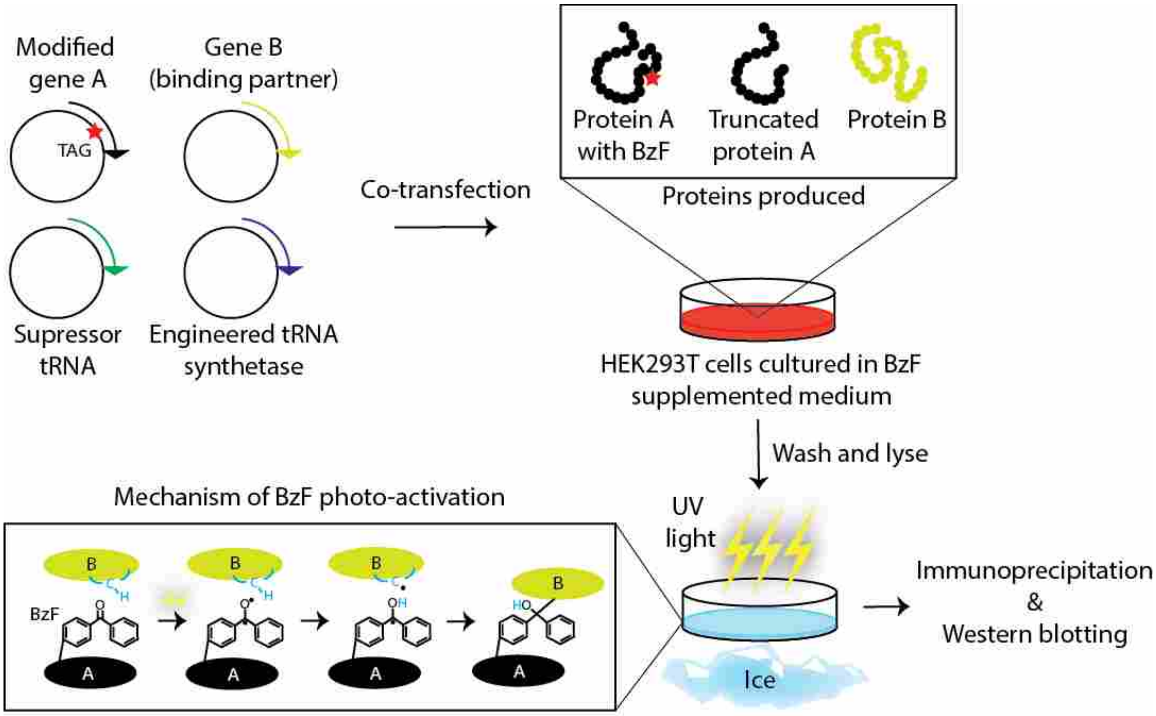

Figure 1.4 The methodology of UAA-XL Cells are co-transfected with several DNA plasmids expressing a target protein mutated to have an amber codon sequence at the residue of interest (Protein A: black), a binging partner of the target protein (Protein B: light green), suppressor tRNA that modified to accept BzF, and engineered tRNA synthetase specific for the modified tRNA. Being cultured with BzF containing media, the cells produce BzF incorporated Protein A. When BzF on Protein A in the cell lysate was activated by UV light, it reacts with a carbon atom in close proximity, supposing that the carbon atom is of Protein B, and Protein A and B are covalently crosslinked, purified by immunoprecipitation, and detected by western blotting.

Conclusion

A combination of high-resolution cryo-EM and crosslinking analysis has enabled researchers to solve the structures of proteins and protein complexes that couldn't be crystallized, greatly expanding the structural information available for the many complexes. The BBSome is one of these complexes that has resisted isolation in large enough quantities or sufficient homogeneity for X-ray crystallography. As a result, the structural insight needed to understand the function of the complex and to design therapeutic molecules to treat diseases associated with its malfunction is lacking. To address this issue, we have isolated the BBSCC and examined its structure by cryo-EM, XL-MS and UAA-XL. The results of this analysis are presented in

Chapter 2. They provide the first in depth structural understanding of BBSome function and the molecular basis of Bardet-Biedl syndrome.

CHAPTER 2: STRUCTURAL ANALYSIS OF THE BBSCC

Summary

In the effort of understanding the assembly mechanism of the BBSome and its protein transport function, the BBSome core complex (BBSCC), consisting of BBS2, BBS7, and BBS9, was purified and its structure was analyzed by a combination of electron microscopy (EM) and crosslinking techniques. Three-dimensional reconstruction of the BBSCC at ~30 Å resolution revealed a structure of the BBSCC that resembled a flattened triangle. Chemical crosslinking coupled with mass spectrometry (XL-MS) was used to construct a structural model of the BBSCC with BBS2 and BBS7 forming a tight dimer based on a coiled-coil interaction and BBS9 interacting with BBS2 through their α-helical domains. Photo-crosslinking with unnatural amino acids was employed to confirm regions of close contact between BBS2-BBS7 in a predicted coiled-coil interaction. Docking of the model into the reconstruction volume oriented the BBS2-BBS7 dimer at the base of the triangular structure and BBS9 interacting with BBS2 at the top of the triangle. The model predicted that a BBS2 R632P mutation closely linked to BBS was at the interface between BBS2 and BBS9 and this mutation was found to disrupt the interaction of BBS2 with BBS9. This finding provides a molecular explanation for BBS in patients harboring the BBS2 R632P mutation.

Introduction

Primary cilia perform vital signaling functions in vertebrate cells ranging from recognition of developmental cues from morphogens such as sonic hedgehog in the developing embryo to detection of sensory signals such as photons of light in retinal photoreceptor cells [15, 64, 65]. Primary cilia are formed by the axoneme, a circularly ordered scaffold containing nine pairs of microtubules anchored inside the cell at the basal body and protruding out from the cell surface [15, 64]. The axoneme is covered by an extension of the plasma membrane, forming a finger-like projection of the membrane that creates an isolated compartment. Many transmembrane receptors are concentrated in this ciliary compartment, creating a type of signaling antenna for the cell [66-68]. The contents of the cilium are delivered there by the intraflagellar transport (IFT) complexes that uses kinesin motors to move cargos toward the tip of the cilium (anterograde transport) and dynein motors to move cargos toward the base of the cilium (retrograde transport) [15, 64]. Failure of ciliary trafficking results in diseases referred to as ciliopathies that are characterized by multiple phenotypes, including cystic kidneys, retinal degeneration, obesity and multiple developmental disorders [69].

One of these ciliopathies is Bardet-Biedl syndrome (BBS), a disease that results from the malfunction of a large protein complex called the BBSome [30]. The BBSome consists of eight subunits (named BBS1, 2, 4, 5, 7, 8, 9 and 18), and mutations in each subunit have been linked to BBS [30, 47, 70, 71]. The disease results from an inability of the BBSome to participate in ciliary transport. The proposed function of the BBSome is to act as a scaffolding complex to link protein cargos, predominantly membrane proteins, to the IFT machinery for ciliary transport with a particularly important role in retrograde transport out of the cilium [26, 29, 33, 34, 47, 72]. The BBSome reversibly associates with the membrane via an interaction of

BBS1 with ARL6, a small GTPase that interacts with the membrane in its GTP-bound form [41, 47]. The BBSome is believed to pick up membrane proteins while in this membrane-bound state [47]. Transport of these cargos occurs through association of the BBSome with the IFT-B complex via an interaction with a linker protein LZTFL1 (Leucine zipper transcription factor-like 1) that binds to IFT27 in the IFT-B complex [19, 26, 29]. In this manner, the BBSome collects membrane proteins for IFT- and dynein-mediated retrograde transport.

To perform its transport function, each of the eight subunits of the BBSome must translated on ribosomes, folded into their native state and assembled into a functional complex. The assembly process is initiated by a system of molecular chaperones that includes the cytosolic chaperonin containing tailless polypeptide 1 (CCT) complex and three chaperonin-like proteins named BBS6, 10 and 12 because inactivating mutations in these proteins are also a major cause of BBS [42, 45]. These chaperonin proteins associate with BBS2 and BBS7 and assist in the formation of a BBS2/BBS7 dimer that then interacts with BBS9 to form the core of the BBSome complex [42]. Once this core complex is formed, the other subunits of the BBSome associate with it to assemble the full BBSome octamer [42, 73].

In an effort to better understand the mechanism of BBSome assembly and its function as a scaffold for intraflagellar transport, we have isolated the BBSCC complex and investigated its structure by EM, XL-MS and unnatural amino acid photo-crosslinking (UAA-XL). These studies contribute to understanding BBSome assembly and function and the molecular basis of BBS disease.

Methods

Purification of the BBSCC

Human embryonic kidney (HEK)-293T cells cultured in 1:1 DMEM F-12 media with 10 % fetal bovine serum (FBS) in T-175 flasks were transfected at 80 % confluency with a transfection mixture consisting of purified plasmids of the pcS2+ vector containing human BBS2 with HPC4 (Ca^{2+}-dependent protein C epitope) and c-Myc tags at the N-terminus, a pcDNA3.1 vector containing human BBS7 with a Flag-Strep tag at the N-terminus, a pcS2+ vector containing human BBS9 with a Flag tag at the N-terminus, and polyethylenimine (PEI). The DNA:PEI ratio was 1:3 by weight, and up to 90 μg of DNA was used in one T-175 flask. The media was replenished with DMEM/FBS after 2-4 hours, and the cells were incubated for 48 additional hours before harvesting. Cells were lysed in 3 mL of extraction buffer (20 mM HEPES pH 7.5, 20 mM NaCl, 1 % NP-40, 0.5 mM PMSF, and 6 mL/mL protease inhibitors cocktail (Sigma P8340), 24 U/mL benzonase nuclease) per gram of cell pellet, and the lysate was cleared by centrifugation at 13,000 *g* for 15 minutes.

The BBSCC was purified at 4º C by tandem affinity purification (TAP). The first purification column was packed with Strep-Tactin resin (iba) equilibrated with Strep equilibration buffer (20 mM HEPES pH 7.5, 20 mM NaCl, and 2 mM $CaCl_2$). The HEK-293T cell lysate was loaded for 1 hour, washed with five column volumes of Strep wash buffer (20 mM HEPES pH 7.5, 20 mM NaCl, 2 mM $CaCl_2$, and 0.05 % CHAPS), and then eluted with 2.5 column volumes of Strep elution buffer (20 mM HEPES pH 7.5, 20 mM NaCl, 2 mM $CaCl_2$, 2.5 mM desthiobiotin, and 0.05 % CHAPS). The second purification column was packed with HPC4 antibody-conjugated resin (Roche 11815024001), equilibrated with Strep equilibration buffer and loaded with the Strep column elution product for 1 hour. Subsequently, the HPC4 column was washed with two column volumes of high salt wash buffer (20 mM HEPES pH 7.5, 250 mM NaCl, 2 mM $CaCl_2$, and 0.05 % CHAPS) and one column volume of Strep wash buffer. Five elution steps were conducted, each with one column volume of HPC4 elution buffer (20 mM HEPES pH 7.5, 150 mM NaCl, 10 mM EDTA, 5 mM TCEP, 0.2 mM PMSF, 3 mL/mL protease inhibitors cocktail, and 0.05 % CHAPS), and the eluted fractions were flash frozen in liquid nitrogen and stored at -80^{o}C. HPC4 elutions from several TAP purifications were thawed, combined and concentrated to ~100 µL using a 30 kDa cutoff filter (Millipore). The concentrated sample was flash frozen in liquid nitrogen and stored at -80 ^{o}C. The purified BBSCC was analyzed by 10 % polyacrylamide SDS-gel electrophoresis and its purity was determined to be > 90 % by staining with Coomassie Brilliant Blue (Thermo Fisher Scientific). The composition of the BBSCC was confirmed by immunoblotting with anti-Flag and anti-c-Myc antibodies and by mass spectrometric analysis of excised protein bands from the Coomassie-stained gel. Blots were imaged using a LI-COR Odyssey infrared scanner, and the MS samples were analyzed by liquid chromatography coupled with tandem mass spectrometry (LC-MS/MS) using an LTQ Orbitrap XL instrument. The MS/MS data were analyzed by Mascot, a software search engine by MATRIX SCIENCE, against the human protein database.

Crosslinking coupled with mass spectrometry

About 200 µg of BBSCC was taken to be crosslinked in 25 mM HEPES pH 8.0, 100 mM KCl, and 325 µM of a 50 % mixture of H12/D12 disuccinimidyl suberate (DSS) or H6/D6 disuccinimidyl glutarate (DSG) (Creative Molecules) at 37 ^{o}C for half an hour. The reaction was quenched by adding 50 mM ammonium bicarbonate to the crosslinked sample and incubating at 37 ^{o}C for 15 minutes. The sample was dried by a vacuum concentrator, denatured in 100 mM Tris-HCl pH 8.5 and 8 M urea, reduced with 5 mM TCEP at 37 ^{o}C for 30 minutes, and alkylated with 10 mM iodoacetamide at room temperature in the dark for 30 minutes. The sample was diluted with 150 mM ammonium bicarbonate to bring the urea concentration to 4 M, and proteins were digested with 4 µg of lysyl endopeptidase (1:50 enzyme:substrate ratio) at 37 ºC for two hours. Subsequently, urea was diluted to 1 M, and proteins were further digested with trypsin at a 1:50 ratio at 37 ºC overnight. Peptide fragments were purified on a C18 column (Waters), dried, and reconstituted in 35 µL size exclusion column (SEC) mobile phase (70:30:0.1 water:acetonitrile:TFA). Crosslinked peptide fragments were enriched by SEC using a Superdex Peptide PC 3.2/30 column on an AKTA pure system (GE Healthcare) at a flow rate of 50 µL/min. The fractions with the highest peptide concentration were dried and resuspended in 2 % formic acid.

Mass spectrometry

The enriched crosslinked peptide samples were separated using a Thermo Fisher Scientific EASY-nLC 1000 Liquid Chromatograph system with a 15 cm Picofrit column (New Objective) packed with Reprosil-Pur C18-AQ of 3 um particle size, 120 Å pore size and gradient of 5-95 % acetonitrile in 5 % DMSO and 0.1 % formic acid over 185 minutes and at a flow rate of 350 uL/min. The column was coupled via electrospray to an Orbitrap Velos Pro mass spectrometer. The resolution of MS1 was 30,000 over a scan range of 380-2000 m/z. Peptides with a charge state 3+ and greater were selected for HCD fragmentation at a normalized collision energy of 35 % with 3 steps of 10 % (stepped NEC) and a resolution of 7,500. Dynamic exclusion was enabled with a 10 ppm mass window and a one-minute time frame. Samples were run in duplicate.

XL-MS analysis

The xQuest/xProphet peptide search engine was used to identify crosslinked peptides and specific lysine residues and to evaluate of the quality of each hit from the mass spectrometry data set. Tandem mass spectra for parent ions with a mass shift of 12.075321 Da for DSS crosslinker and 6.04368 Da for DSG crosslinker and a charge of +2 to +7 were classified as isotopic pairs and evaluated in ion-tag mode with the following parameters: 2 missed cleavages, 5-50 amino acid peptide length, carbamidomethyl fixed modification (57.02146 Da mass shift), oxidation variable modification (15.99491 Da mass shift), 138.0680796 Da mass shift for intra- and inter-protein crosslinks, 156.786442 and 155.0964278 Da mass shifts for mono-links, MS1 tolerance of 10 ppm, and MS2 tolerance of 0.2 Da for common ions and 0.3 Da for crosslink ions.

The peptide sequence database was created by xQuest based on the amino acid sequence of human BBS2, 7, and 9 (UniProt ID: Q9BXC9, Q8IW26, and Q3SYG4, respectively). Spectra were searched against the database which covered all possible crosslink combinations of the BBSome core proteins, and any spectra that matched crosslinks in the database were counted and evaluated. Crosslink hits were screened with the following criteria: <10 % false discovery rate, <10 % total ion counts, -4 to 7 ppm MS1 tolerance window, >20 xQuest Id-Score, and >4 fragmentation events per peptide. Those xQuest hits that satisfied the thresholds were collected and used to orient structural models of the individual domains of the BBSCC using UCSF Chimera [74].

Unnatural amino acid crosslinking

To test possibility of a coiled-coil interaction between residues 334-362 of BBS2 and residues 340-376 of BBS7, we employed amber codon suppression methods to introduce the photo-crosslinking unnatural amino acid benzoyl phenylalanine (BzF) into BBS7. Residues likely to be found at the coiled-coil interface (L345, L349, L352 and L357) were targeted. Each of the codons for these residues of BBS7 were replaced separately with an amber stop codon (TAG) by PCR using mutagenic primers in the pcDNA3.1 expression vector (Thermo Fisher Scientific). As a control, an amber codon was also introduced into residue N347, a polar residue in this same region that is predicted to be on the opposite side of the coiled-coil interaction. These constructs included N-terminal Strep and Flag tags for immunoprecipitation and immunoblotting. The constructs were transfected into HEK-293T cells along with BBS2 containing N-terminal c-Myc and HPC4 tags in the pcS2+ vector (Addgene) and the amber codon suppression vectors containing the aminoacyl-tRNA synthetase for BzF in the pcDNA3 plasmid and the amber codon suppressor tRNA in the pSVBpUC plasmid (a gift from Thomas Sakmar, Rockefeller University). The relative DNA ratios were 10:2:10:1 for the BBS7 variants, BBS2, suppressor tRNA, and aminoacyl-tRNA synthetase, respectively. In total, 11.5 μg of DNA was added to one 60 mm dish.

The cells were grown in 1:1 DMEM:F-12 media with 10 % FBS in 60 mm dishes and transfected at 80-90 % confluency with Lipofectamine 2000 (Thermo Fisher Scientific) according to the manufacturer’s protocol. The cells were fed three hours post-transfection with the same media containing 1 mM BzF (Bachem F-2800). At 48 hours post-transfection, the cells were washed with a HEPES wash buffer (20 mM HEPES pH 7.5, 150 mM NaCl) and harvested in a HEPES lysis buffer (20 mM HEPES pH 7.5, 150 mM NaCl, 6 uL/mL protease inhibitors cocktail (Sigma P8340), 0.6 mM PMSF, and 1 % NP-40). The cell lysate was triturated 8 times with a 25-gauge needle and syringe and cleared by centrifugation in a Sorvall Legend Micro 21 microfuge at 14,800 rpm for 10 minutes. Lysates were immediately exposed to UV light from a

600-W UV flood lamp (Integrated Dispensing Solutions) at a distance of 10 inches for two minutes on ice. Photo-activated samples were immunoprecipitated by incubating with an antibody to the c-Myc tag (Invitrogen 13-2500) on BBS2 for one hour at 4 ºC and then incubating with protein A/G agarose beads (Santa Cruz sc-2003) for one hour at 4 ºC. Antibody-attached beads were washed three times with the HEPES lysis buffer, and the samples were resuspended in SDS-PAGE sample loading buffer. Proteins in the samples were separated by SDS-PAGE on 9 % gels and immunoblotted with an anti-c-Myc primary antibody for BBS2 (Invitrogen 13-2500) and an anti-Flag primary antibody (Sigma F3165) for BBS7 and a near-infrared fluorescence tagged anti-mouse (LI-COR 926-32210) secondary antibody. Blots were scanned by a LI-COR Odyssey infrared scanner and imaged with Image Studio Lite software.

Mutagenesis

The consequences of 14 BBS-linked mutations in BBS2, 7 and 9 on the formation of the BBSCC were measured by co-immunoprecipitation. The mutations were introduced into N-terminally c-Myc-tagged BBS2 in pcS2+ vector, N-terminally Strep and Flag-tagged BBS7 in pcDNA3.1 vector and N-terminally Flag-tagged BBS9 also in pcS2+ vector using mutagenic PCR primers in a conventional PCR-based cloning protocol. All constructs were sequenced to confirm that the mutations were correct. Constructs were transfected into HEK-293T cells grown in 1:1 DMEM:F-12 media with 10 % FBS in 6-well plates at 80-90 % confluency using Lipofectamine 2000 according to the manufacturer’s protocol. Up to 3 µg of DNA was added to each well, and the relative DNA amounts were 1:1:1 for the BBS2, 7 and 9 constructs. Cells were fed with media three hours after transfection and incubated at 37 ºC for two days. Cells were washed with a phosphate-buffered saline (PBS) solution (12 mM phosphate pH 7.4, 137 mM NaCl, 3 mM KCl) and harvested in a PBS lysis buffer (12 mM phosphate pH 7.4, 137 mM

NaCl, 3 mM KCl, 6 uL/mL protease inhibitors cocktail (Sigma P8340), 0.6 mM PMSF, and 1 % NP-40) 48 hours after transfection. Lysed cells were triturated 8-10 times in a 25-gauge needle and syringe and cleared by centrifugation at 14,800 rpm in a Sorvall Legend Micro 21 microfuge for 10 minutes. The lysates were immunoprecipitated by incubating with an antibody to the c-Myc tag (Invitrogen 13-2500) on BBS2 as described above and immunoblotted with the c-Myc antibody for BBS2 and with the anti-Flag antibody (Sigma F3165) for BBS7 and BBS9 also as described above.

Protein separation for EM sampling

As described above, the BBSCC purified by the Strep affinity purification was concentrated to ~ 1 mg/ml. 145 µg of the concentrated protein complex was centrifuged and separated by a 10-30 % glycerol gradient in a separation buffer (20 mM HEPES pH 7.5, 100 mM KCl, 4 mM $CaCl_2$, 0.3 mM PMSF, 0.3 % protease inhibitor cocktail, 3 mM DTT) at 34,000 rpm in a SW55Ti at 4 °C for 16 hours. Fractions were analyzed in 10 % SDS gels.

EM grid preparation and data collection

5 µl aliquots of the protein samples were applied to 400 mesh grids (Maxtaform Cu/Rh HR26) coated with a thin (~ 8 nm) carbon layer and glow-discharged for 20 seconds. The grids were then stained (2 min) with 2 % uranyl acetate and air-dried before transmission EM analysis. Images were taken using Tecnai F20 transmission EM electron microscope operating at 200 kV with a 4k FEI Eagle CCD camera. Images were recorded at a sampling rate of 1.78 Å/px.

Image processing, particle selection and 2D classification

Contrast transfer function (CTF) was corrected using the CTFFIND3 program [75], which also calculated potential astigmatism. Micrographs with visible drift and astigmatism were discarded. 8806 single particles of the BBSCC were selected manually, extracted from micrographs, and normalized using the XMIPP software package [76]. Two types of algorithms implemented in XMIPP were used to classify single images, CL2D [77] and KerDenSom for immune-complexes [78].

3D reconstruction

Several initial models were tested in the first step of the 3D reconstruction procedure using EMAN software [79]: artificial noise, blob, a model created by a ‘common lines’ algorithm based on previously obtained 2D classes. Refinement was performed until the 3D reconstructions from these initial models converged to stable, similar 3D volumes. To obtain more structural detail, the 3D reconstruction from EMAN refinement was subjected to Projection Matching using XMIPP. Resolution of the final 3D models was estimated based on the FSC criterion (Fourier shell correlation) [80]. The spatial frequency at 0.5 correlation was taken as the resolution of the model. Visualization of the 3D models and docking of the atomic structures into EM volumes was performed manually using USCF Chimera [74].

Generating a structural model

All three BBSCC components share the same domain organization with N-terminal β-propeller, coiled-coil, γ-adaptin ear (GAE), platform, and C-terminal alpha-helical domains [47]. The secondary and tertiary structure of each domain was generated using the protein structure prediction servers I-TASSER [81] and SWISS-MODEL [82], and the accuracy of these domain models was confirmed using the intra-domain crosslinks from the XL-MS data. The inter-domain crosslinks were then used in Chimera to align domains relative to each other and assemble complete structures for BBS2, 7 and 9 by minimizing crosslink distances and avoiding stearic overlap. In similar fashion, the structural models for BBS2, 7 and 9 were then aligned relative to each other. This crosslink-based model of the BBSCC was fit into the EM electron density envelope in Chimera, allowing some movement of the subunits relative to each other to fit the electron density without extending crosslinking distances to unreasonable values.

Results

Purification of the BBSCC

The complex between BBS2, BBS7 and BBS9 is an important early intermediate in assembly of the BBSome. We purified this core complex for structural studies by co-expressing affinity-tagged versions of each subunit in HEK-293T cells and isolating the complex using a tandem affinity approach. Complexes containing a Strep-peptide tagged BBS7 were first purified using a Strep-Tactin column and then complexes also containing the HPC4 peptide-tagged BBS2 were purified using an HPC4 antibody-conjugated column (**Figure 2.1 A**). The purified complex was analyzed by SDS-PAGE and immunoblotting. The SDS gel image shows the BBS2, 7 and 9 bands were isolated to >90 % purity. Immunoblots verified the identity of the bands and each band was excised and its identity was confirmed by mass-spectrometry. The intensities of the three gel bands were similar, indicating that the stoichiometry of the subunits in the complex was equal.

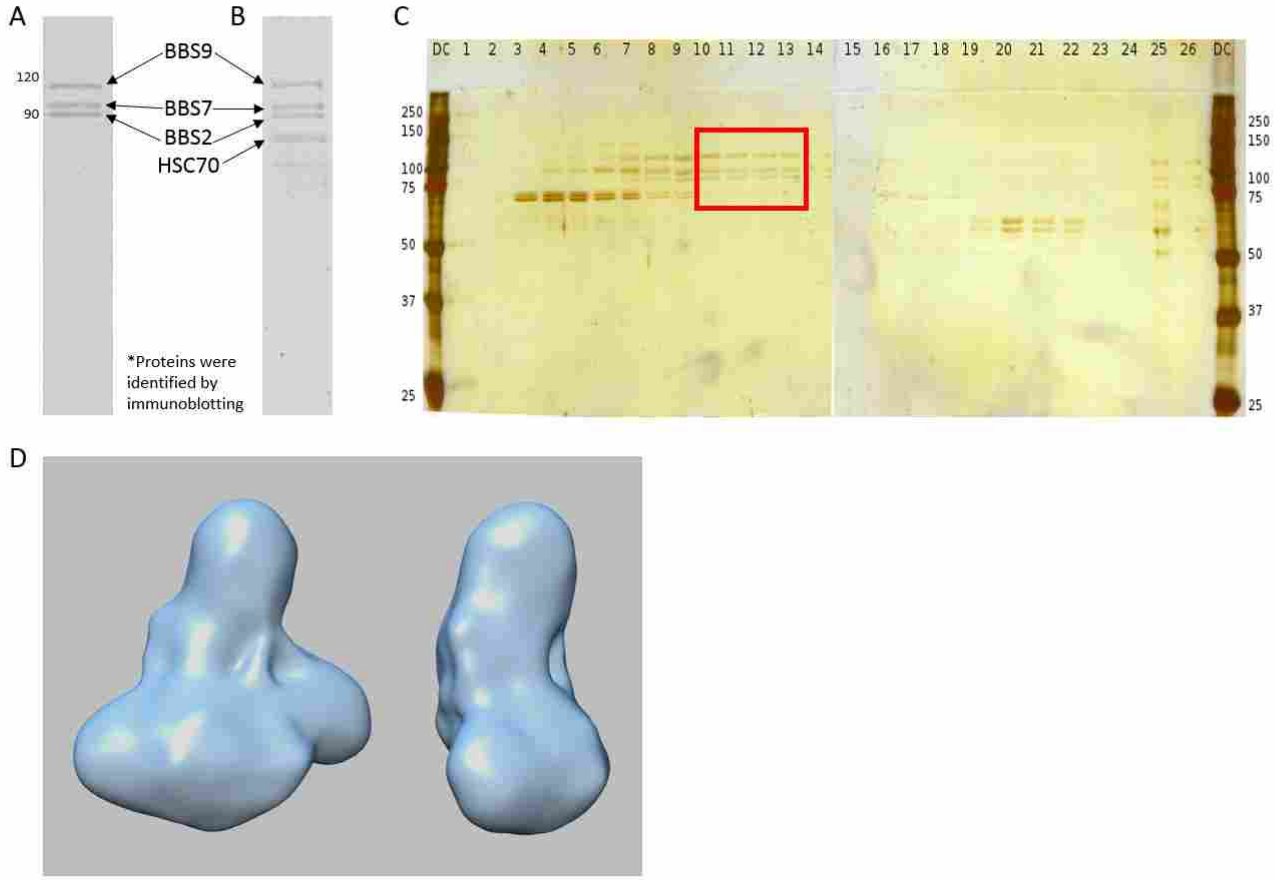

Figure 2.1 Purification and EM reconstruction of the BBSCC A) Coomassie-stained SDS gel of the BBSCC purified by TAP (Strep-HPC4). Flag-tagged human BBS9 (~100 kDa) migrated at just below the 120 kDa molecular standard, and Strep-tagged human BBS7 (~90 kDa) and HPC4-tagged human BBS2 (~90 kDa) migrated at the 90 kDa molecular standard. B) Coomassie-stained SDS gel of the BBSCC purified with a single Strep affinity column. HSC70 (heatshock cognate 70) was co-purified and migrated below BBS2. Identity of these major protein bands was confirmed by immunoblotting. C) Silver-stained SDS gel of the BBSCC purified with a single Strep affinity column and separated by a glycerol gradient purification. The post-centrifugation fractions were loaded from the top (left) to the bottom (right). The fractions in the red box (fraction number 10-13) were used for EM analysis. D) EM reconstruction of the purified BBSCC.

Electron microscopy

We assessed the homogeneity of the purified BBSCC by negative stain electron microscopy and found that despite the gel purity the samples were too heterogeneous, with what appeared to be both aggregated and dissociated particles, for further EM analysis. To decrease the heterogeneity, we modified our purification scheme to include a glycerol density gradient separation after the Strep-Tactin affinity column. Prior to the gradient, gels showed equal amounts of BBS2, 7 and 9 bands but there was an additional band at 70 kDa in the complex (**Figure 2.1 B**). Mass spectrometry and immunoblotting identified this band as the chaperone heatshock cognate (HSC) 70. The glycerol gradient caused dissociation of much of the complex, but the intact BBSCC without HSC70 was isolated in higher molecular weight fractions (**Figure 2.1 C**). This complex showed less heterogeneity in negative stain EM, but the particles were still not sufficiently homogeneous for high-resolution cryo-EM analysis. As a result, we proceeded with a low-resolution EM reconstruction from the negative-stained images. This reconstruction revealed the overall structure of the BBSCC. It shows a roughly triangular mass suggesting that each subunit fits within the vertices of the triangle (**Figure 2.1 D**).

Structures of BBS2, 7 and 9 domains

Important information about the structure of protein complexes can be obtained from docking atomic structures of the individual subunits into low resolution EM reconstructions. However, there are no complete atomic structures for the subunits of the BBSCC. BBS2, 7 and 9 share a well-defined domain organization with an N-terminal β-propeller, followed by coiled-coil, GAE, platform, and a C-terminal α-helical domain [47]. One atomic structure of the β-propeller domain of BBS9 has recently been reported [83], and the structures of homologous domains in other proteins have been solved [47]. Given these homologs, we reasoned that accurate structural models of each domain could be determined, and we generated models of each domain using the protein structure prediction servers I-TASSER [81] and SWISS-MODEL [84] (**Figure 2.2**).

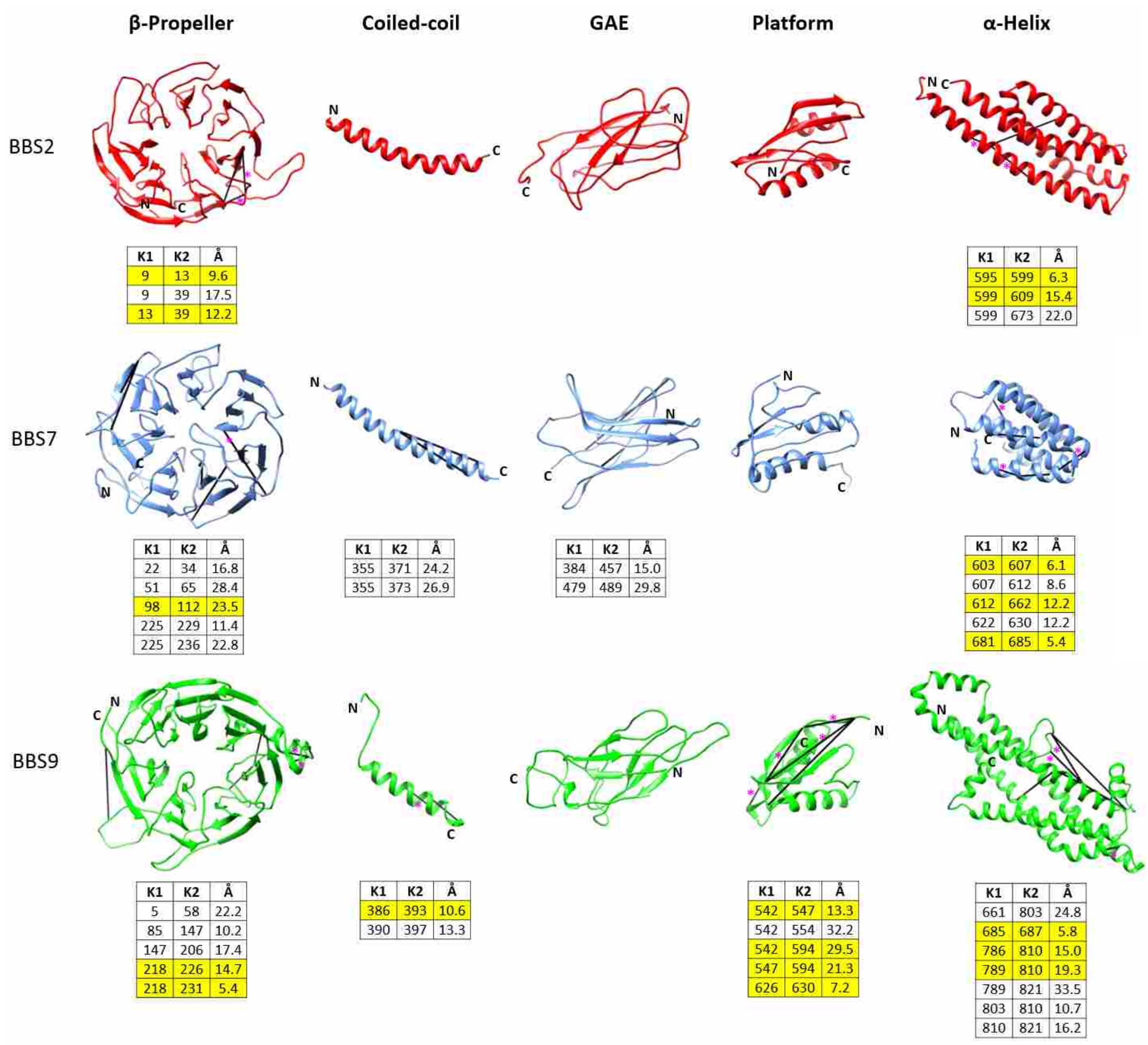

K1	K2	Å
9	13	9.6
9	39	17.5
13	39	12.2

K1	K2	Å
595	599	6.3
599	609	15.4
599	673	22.0

K1	K2	Å
22	34	16.8
51	65	28.4
98	112	23.5
225	229	11.4
225	236	22.8

K1	K2	Å
355	371	24.2
355	373	26.9

K1	K2	Å
384	457	15.0
479	489	29.8

K1	K2	Å
603	607	6.1
607	612	8.6
612	662	12.2
622	630	12.2
681	685	5.4

K1	K2	Å
5	58	22.2
85	147	10.2
147	206	17.4
218	226	14.7
218	231	5.4

K1	K2	Å
386	393	10.6
390	397	13.3

K1	K2	Å
542	547	13.3
542	554	32.2
542	594	29.5
547	594	21.3
626	630	7.2

K1	K2	Å
661	803	24.8
685	687	5.8
786	810	15.0
789	810	19.3
789	821	33.5
803	810	10.7
810	821	16.2

Figure 2.2 Domain structural models of the components of the BBSCC Crosslinks (black lines) were formed among domains (β-propeller, coiled-coil, GAE, platform, and α-helix) of each BBSCC component (BBS2-red, BBS7-blue, and BBS9-green). The tables show the number of intra-domain crosslinks, identify the crosslinked lysines and give the distance of each crosslink. All cross-links were found with the DSS cross-linker except BBS7 K98-K112 which was only found with DSG. Yellow rows and pink asterisks indicate the crosslink also formed by DSG. N- and C-terminal of each domain are indicated as well.

To assess the accuracy of the domain models, we turned to XL-MS, a technique that has become a practical tool to assist in protein structure determination. The tandem affinity purified BBSCC was crosslinked with two different lysine specific crosslinkers, DSS and DSG (**Figure 2.2**). Both crosslinkers contained a 50:50 mixture of normal (light) and deuterium-substituted (heavy) isotopes to create doublet pairs of m/z peaks to identify crosslinked peptides. After crosslinking, the complex was digested with proteases and the resulting peptides were enriched for crosslinked peptides by size exclusion chromatography. The enriched peptide mixture was analyzed by LC-MSMS, and crosslinked peptides were identified in the MS data using the crosslink search engine xQuest. This program searches for doublet m/z peaks separated by the weight difference between the light and heavy crosslinker isotopes and uses the MSMS data to identify the peptides and their crosslinked lysines. Only high confidence hits that satisfy the screening criteria were considered as true crosslinks.

There were three types of crosslinks that provided different types of structural information: crosslinks within individual domains of the BBSome subunits (intra-domain crosslinks), crosslinks between domains of the subunits (inter-domain crosslinks) and crosslinks between subunits (inter-protein crosslinks). We used the distance constraints from the intra-domain crosslinks to assess the accuracy of the domain models (**Figure 2.2**). The distance between Cα carbons of lysine residues, taking into account normal movement of the protein backbone, is ~ 30 Å for the DSS crosslinker and ~ 26 Å for the DSG crosslinker [43, 44, 58]. When mapped to the domain models, 38 of the 40 intra-domain crosslinks fell within these distance constraints while the two others measured 32 Å and 33 Å (**Figure 2.2**). The consistency between the structural models and the crosslinking distances verifies the accuracy of the domain models for BBS2, 7 and 9 and the quality of the crosslinking data.

BBS2 and BBS7 interact through a coiled-coil domain

XL-MS identified 12 inter-protein crosslinks that could be used to locate sites of interaction between subunits in the BBSCC (**Figure 2.4 A and 2.5 C**). Nine of these crosslinks were between BBS2 and BBS7 and six were in regions predicted to form coiled-coils (residues

333-363 of BBS2 and 339-376 of BBS7). This high density of crosslinks supports the idea that BBS2 and BBS7 interact via a coiled-coil interaction in these regions. A model of this interaction based on the crosslinking data is shown in **Figure 2.3 A**. Interestingly, no inter-protein crosslinks were found in the same coiled-coil region of BBS9, suggesting that BBS9 does not form a coiled-coil interaction with BBS2 or 7. The other three inter-protein crosslinks were between BBS2 and BBS9, and no crosslinks were observed between BBS7 and BBS9. These data are consistent with pair-wise co-immunoprecipitation experiments that showed interactions between BBS2 and BBS7 as well as between BBS2 and BBS9 but not between BBS7 and 9 [42, 73].

To further test the possibility that BBS2 and BBS7 interacted through their coiled coil regions, we turned to unnatural amino acid crosslinking. We replaced the codons for L345 and L349 of BBS7 with the amber stop codon. These leucine residues could be involved in a coiled-coil interaction with BBS2 because they are hydrophobic and are oriented on the same side of the BBS7 α-helix predicted to form a coiled-coil. As a control, we also introduced an amber codon at position N347. This asparagine residue would not be expected to contribute to a coiled-coil interaction because it is hydrophilic and is oriented on the opposite side of the α-helix from L345 and L349. BBS7 constructs with these changes were transfected into HEK-293T cells along with constructs of the suppressor tRNA and BzF tRNA synthetase. Cell were incubated with BzF and extracts were crosslinked with UV light. BBS7 was immunoprecipitated and immunoblotted for BBS2 to detect any crosslinked species. Photo-activated BzF creates a high-energy intermediate that rapidly reacts with atoms at an ~ 3 Å radius [85]. Thus, any BBS2 crosslinks would indicate regions of close contact.

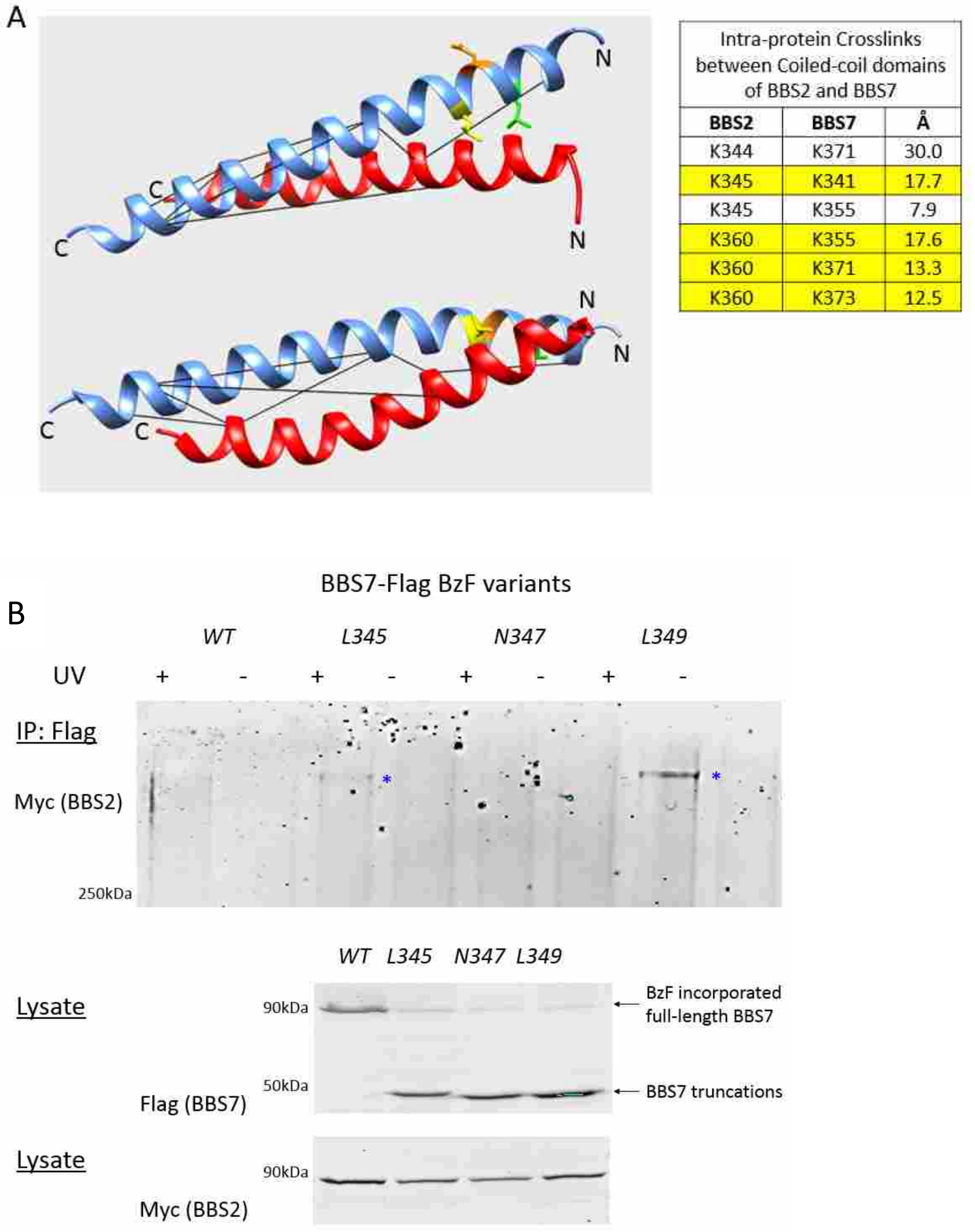

Intra-protein Crosslinks between Coiled-coil domains of BBS2 and BBS7

BBS2	BBS7	Å
K344	K371	30.0
K345	K341	17.7
K345	K355	7.9
K360	K355	17.6
K360	K371	13.3
K360	K373	12.5

Figure 2.3 Specific interaction between BBS2 and BBS7 A) Depiction of the coiled-coil interaction between BBS2 (red) and BBS7 (blue). Crosslinks are indicated as black lines, and BBS7 residues, L345, N347, and L349, are indicated as green, orange, and yellow, respectively. N- and C- termini of each domain is labeled. The table shows the list of crosslinks formed between lysines in coiled-coil domains of BBS2 and BBS7 with their distances in angstrom. Yellow columns indicate the crosslink also formed by DSG. All listed crosslinks were seen in DSS crosslinking. B) HEK-293T cells were co-transfected with FLAG-tagged BBS7 amber codon variants (wild type, L345, N347, or L349), Myc-tagged BBS2, tRNA, and BzF aminoacyl tRNA synthetase. Cells were fed with media containing BzF. Cell lysates were irradiated with UV light to initiate the cross-linking reaction. BBS7 was immunoprecipitated with an anti-FLAG antibody, and covalent BBS2-BBS7 crosslinked species were detected by immunoblotting (marked with *). Cell lysates were also immunoblotted to show correct overexpression and incorporation of BBS7 BzF variants and BBS2.

The BBS7 L349BzF variant showed a clear band at >300 kDa in the BBS2 blot while the BBS7 L345BzF variant showed a weak band at the same position (**Figure 2.3 B**). These bands migrate much higher in the gels than the BBS2 band and are greater than the sum of the molecular weights of individual BBS2 (84 kDa) and BBS7 (85 kDa). We have previously observed slower migration with crosslinked proteins [44] that likely stems from their branched molecular shape. The bands were not observed with wild-type BBS7, nor were they seen without UV light exposure, indicating that the crosslinks were specific. Importantly, the N347BzF variant also showed no crosslinked bands, which would be expected for a hydrophilic residue located on the opposite side of an α-helix involved in a coiled-coil interaction. Together, these findings confirm that a close contact occurs between BBS2 and BBS7 in this region and are entirely consistent with the predicted coiled-coil interaction.

Structural model of the BBS2-BBS7 dimer

Using the coiled-coil interaction between BBS2 and BBS7 as a scaffold, the inter-protein and inter-domain crosslinks were used as constraints to build a model of the BBS2-BBS7 dimer (**Figure 2.4**). In BBS7, there were 13 inter-domain crosslinks: one between the β-propeller domain and the coiled-coil domain, five between the GAE domain and the coiled-coil domain and three between the platform domain and the coiled-coil domain, one between the GAE domain and the α-helical domain and three between the platform domain and the α-helical domain (**Figure 2.4 A**). These crosslinks suggest a domain organization in which the coiled-coil region is in the center of the structure surrounded by the GAE and platform domains, with the α-helical domain extending away from the core of the protein. In BBS2, there was only one inter-domain crosslink which occurred between the coiled-coil domain and the β-propeller domain. This lack of inter-domain crosslinks can partially be explained by the fewer number of lysine residues in BBS2 (28) than BBS7 (52), but it must also reflect a more extended structure for BBS2 in which the domains are more separated.

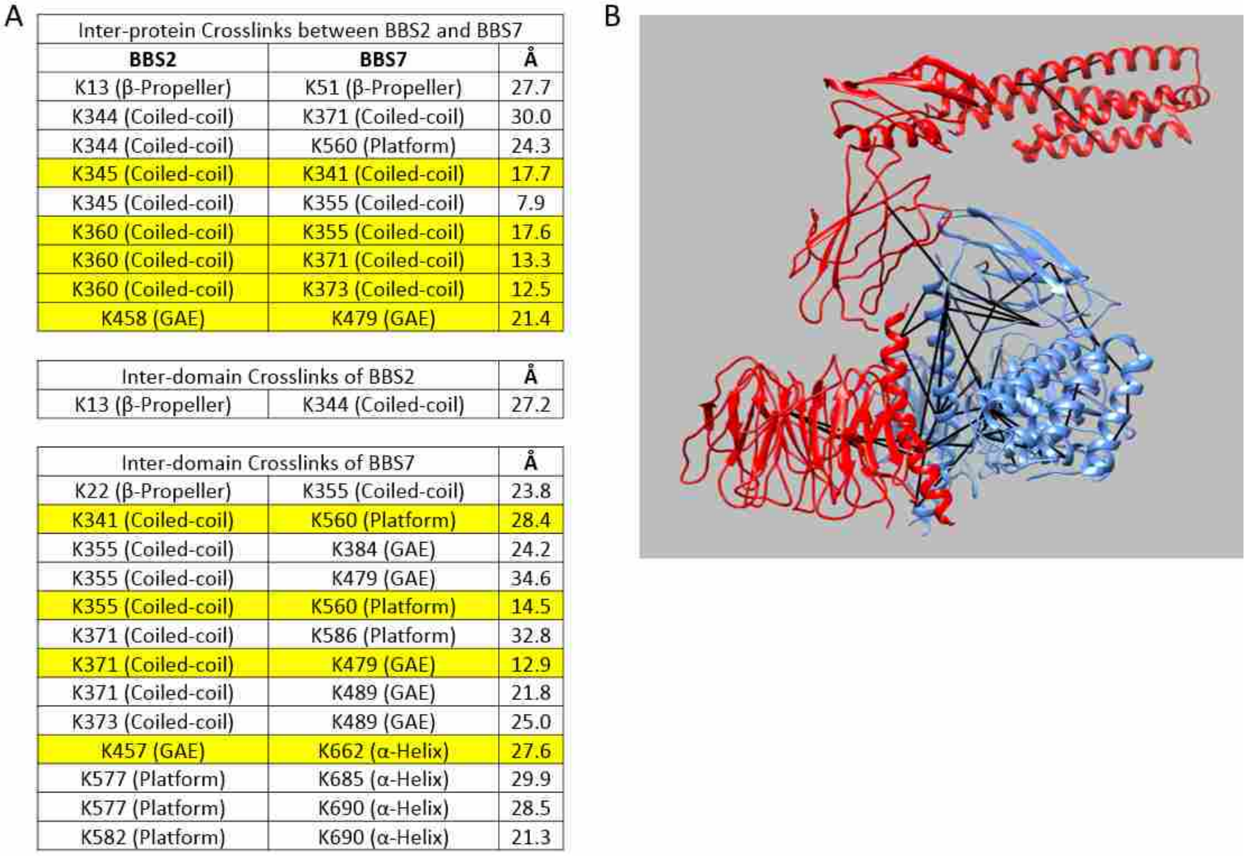

Inter-protein Crosslinks between BBS2 and BBS7		
BBS2	**BBS7**	**Å**
K13 (β-Propeller)	K51 (β-Propeller)	27.7
K344 (Coiled-coil)	K371 (Coiled-coil)	30.0
K344 (Coiled-coil)	K560 (Platform)	24.3
K345 (Coiled-coil)	K341 (Coiled-coil)	17.7
K345 (Coiled-coil)	K355 (Coiled-coil)	7.9
K360 (Coiled-coil)	K355 (Coiled-coil)	17.6
K360 (Coiled-coil)	K371 (Coiled-coil)	13.3
K360 (Coiled-coil)	K373 (Coiled-coil)	12.5
K458 (GAE)	K479 (GAE)	21.4

Inter-domain Crosslinks of BBS2		Å
K13 (β-Propeller)	K344 (Coiled-coil)	27.2

Inter-domain Crosslinks of BBS7		Å
K22 (β-Propeller)	K355 (Coiled-coil)	23.8
K341 (Coiled-coil)	K560 (Platform)	28.4
K355 (Coiled-coil)	K384 (GAE)	24.2
K355 (Coiled-coil)	K479 (GAE)	34.6
K355 (Coiled-coil)	K560 (Platform)	14.5
K371 (Coiled-coil)	K586 (Platform)	32.8
K371 (Coiled-coil)	K479 (GAE)	12.9
K371 (Coiled-coil)	K489 (GAE)	21.8
K373 (Coiled-coil)	K489 (GAE)	25.0
K457 (GAE)	K662 (α-Helix)	27.6
K577 (Platform)	K685 (α-Helix)	29.9
K577 (Platform)	K690 (α-Helix)	28.5
K582 (Platform)	K690 (α-Helix)	21.3

Figure 2.4 BBS2-BBS7 dimer A) BBS2 and BBS7 inter-protein crosslinks and inter-domain crosslinks. The tables show the domains and residue numbers of crosslinked lysines and distances of each crosslink. Yellow rows indicate the crosslinks also formed by DSG, and all crosslinks listed in this figure except BBS7 K475-K662 were formed by DSS. B) BBS2 (red)-BBS7 (blue) dimer structure based on XL-MS. Cross-links are indicated as black lines.

The inter-protein crosslinks were also taken into account in assembling the BBS2-BBS7 dimer. There were two crosslinks between BBS2 and BBS7 in addition to the six crosslinks in their coiled-coil interaction, one between the β-propeller domains and one between the GAE domains. Combining both the inter-domain crosslinks and the inter-protein crosslinks places the coiled-coil interaction at the center of the dimer flanked by the β-propeller domain of BBS2 on one side and the β-propeller, GAE, platform and α-helical domains of BBS7 on the other side (**Figure 2.4 B**). The BBS2 GAE domain extends away from the coiled-coil, making contacts with the BBS7 GAE domain, followed by the BBS2 platform and α-helical domains that make no contacts with the rest of the structure and thus their exact orientation is undetermined. This structure suggests an elongated BBS2 fold connected to a more compact BBS7 fold which are tethered together by the coiled-coil interaction.

Structural model of the BBSCC

To complete the structural model of the BBSCC, we analyzed the inter-domain and inter-protein crosslinks of BBS9. There were 11 inter-domain crosslinks in BBS9: four between the β-propeller and coiled-coil domains, two between the β-propeller and α-helical domains, one between the β-propeller and GAE domains, one between the coiled-coil and GAE domains, one between the coiled-coil and platform domains, one between the GAE and platform domains, and one between the GAE and α-helical domains (**Figure 2.5 A**). Based on these crosslinks, the domains of BBS9 were assembled into a structural model that resembles that of BBS7, with the coiled-coil region in the center surrounded by the other domains (**Figure 2.5 B**). One difference is that the α-helical domain of BBS9 is larger than that of BBS7, allowing it to reach back across the structure to make contacts with the β-propeller domain (**Figure 2.5 B**).

The remaining three inter-protein crosslinks between BBS2 and BBS9 were used to guide the docking of BBS9 to the BBS2-BBS7 dimer and obtain a structure of the BBSCC (**Figure 2.5 C**). There were two crosslinks between their α-helical domains and one between the BBS9 platform domain and the BBS2 α-helical domain. These crosslinks position the α-helical domain of BBS2 in close contact between the platform and α-helical domains of BBS9 (**Figure 2.5 D**).

There were no crosslinks between BBS9 and BBS7, indicating that BBS9 is not in close contact with BBS7 and supporting the proposed extended structure of BBS2.

This structural model of the BBSCC was docked into the electron density from the EM reconstruction (**Figure 2.5 E**). The BBS2-BBS7 dimer fit best at the base of the triangular structure although there was extra EM density not filled by the models. The BBS9 structure fit best in the EM density at the top of the triangle with the extended structure of the BBS2 platform and α-helical domains forming a bridge between the base and the top.

Effects of BBS-linked mutations

Multiple point mutations in BBS2, BBS7 and BBS9 have been linked to Bardet-Biedl syndrome [83, 86-94]. To understand how these mutations might result in BBS, we measured the effect of 14 of these mutations on the formation of the BBSCC. BBS2, BBS7 and BBS9 were co-expressed in HEK-293T cells and the co-immunoprecipitation of BBS7 and BBS9 with BBS2 was determined. None of the mutants changed the co-immunoprecipitation of BBS7 with BBS2 (**Figure 2.6 A** and **B**). However, the BBS2 R632P mutant and the BBS9 G141R mutants showed a marked decrease in the co-immunoprecipitation of BBS9 with BBS2. The decrease in co-immunoprecipitation of BBS9 in the G141R mutant was a result of decreased cellular expression. Quantification of the BBS9 bands from cell lysates showed that expression of the G141R mutant was decreased by 80 % compared to the expression of wild-type BBS9. In contrast, expression of the BBS2 R632P mutant was similar to wild-type BBS2, indicating that the mutation did not impair the expression of BBS2, but that it disrupted the interaction between BBS2 and BBS9.

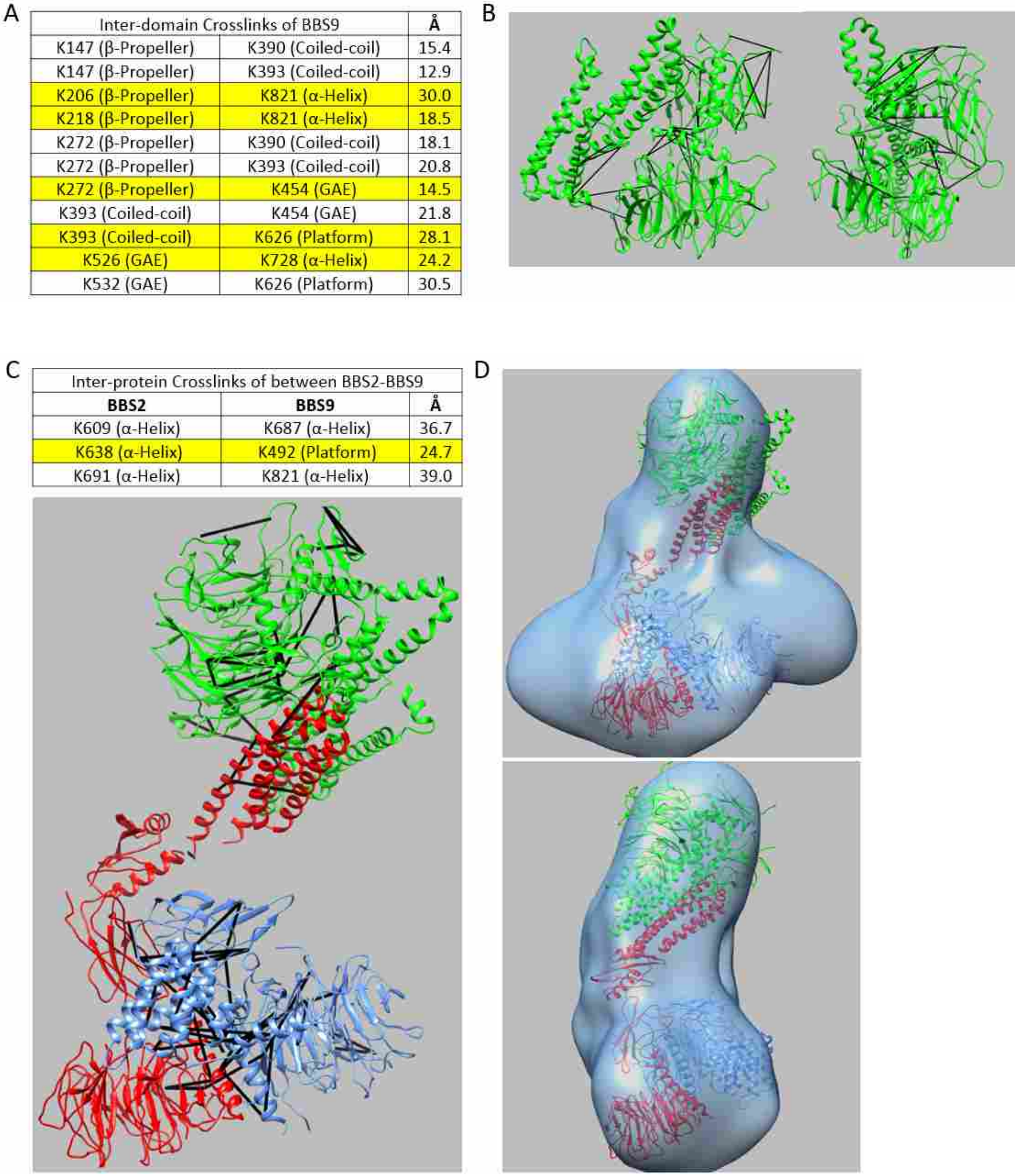

Inter-domain Crosslinks of BBS9		Å
K147 (β-Propeller)	K390 (Coiled-coil)	15.4
K147 (β-Propeller)	K393 (Coiled-coil)	12.9
K206 (β-Propeller)	K821 (α-Helix)	30.0
K218 (β-Propeller)	K821 (α-Helix)	18.5
K272 (β-Propeller)	K390 (Coiled-coil)	18.1
K272 (β-Propeller)	K393 (Coiled-coil)	20.8
K272 (β-Propeller)	K454 (GAE)	14.5
K393 (Coiled-coil)	K454 (GAE)	21.8
K393 (Coiled-coil)	K626 (Platform)	28.1
K526 (GAE)	K728 (α-Helix)	24.2
K532 (GAE)	K626 (Platform)	30.5

Inter-protein Crosslinks of between BBS2-BBS9		
BBS2	**BBS9**	**Å**
K609 (α-Helix)	K687 (α-Helix)	36.7
K638 (α-Helix)	K492 (Platform)	24.7
K691 (α-Helix)	K821 (α-Helix)	39.0

Figure 2.5 The structure of the BBSCC A) BBS9 inter-domain crosslinks. 11 BBS9 inter-domain crosslinks are shown in the table with residue numbers, domains, and the distances. Yellow rows show the crosslinks also formed by DSG crosslinking though all crosslinks listed in this figure except K526-K728 were formed by DSS. B) BBS9 structure (green) based on XL-MS. Black lines indicate the crosslinks. C) BBS9 inter-protein crosslinks and BBSome core structure based on XL-MS. D) The BBSCC docked into the EM density.

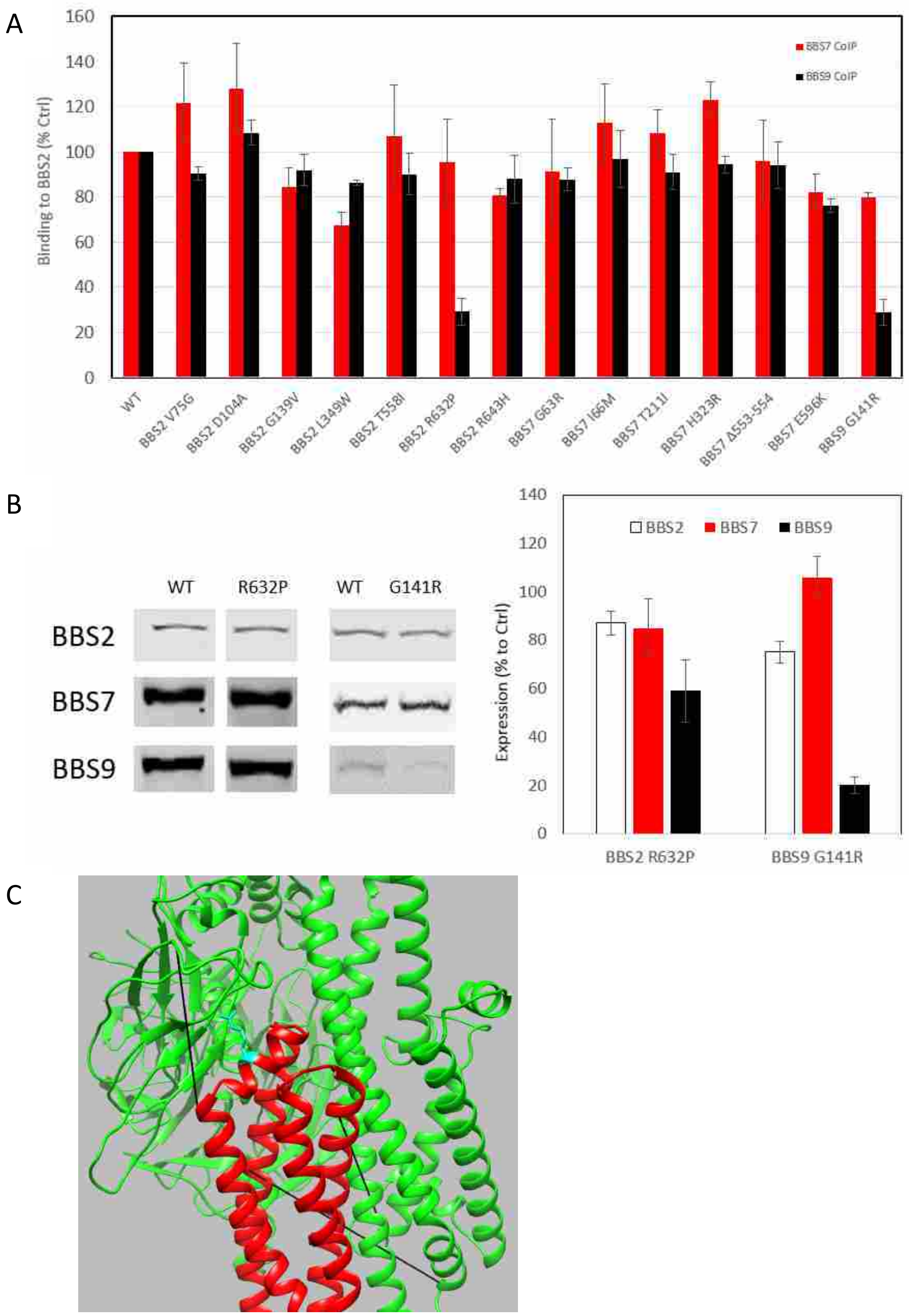

Figure 2.6 Effects of mutations on BBSome core assembly A) The effects of mutations in BBS2, 7 and 9 linked to the disease on BBSCC formation were measured. HEK-293T cells were co-transfected with c-Myc-tagged wild type or mutant BBS2, FLAG-tagged wild type or mutant BBS7, and Flag-tagged wild type or mutant BBS9. BBS2 was immunoprecipitated with anti-c-Myc antibody, and BBS2, 7, and 9 were detected and quantified by immunoblotting. The graph shows co-immunoprecipitation of BBS7 (red bars) and BBS9 (black bars) normalized to the wild-type. B) Expression level of BBS2 R632P and BBS9 G141R in cell lysate normalized to the wild-type. (BBS2: white bars, BBS7: red bars, and BBS9: black bars). Data represent the average ± SEM of at least three experiments. C) BBS R632 position. The BBS causing mutation BBS2 R632P (cyan) is located at the interface of BBS2 (red) and BBS9 (green).

Discussion

Solving the molecular structure of the BBSome will contribute considerably to understanding the mechanism by which the BBSome transports of cargos within the primary cilium. As an initial step, we have probed the structure of the BBSCC using EM, XL-MS, unnatural amino acid crosslinking, and site-directed mutagenesis. Reconstruction of single particle EM images of the core complex reveal a relatively flat, triangular shape that would be suitable as a platform structure upon which the other BBSome subunits or cargos could associate (**Figure 2.1**). The XL-MS and UAA-XL data show that BBS2 and BBS7 form a dimer that associates via a coiled-coil interaction between residues 333-363 of BBS2 and residues 339-376 of BBS7 (**Figure 2.3**). The XL-MS data also show that BBS9 associates with BBS2 via interactions between the BBS2 α-helical domain and the BBS9 platform and α-helical domains.

BBS1 has a similar domain structure to BBS2, 7 and 9 with an N-terminal β-propeller, followed by a coiled-coil and a GAE domain [47], and BBS1 has been shown to interact strongly with BBS9 [73]. Given the conserved coiled-coil of BBS1, it is interesting to speculate that BBS1 interacts with BBS9 via a coiled-coil interaction. BBS9 also interacts with BBS5 and BBS8, acting as a hub for BBSome assembly [42, 73]. It is not clear from the core complex structure where the sites of BBS5 and BBS8 interaction are located, but they would not be found in the BBS9 α-helical domain where BBS2 binds, nor in the coiled-coil domain where BBS1 may bind. It seems likely that BBS5 or BBS8 would bind the β-propeller domain of BBS9, given its accessibility in the core complex structure.

Our data provide insight into the molecular basis of BBS disease caused by the BBS2 R632P mutation. The interaction of this mutant with BBS9 is strongly inhibited, while its binding to BBS7 is not. The reason for the disruption can be seen in the predicted interaction surface between the α-helical domain of BBS2 with the platform and α-helical domains of BBS9. Residues 628-635 of BBS2 are expected to form a short α-helix that is located in the contact region between BBS2 and BBS9 (**Figure 2.6 C**). High confidence crosslinks between lysines 638, 609 and 691 of the BBS2 α-helical domain with lysine 492 of the BBS9 platform domain and lysines 687 and 821 of BBS9 α-helical domain, respectively, direct this short α-helix into a cleft between the platform domain and the α-helical domain of BBS9 (**Figure 2.6 C**). The R632P mutation would disrupt this short helix, which would in turn destabilize the interactions occurring at this interface.

Previous work has shown that the G141R mutation disrupts the folding of the BBS9 β-propeller and inhibits the expression of the mutant protein [83]. We also see decreased expression of the BBS9 G141R mutant that results in decreased binding of BBS9 to BBS2. The other mutants found in BBS2, 7 and 9 do not disrupt formation of the BBSCC, suggesting that they might contribute to BBS in some other way by interfering with the association of the other BBSome proteins or BBSome cargos with the core.

In summary, this structural analysis provides a view of the overall structure of the BBSCC, consisting of BBS2, BBS7 and BBS9, and identifies key interactions that bring the components of the core complex together. Moreover, it provides a molecular basis for Bardet Biedl syndrome caused by the BBS2 R632P mutation. These studies show how structural information can inform our understanding of the BBSome and how its malfunction causes disease.

CHAPTER 3: MTOR SIGNALING AND MTORC ASSEMBLY

Summary

The mechanistic target of rapamycin (mTOR) serine/threonine kinase has important signal transduction roles in eukaryotic organisms. mTOR forms two compositionally and functionally distinct protein complexes (mTORC1 and 2) that detect intra- and extra-cellular signals, such as nutrients, growth factors and hormones to control cell size, cell division and survival via regulation of transcription, translation and metabolism. The mTOR complexes consist of multiple subunits that must assemble from their individual subunits. The process of mTOR complex assembly is mediated by chaperone proteins, which are critical for controlling production of functional proteins in the cell by assisting in their folding and association with their binding partners. A key component of the cell's chaperone machinery is the cytosolic chaperonin containing tailless polypeptide 1 (CCT). CCT accounts for folding of about 10 % of the proteome in the eukaryotic cytosol. Some of these CCT substrates are folded with the assistance of phosducin-like protein 1 (PhLP1), a CCT co-chaperone. Several observations link CCT to mTOR signaling. First, protein components in the mTOR complexes, mammalian lethal with Sec13 protein 8 (mLST8), regulatory associated protein of mTOR (Raptor), and rapamycin-insensitive companion of mTOR (Rictor), have 7-bladed β-propeller domains that are a unique structural feature found in many CCT substrates. The mLST8 subunit in particular shows

sequence and structural homology to the β subunit of heterotrimeric G proteins (Gβ), a known CCT substrate. In fact, mLST8 has also been named Gβ-like protein (GβL). Second, over-expression of CCT subunits rescues LST8 and TOR mutant phenotypes in yeast. Third, an interaction between CCT and mLST8 has been reported in an autophagy interactome study. Motivated by these evidences, we explored the possibility that CCT was involved in mTOR signaling through the folding and assembly of mLST8, and possibly Raptor and Rictor, into the mTOR complexes.

Introduction

mTOR signaling

mTOR is a large (290 kDa) protein kinase that regulates cellular signal transduction [95]. mTOR responds to extra-cellular stimuli such as insulin and other growth factors and also to changes intra-cellular conditions such as redox and nutritional status. mTOR serves as a main regulator of cell size, cell division, and cell survival through its regulation of protein translation, lipid and nucleotide synthesis, mitochondrial proliferation and autophagy. As its name suggests, mTOR activity is sensitive to rapamycin, a metabolite isolated from soil bacteria. Rapamycin and other drugs derived from rapamycin have been extensively studied, and these investigations have led to the use of mTOR inhibitors as immune-suppressant and anti-cancer drugs. The highlight of mTOR function is to amplify the cell's ability to grow and divide by triggering cytoskeleton reorganization, ribosome biogenesis and initiating protein synthesis. These properties make mTOR a high-value drug target. Indeed, mTOR function must be strictly regulated, otherwise excessive mTOR activity leads to uncontrolled cell proliferation and cancer.

mTORC1 and mTORC2

mTOR forms two types of structurally and functionally distinct protein complexes with other subunits (mTORCs) [96]. mTORC1 is a hetero-oligomer that consists of mTOR, mLST8, Raptor, and other non-core components (**Figure 3.1 A and C**). Another mTOR complex, mTORC2, is also a hetero-oligomer that consists of mTOR, mLST8, Raptor independent companion of mTOR (Rictor), mammalian stress-activated protein kinase interacting protein 1 (mSIN1), and other non-core components (**Figure 3.1 B and D**) [97]. Despite the presence of mTOR with mLST8 in both complexes, mTORC1 and mTORC2 behave quite differently. For example, while mTORC1 is sensitive to rapamycin, fully assembled mTORC2 doesn’t bind rapamycin [98, 99]. In addition, their localization in cell is quite distinct. mTORC1 is found predominantly in the cytoplasm, whereas mTORC2 is found in the nucleus and plasma membrane as well as the cytoplasm [100-102]. While depletion of Raptor impairs T-lymphopoiesis and causes death of T-cell acute lymphoblastic leukemia cells, Rictor loss doesn’t cause the same effect [103]. Loss of Rictor selectively abolished the NKT17 lineage of iNKT cells, but Raptor and Rheb, mTORC1 regulators, are found to be dispensable for NKT17 differentiation [104]. The fate of mTOR is determined by Raptor (mTORC1) and Rictor (mTORC2). These subunits compete for mTOR binding as evidenced by the fact that Rictor over-expression disrupted Raptor binding to mTOR [105]. Deep understanding of the structural and functional specificity of each complex will directly lead to more effective and specific strategies to therapeutically target mTOR signaling.

The mTOR kinase

mTOR is a member of the phosphatidylinositol-kinase-related kinase (PIKK) family which includes the protein kinases ATM, ATR, SMG1, TRRAP, and DNA-PKcs [106]. Like other PIKK family members, mTOR has N-terminal HEAT (Huntingtin, EF3A, ATM, TOR) repeats, which serve as the binding sites for the regulatory proteins and components of each mTOR complex (**Figure 3.1 C**) [107-109]. The HEAT domain is followed by a FAT (FRAP, ATM, TRRAP) domain and the kinase domain. The FAT domain consists of 28 α-helices which are divided into three sets of tetratricopeptide repeats (TRD1-3) and a HEAT domain. The FAT domain makes intra-molecular contacts with the kinase domain through conserved residues (E1401-R2317, R1905-E2419, and Q1941-E2200), and these interactions contribute to the structure and function of mTOR (**Figure 3.1 C**) [110]. N-terminal HEAT and FAT occupies roughly four-fifths of the primary sequence of mTOR, and these domains are critical in dimerization of both mTORC1 and mTORC2 [111, 112].

The kinase domain (KD) has about 550 amino acids and forms an N- and C-terminal lobes structure typical of protein kinases. The crystal structure of N-terminal truncated mTOR with mLST8 reveals that ATP binds to a cleft created by these lobes as seen with other kinase domains [110]. The kinase domain N-lobe contains an ~100-amino-acid FRB (FKBP12 rapamycin binding) domain. FRB makes mTOR unique in the PIKK family by providing binding sites for the FKBP12-rapamycin complex [107]. The FRB domain recruits mTOR substrates and directly regulates mTOR activity by gating its active site from substrates [110].

mTOR associates with its obligate binding partner, mLST8, through a 40-residue LST8 binding element (LBE) of the kinase domain C-lobe (discussed below). mLST8 binding further restricts the active site by creating a deep crevice 37 Å deep and only 8 Å wide at the narrowest point between the FRB domain in the N-lobe and mLST8 bound to the LBE in the C-lobe [110]. There are six phosphorylation sites on mTOR (S1261, S2159, T2164, T2446, S2448, and S2481), and five of them are concentrated in the kinase domain (**Figure 3.1 C**) [107, 113].

Insulin-PI3K pathway mediated S1261 phosphorylation is observed in both mTORC1 and mTORC2 [114]. In mTORC1, S1261 phosphorylation promoted phosphorylation of ribosomal protein S6 kinase (S6K) and eukaryotic translation initiation factor 4E-binding protein (4EBP). Likewise, phosphorylated S2159 and T2164 enhances mTORC1 signaling to S6K and 4EBP to promote cell growth and cell progression [115]. T2446 responses to energy and nutrients level and is possibly phosphorylated via adenosine monophosphate kinase (AMPK) though it has been reported that the site is constitutively phosphorylated in breast cancer cells with an amplified S6K gene, while this phosphorylation is not observed in a less tumorous cell lines [105, 116, 117]. S2448 is phosphorylated by S6K, and phosphorylation of the site seems to be mTORC1 specific [114, 117, 118]. Mutations on T2446/S2448 impairs mTOR signaling to its downstream effectors. S2481 is autophosphorylated in both mTORC1 and mTORC2. Whereas S2481 phosphorylation in mTORC2 is rapamycin insensitive, it becomes sensitive after prolonged treatment with rapamycin [114, 115, 119]. Phosphorylation on S1261, Rheb overexpression, and insulin stimulation promote S2481 autophosphorylation [119].

The last 35 amino acids of mTOR forms a FATC domain (FAT domain at C-terminus). FATC is commonly seen in the structure of PI3K and other PIKKs [120, 121]. The fact that FATC interacts with the activation loop on the kinase domain indicates that FATC may support mTOR's kinase activity by stabilizing the activation loop. Indeed, the sequence of the FATC and activation loop is well-conserved among PIKK family members [110].

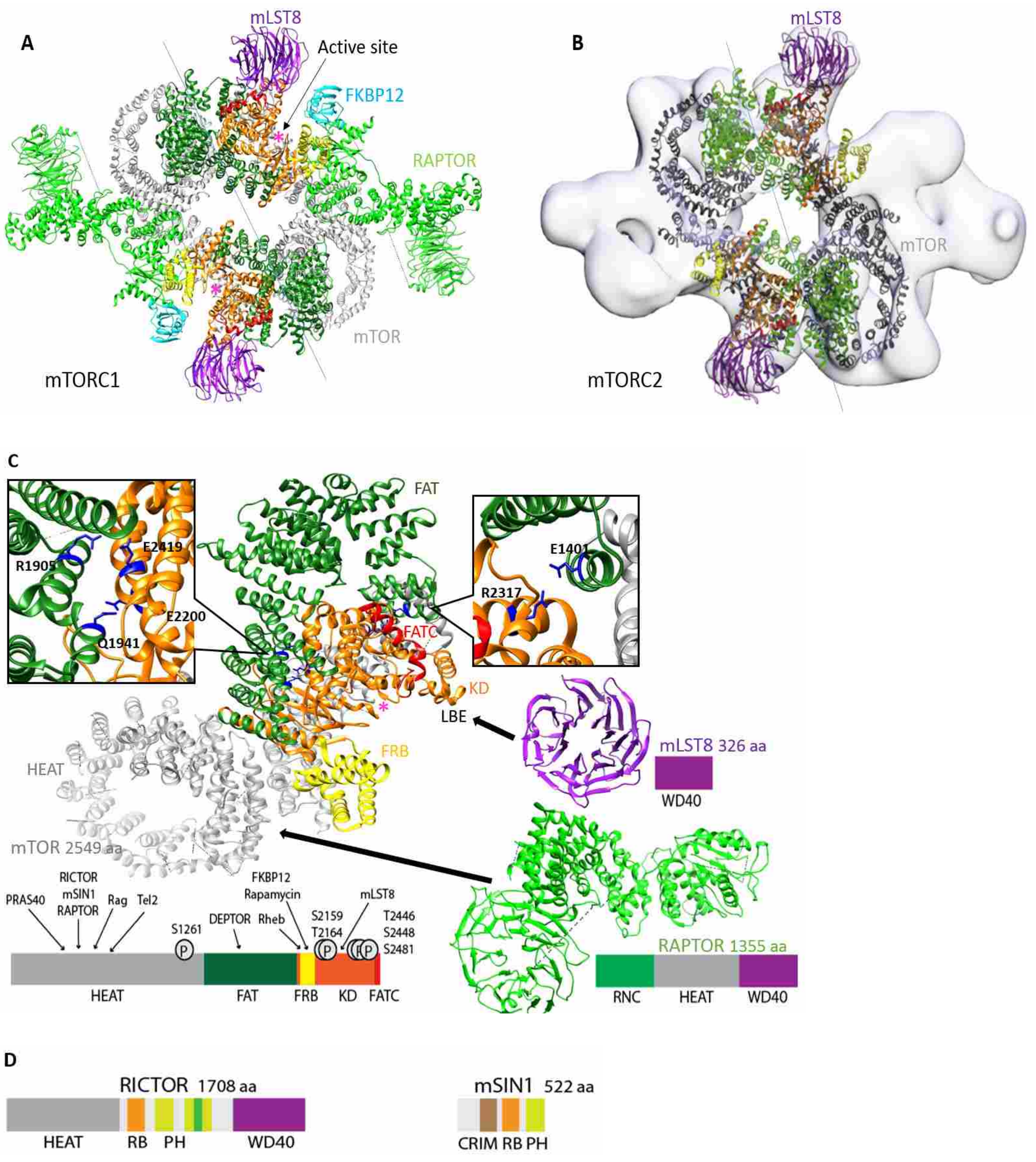

Figure 3.1 Structures and domain maps of mTORC components A) The atomic structure model of mTORC1 reveals symmetrically dimerized sub-complexes each consists of mTOR (HEAT: gray, FAT: dark green, FRB: yellow, KD: orange, FATC: red), mLST8 (purple), and Raptor (green). FKBP12 (light blue) binds to FRB domain of KD affecting the activity of mTOR with rapamycin. The pink asterisk indicates the active site. B) The atomic model of the dimer of mTOR-mLST8 complex is superimposed on the TORC2 reconstruction [112]. C) Structural domain maps of mTORC1 components. The zoomed in windows depict FAT-KD interaction through conserved residues (blue) in mTOR. The total number of amino acid in human mTORC genes are shown after each name. Six phosphorylation sites and binding sites for mTOR binding partners are indicated on the mTOR domain map. The WD40 domain is seen in mLST8 and Raptor models. D) Domain maps of Rictor and mSIN1. PDB ID: 5FLC [111]

mLST8

Though mLST8 is well-characterized as an integral core component of mTORCs, its functions have not been well-understood until recently. mLST8 forms seven WD40 repeats, and the structure is highly homologous to the Gβ, hence its other name Gβ-like (**Figure 3.1 C**). We will discuss the similarity between mLST8 and Gβ and its implications later in this chapter. Recent structures provide insight into the role of mLST8 in mTOR complexes. First, the interaction of mLST8 with the LBE of the C-lobe increases the stability of the kinase domain as evidenced by the increased solubility of the over-expressed kinase domain when mLST8 was co-expressed [110], and loss of mLST8 leads to the association of mTOR with heat-shock proteins [122]. As a result, mLST8 is essential for mTOR kinase activity. Second, the crystal structure of the mLST8-mTOR complex reveals that mLST8 restricts access to the kinase domain active site as described in the previous section [122]. Third, mLST8 depletion in cancer cells reduced the formation of both mTORC1 and mTORC2 [123]. In the same study, while depletion of mLST8 diminished mTORC2-mediated phosphorylation of AKT in both normal and cancer cells, mTORC1-mediated phosphorylation of 4EBP was inhibited in cancer cells but not in normal cells, implicating that mLST8 has a distinct function in cancer cells. This idea is supported by other experiments done in non-tumor cells which showed normal proliferation under low mLST8 conditions [124]. These reports conclude that mLST8 as an essential component of mTOR complexes even though the impact of loss of mLST8 seems different between mTORC1 and mTORC2.

mTORC1 components

Raptor is the 150 kDa defining factor of mTORC1 and binds to the N-terminal HEAT domain of mTOR (**Figure 3.1 C**). Raptor protein consists of RNC (Raptor N-terminal

Conserved) domain, armadillo repeats, and a C-terminus WD40 repeat β-propeller domain [111, 125]. Raptor seems more important in controlling the substrate recruitment, substrate specificity, direction of the subcellular localization and catalytic activity of mTORC1, than contributing to the formation of the mTOR dimer complex. This observation stems from several cryo-EM analyses demonstrating a stable dyad-symmetry dimer of mTOR-mLST8 heterodimers in the absence of Raptor [107]. In contrast, many key mTORC1 substrates in mTORC1 signaling such as S6K, 4EBP and PRAS40 bind to Raptor directly. Raptor serves as a scaffold for PRAS40, a subunit of mTORC1 that regulates mTOR activity [105, 126, 127]. Sequence analysis reveals that PRAS40 contains two mTORC1 binding motifs, the TOS (TOR signaling) motif and the RAIP motif (named after an amino acid sequence in 4EBP1). PRAS40 exerts inhibition on mTORC1 with DEPTOR (DEP domain containing mTOR-interacting protein), another accessory protein for both mTORCs, and activated mTORC1 phosphorylates both PRAS40 and DEPTOR that results in dissociation of both components [126]. Moreover, PRAS40 phosphorylation by AKT at T246 also releases its inhibition on mTOR [126, 127].

mTORC2 components

Rictor is an obligatory component and serves as a scaffold protein in mTORC2, sharing the same binding site on mTOR with Raptor (**Figure 3.1 C**) [105, 128]. Rictor (~ 200 kDa) is the second largest component in mTORC2. Sequence alignment of conserved regions of Rictor reveals that Rictor seems to have HEAT, WD40, PH (pleckstrin homology) and ribosome binding (RBD) domains (**Figure 3.1 D**). The HEAT and WD40 domains indicate structural similarity to Raptor, possibly suggesting a shared folding chaperone and mTOR binding motif, and the PH and ribosome binding domains point to its localization and downstream targets [128]. Another mTORC2 specific component, mSIN1, has a PH domain at its C-terminus as well. This

500 amino-acid-protein consists of NTD (N-terminal domain), CRIM (conserved region in middle), RBD (Ras-binding domain), and PH domain [129]. mSIN1 interacts with other mTORC2 components through the NTD, and without the NTD, functional mTORC2 is not assembled [130]. mSIN1 is known to inhibit the activity of MEKK2, JNK, and RAS, by directly binding to their catalytic center [130-133]. Similarly, mSIN1 binds to mTOR's kinase domain mainly through the PH domain, even without Rictor, and inhibits mTOR catalytic activity [132].

mTORC1 signaling

Activation of mTORC1 is initiated in response to nutrients, cellular stresses, amino acids, and growth factors, which trigger distinct signaling pathways (**Figure 3.2**) [127, 134]. Extracellular signal-required kinase (ERK) and Wnt pathways have also been suggested to signal upstream of mTORC1 [135, 136]. External stimuli such as insulin and insulin-like growth factors (IGF) activate class I phosphatidylinositol-4,5-bisphosphate 3-kinase (PI3K), and PI3K produces phosphatidylinositol (3,4,5)-triphosphate (PIP3) by phosphorylating phosphatidylinositol (4,5)-bisphosphate (PIP2) on the plasma membrane. The target of PIP3 is the PH domain of AKT and 3-phosphoinositide dependent protein kinase-1 (PDK1). Association with PIP3 brings AKT to the plasma membrane where it meets PDK1, which in turn phosphorylates and activates AKT. For AKT's full kinase activity, two of AKT's phosphorylation sites, Thr308 and Ser473, have to be phosphorylated. Thr308 is phosphorylated by PDK1, and Ser473 is phosphorylated by mTORC2. Activated AKT inhibits the tuberous sclerosis complex (TSC), consisting of TSC proteins 1 and 2, by phosphorylating TSC2. In its active form, TSC acts as a GTPase activating protein for the small GTPase Rheb, an activator of mTORC1. AKT phosphorylation-dependent inactivation of TSC allows the accumulation of Rheb-GTP, which in turn binds and activates mTORC1 [137]. Since Rheb resides on the surface of the lysosome, mTORC1 is recruited to lysosome for activation [138]. Lysosomal translocation and activation of mTORC1 is also a key step in amino acid-dependent mTOR signaling pathways, which employs a different GTPase, Rag, to recruit mTOR to the surface of the lysosome [139]. Recruitment of mTORC1 to lysosomes by both Rheb-GTP and Rag-GTP has been proposed to work together to increase mTORC1 activation [139]. Rag-GTP only acts to recruit mTORC1 to the lysosomal membrane, while Rheb-GTP both recruits and activates mTORC1.

Upon activation, mTORC1 phosphorylates its downstream targets 4EBP and S6K. Prior to phosphorylation by mTORC1, 4EBP represses translation by binding to eIF4E and preventing other translation components to form the initiation complex. Once mTORC1 phosphorylates threonines 36 and 45, 4EBP is incapable to associate with eIF4E, thus eIF4G (a scaffold protein), eIF4A (an ATP-dependent RNA helicase), eIF4B, the 40S subunit of ribosome, and other components are allowed to form the initiation complex at the 5' end of most mRNAs and initiate protein translation. In the absence of growth factors, mTORC1 doesn't phosphorylate 4EBP, and the translation initiation complex remains inhibited by 4EBP [127, 137, 140]. In the case of S6K, when mTORC1 phosphorylates threonine 389, S6K phosphorylates its downstream effectors, stress-activated protein kinases (SKAR), eIF4B, eEF2K, and 40S ribosomal protein S6 (S6), to promote protein translation, ribosome biogenesis, and regulation of both catabolic and anabolic metabolism [137, 141].

TSC can also be activated by AMPK phosphorylation in response to cellular energy depletion or DNA damage, or by REDD1 expression in response to hypoxia [127, 142-145]. Activation of TSC leads to decreased Rheb-GTP and inactivation of mTORC1. Thus, TSC integrates multiple cellular signals to generate an appropriate response by mTORC1.

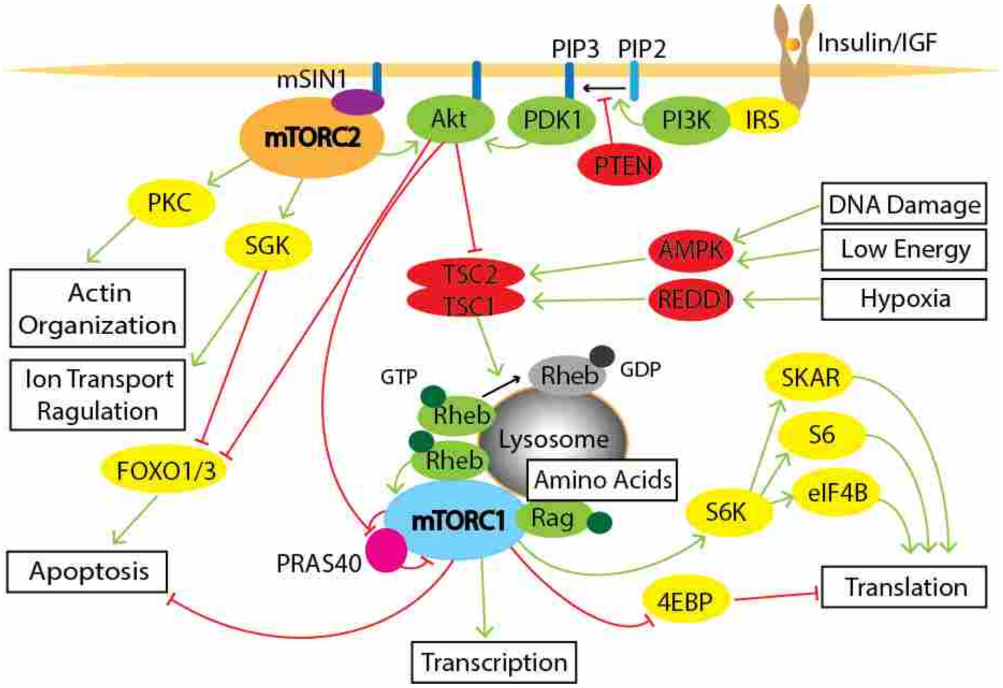

Figure 3.2 The mTOR signaling pathway The mTOR signaling cascade is depicted. Growth factors such as insulin activate receptors, and the signal is propogated to activate PI3K, which produces PIP3 to recruit PDK1 and AKT. Upon activation by PDK, AKT phosphorylation inhibits the TSC1/2 complex which negatively regulates accumulation of GTP-Rheb, the mTOR activator. Lysosomal localization of mTORC1, which is necessary for mTORC1 activation, is promoted by GTP-Rheb and amino acid-sensing Rag GTPase. Activated mTORC1 upregulates cell growth, transcription, and translation through effectors such as S6K and 4EBP and inhibits apoptosis and autophagy. Cellular stresses such as DNA damage, low energy state, and hypoxia, negatively affects mTORC1 activity through proteins such as AMPK and REDD1. For the activation of mTORC2, inhibition of mSIN1 must be relieved through interaction with PIP3, the product of PI3K. Activated mTORC2 phosphorylates its effectors such as AKT, PKC, and SGK, to promote cell growth and survival.

mTORC2 signaling

Compared with mTORC1, the mTORC2 signaling pathway has been less investigated. Although activation by RAS, AKT, S6K, mTOR, GSK3β, and mTORC2 auto-phosphorylation are implicated as its regulators, the mechanism of mTORC2 activation is not fully understood [118, 146-150]. However, it is certain that extracellular cues such as growth factors and insulin can activate mTORC2 [132, 134]. Supporting this idea, production of PIP3 in response to PI3K activation by growth factor receptors has been shown to activate mTORC2 [132, 151]. The PH domain of mSIN1 in mTORC2 is the key to this activation (**Figure 3.2**). The kinase domain of mTOR in mTORC2 is blocked by the PH domain of mSIN1 until mTORC2 is recruited to plasma membrane by PIP3. Upon PIP3 binding, the PH domain of mSIN1 is reoriented by PIP3, opening up the mTOR active site for substrate phosphorylation. This proposed mechanism is consistent with the fact that AKT is one of the downstream targets of mTORC2. Activated mTORC2 is essential for cell survival and transformation of cancer cells by activating AGC kinase family members such as AKT to promote pro-survival pathway, protein kinase C-α (PKCα) to control cytoskeletal organization, and glucocorticoid-induced protein kinase 1 (SGK1) to regulate ion transport [127, 134, 152, 153]. AKT is positioned upstream of mTORC1 (down-regulating PRAS40, TSC1, and TSC2) and downstream of mTORC2, indicating that mTORC1 and mTORC2 are tightly related to control cell growth through AKT. When AKT is activated by mTORC2, similar consequences such as cell survival and proliferation are observed. In spite of this, only mTORC2 specific phosphorylation on S473 of AKT results in regulation of FOXO1/3. Phosphorylation on FOXO1/3 by AKT prevents apoptosis [112]. As mentioned above, mTORC2 is insensitive to rapamycin, but its activity depends on the PIP3 level. Therefore, a drug targeting both PI3K and mTOR kinase activity can have a massive impact on tumor cells. In fact, PTEN (phosphatase and tensin homolog), a lipid phosphatase that hydrolyzes PIP3 into PIP2, is frequently mutated in tumor cells [154].

Chaperones and mTORC assembly

Whether in healthy cells or tumor cells, proliferation and proteome homeostasis are strictly regulated by chaperones, which play crucial roles in protein folding, assembling functional protein complexes and protein degradation processes. Well known chaperone systems such as heatshock protein (HSP) 70/90, and chaperonin systems form a chaperone network that controls the proteome of cells [155]. It is not surprising that the assembly of a large protein complex like mTORCs is also supported by a chaperone system. Folding of the mTOR kinase and other PIKKs and their assembly of the functional complexes is mediated by HSP90 system and the TTT-R2TP (Tel2-Til1-Til2 and Rvb1/2-Tah1-Pih1) complex as a co-chaperone [106, 156, 157]. Tel2 preferentially interacts to newly synthesized PIKKs, rather than in their matured state, and brings those nascent peptides to HSP90 through the R2TP complex [106, 157]. Depletion of Tel2 diminishes the interaction of newly synthesized mTOR with Raptor, Rictor and mLST8, indicating that Tel2 plays an integral role in the assembly of both mTORC1 and mTORC2. Moreover, rapamycin is found to acutely inhibit assembly of newly synthesized mTOR into mTORC2 whereas rapamycin partially affects mTORC1 assembly. This observation is consistent with the finding that mTORC2 activity, AKT activity and cell survival is not sensitive to rapamycin until prolonged dosage, which reduces the number of functional mTORC2 complexes to below that needed to maintain cell survival through AKT signaling [98]. Association of the TTT complex and the R2TP complex is essential to achieve mTORC1 dimerization, and this process is done in an energy-dependent manner through WAC (WW domain containing adaptor with coiled-coil) [156]. However, the information of how other subunits in mTORC1 are folded and assembled is not known.

CCT—possible chaperone for mTORC components

One characteristic commonly seen in some of the mTORC components is that mLST8, Raptor and Rictor have WD40 domains that form β-propeller structures [127, 128]. In the case of mLST8, which is an essential component in both mTORC1 and mTORC2, its entire structure consists of one WD40 domain that is a close structural homolog of the G protein β subunit. Gβ1 is folded and assembled into an obligate Gβγ dimer through the chaperonin CCT. Interestingly, CCT binds and folds a number of substrates with β-propeller structures, suggesting that CCT contributes to mTOR signaling by folding and assembling mLST8 into mTOR complexes [44, 158-160]. The WD40 domain of Raptor and Rictor are also possible CCT substrates since proteins with complex folding patterns like the WD40 domain cannot achieve their native state without chaperones [161].

mTOR signaling and CCT

A link between mTOR and CCT has been reported in a study investigating the physiological effects of individual CCT subunits in yeast [162]. In that study, when the CCTζ subunit was over-expressed, LST8 and TOR mutant phenotypes were suppressed, indicating that deficient mTORC could be rescued by CCT activity. Furthermore, an mLST8-CCT interaction was detected in an autophagy interactome study by mass-spectrometry [163]. Finally, feedback regulation of CCT activity by mTORC1 was implied by a study demonstrating that S260 of the β subunit of CCT is phosphorylated by S6K, a main phosphorylation target of mTORC1 [164]. Such information led us to investigate the relationship between mTORCs and CCT.

CCT

CCT is known to fold actin, tubulin, Gβ and many other cytosolic substrates important for cellular function [165]. Mutations in CCT cause a retinal-degenerative genetic disorder, Leber Congenital Amaurosis (LCA), and autosomal recessive sensory neuropathy [166, 167]. Additional substrates of CCT include p53, programmed cell death 5 (PDCD5), signal transducer and activator of transcription 3 (STAT3), and von Hippel Lindau tumor repressor (VHL), indicating that CCT is linked to cancers [168-171]. Tumorigenesis is promoted by mutation in the CCT binding site on VHL. The function of CCT is not only limited to folding but also participating in protein degradation process by cooperating with ubiquitin, proteasome, and autophagy pathways [172-175].

CCT is a large protein complex of roughly 1 MDa with a barrel-like structure that consists of two identical rings stacked on top of each other, each ring containing eight different subunits (CCT1-8) (**Figure 3.3 A and B**) [43]. Each CCT subunit is paralogous, and they share 30 % sequence homology and very high structural homology [176]. The individual CCT subunits are L-shaped structures that consist of three domains, an equatorial region in the bottom part of the L shape where ATP binds and is hydrolyzed, an apical region of the top part of the L shape which serves as a main substrate binding site, and an intermediate region between the other two domains that translates ATP binding and hydrolysis into conformational changes in the apical region that facilitate CCT's folding function (**Figure 3.3 C**). When the nucleotide binding pocket is empty or bound to ADP, CCT adopts an open conformation in which the apical regions of CCT subunits are spread out and protein substrates have access to the folding cavity. ATP binding induces conformational changes in the apical domain of CCT subunits to close the folding cavity and trap CCT substrates within the cavity, isolating them from the cellular environment [177]. ATP-hydrolysis reverses the conformational change and opens the apical domains. This open and closed conformational cycle may be repeated multiple times until the substrate achieves its fully native state. CCT opening induced by ATP-hydrolysis allows the substrate to escape from CCT when it has achieved its native fold and/or when an appropriate release factor is present.

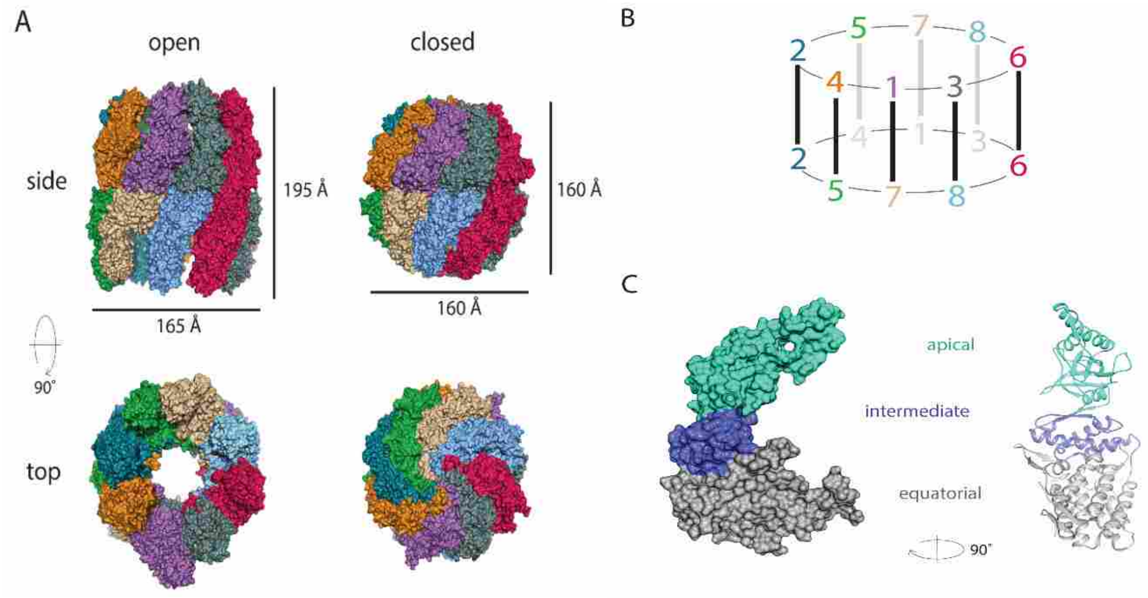

Figure 3.3 Architecture of CCT A) Structure of the open (left) and closed (right) conformation of mammalian CCT [161]. Top and side views are shown. B) Orientation of the CCT subunits (CCT1-8). C) A single CCT subunit has apical, intermediate, and equatorial domains.

CCT is the eukaryotic counterpart of the GroEL/GroES chaperonin system in bacteria. The 800 kDa homo-heptameric GroEL chaperonin complex is functionally and structurally similar to CCT [178]. However, CCT has more chemically diverse binding surface than GroEL because of its eight different subunits. As a result, CCT is capable of binding and folding approximately 10 % of the eukaryotic proteome [43, 46]. A recent study reveals that CCT subunits have different and unique substrate binding properties [179]. CCT subunits are circularly oriented in a clockwise direction, 1 (alpha), 4 (delta), 2 (beta), 5 (epsilon), 7 (eta), 8 (theta), 6 (zeta), and 3 (gamma), in order (**Figure 3.3 B**). The CCT surface containing subunits gamma, zeta, and theta has weaker affinity for ATP and greater affinity for substrate binding. On the contrary, the opposite side of the CCT ring which containing subunits beta, delta, and epsilon, has the high ATPase activity and weaker affinity for CCT substrates. Such diverse chemical properties among its subunits allows CCT to interact with various proteins and participate in the folding of many proteins involved in multiple cellular processes.

PhLP1 as a co-chaperone of CCT

Like GroEL which has its co-chaperone GroES, there are also CCT co-chaperones, such as PhLP1, but unlike GroEL, CCT doesn't require co-chaperones for all folding processes. PhLP1 is a structurally flexible phosphoprotein with an N-terminal helical region and C-terminal domain with a thioredoxin fold [180]. PhLP1 plays a key role in production of the heterotrimeric G protein and G protein signaling by directly binding to both CCT and the nascent Gβ subunit, assisting in Gβ folding, and delivering folded Gβ to Gγ to form the Gβγ dimer [44]. In the process of Gβ folding, PhLP1 binds to the CCT apical domains to cover the folding cavity in a manner analogous to GroES binding to GroEL. Though Gβ can bind CCT either in the presence or absence of PhLP1, the nascent Gβ polypeptide will not progress through the folding process without PhLP1. Therefore, formation of the PhLP1-Gβ-CCT ternary complex is necessary for production of a stable Gβ subunit [44]. The main role of PhLP1 in this process seems to be to facilitate the final folding steps of Gβ by closing the seven-blade propeller and releasing Gβ from CCT [44, 181, 182].

Conclusion

The structural similarity between Gβ and mLST8, the reported interaction between mLST8 and CCT, and the links between mTOR signaling and CCT lead us to hypothesize that CCT is involved in mTOR signaling through folding and production of stable mLST8. If mLST8 is a CCT substrate, PhLP1 could also contribute as a co-chaperone. Since PhLP1 is essential not only in the folding of CCT substrates like Gβ, but also in linking the substrate to its destination complex, the assembly process of mTORCs could also involve PhLP1. To test these possibilities, we assessed the contribution of CCT and PhLP1 in mTORC1 and mTORC2 assembly through a series of biochemical and functional experiments. We also isolated complexes of mLST8-CCT and PhLP1-mLST8-CCT as intermediates in the process of mLST8 folding and probed mLST8-CCT structure by cryo-EM and chemical crosslinking coupled with mass spectrometry. Another β-propeller containing mTORC1 component, Raptor, was discovered to interact with CCT as well. These studies have yielded a wealth of information about the mechanism of folding of mLST8 and Raptor and mTORC assembly. The structures will also reveal sites of mLST8-CCT and Raptor-CCT interaction that could be targeted by small molecules to enhance or disrupt folding of these proteins and mTOR complex assembly. Chapter 4 described these studies in detail.

CHAPTER 4: MTORC FOLDING AND ASSEMBLY

Summary

The mTOR kinase performs an essential function in the signaling processes that control cell metabolism, growth and proliferation. mTOR functions in two structurally and functionally unique complexes, mTORC1 and mTORC2. In this study, we investigated the mechanism of assembly of these mTOR complexes and found that the cytosolic chaperonin CCT contributes to mTOR signaling by assisting in the folding of mLST8, a component of both mTORC1 and mTORC2, and also Raptor, a component of mTORC1. Both mLST8 and Raptor contain β-propeller domains that are common CCT folding substrates. The CCT co-chaperone PhLP1 also contributes to mLST8 folding, but not Raptor folding. On the contrary, PhLP1 plays a role in Raptor ubiquitination and degradation.

The structure of mLST8 bound to CCT was investigated by cryo-electron microscopy (cryo-EM) and chemical crosslinking coupled with mass spectrometry (XL-MS). The results show mLST8 bound in the bottom of the CCT folding cavity in a very different location than the G protein β subunit, another β-propeller protein and close structural homolog of mLST8. Thus, despite their structural similarities CCT accommodates similar β-propeller proteins by employing unique binding surfaces within the CCT folding cavity. These structural and functional studies

of mTOR complex assembly increase our understanding of the assembly mechanism and provide additional therapeutic targets to possibly treat diseases associated with mTOR malfunction.

Introduction

Mechanistic target of rapamycin (mTOR) is a central regulator of cell growth [95]. Sensing both intra- and extra-cellular stimuli such as energy levels, redox state, nutrient availability, growth factors and cellular stress through specific signaling pathways, mTOR responds and controls the fate of the cell by phosphorylating its downstream effectors [95, 183, 184]. mTOR is known to form structurally and functionally distinct protein complexes, mTORC1 and mTORC2, to achieve its cellular functions. mTORC1 consists of three principal components: mTOR, mammalian lethal with SEC13 protein 8 (mLST8), and regulatory associated protein of mTOR (Raptor), while mTORC2 consists of mTOR, mLST8, rapamycin-insensitive companion of mTOR (Rictor), and mammalian stress-activated protein kinase interacting protein 1 (mSIN1) [110-112]. While mTORC1 is sensitive to rapamycin, mTORC2 is not sensitive until prolonged dose of the drug [98]. Upstream and downstream effectors, binding partners, cell type-specific functions, and localization are distinct between these complexes.

Regardless of cell type, healthy or tumorous, all proteins have to be properly synthesized to support growth of the cell [185]. Proper synthesis requires not only translation by the ribosome but also post-translational processing such as protein stabilization, folding by chaperones, and assembly into a complex. Needless to say, the stability of mTORCs directly affects multiple cellular processes including cell growth and proliferation. Whether destined to mTORC1 or mTORC2, the mTOR kinase is folded by heatshock protein (HSP) 90 and the Tel2-Til1-Til2 and Rvb1/2-Tah1-Pih1 (TTT-R2TP) complex prior to functioning in the mTOR signaling [106, 156, 157]. However, the folding process of other mTORC components and the assembly into mTORC1/mTORC2 is not understood.

Clues about the folding of mLST8, an essential component of both mTORC1 and mTORC2, can be gleaned from its structural homology to guanine nucleotide binding protein β subunit (Gβ) [186]. Both mLST8 and Gβ share WD40 repeat sequences that fold into a 7-bladed β-propeller structure. Gβ is assisted in its folding by the cytosolic chaperonin containing tailless polypeptide 1 (CCT) and its co-chaperone, phosducin like-1 (PhLP1) [44]. CCT is a large protein chaperone complex that folds approximately 10 % of eukaryotic proteome. One interesting characteristic of CCT is that a number of its substrates have β-propeller structures [43, 46, 158-160]. In addition to mLST8, the mTORC1 subunit Raptor and the mTORC2 subunit Rictor also contain β-propeller domains [111, 128]. These observations suggest that CCT may be involved in the folding of multiple mTORC subunits. In fact, a genetic link between mTOR and CCT has been reported in a study investigating the physiological effects of individual CCT subunits in yeast [162]. In that study, when the CCTζ subunit was over-expressed, LST8 and TOR mutant phenotypes were suppressed, indicating that deficient mTORC could be rescued by increasing CCT activity. Furthermore, an mLST8-CCT interaction was detected in an autophagy interactome study by mass-spectrometry [163].

To assess the role of CCT and PhLP1 in mTOR signaling, we have measured the effects of loss of these chaperones from the cell using siRNA-based depletion and CRISPR-based gene deletion on mTOR complex assembly and signaling. We also purified CCT-bound folding intermediates of mLST8 and raptor and investigated their structure by a combination of cryo-EM and XL-MS. The results of this analysis reveal roles for CCT and PhLP1 in mTORC1 and mTORC2 assembly and provide insight into the mechanism by which they contribute to mLST8 folding.

Methods

Purification of the mLST8-CCT, PhLP1-mLST8-CCT, and Raptor-CCT complex

mLST8-CCT, PhLP1-mLST8-CCT, and Raptor-CCT complexes were purified from human embryonic kidney (HEK)-293T cells over-expressing PhLP1 and mLST8 or Raptor. The details of cell culturing and over-expression are described in Experimental Procedures section of Chapter 2. For the purification of mLST8-CCT, HEK-293T cells were co-transfected with a pcDNA3.1 vector containing human PhLP1 with a c-Myc-His_6 tag at the C-terminus and the same vector containing human mLST8 with a double Strep-Flag tag at the N-terminus and an HPC4 tag at the C-terminus. For Raptor over-expression, HEK-293T cells were transfected with a pDEST40 vector containing human Raptor with a HPC4-Strep-His_6 tag at the N-terminus. The cell lysate was prepared by the same methods described in Chapter 2.

In the purification of the mLST8-CCT and PhLP1-mLST8-CCT complexes, the cell lysate was first applied to a HisPur (Thermo Fisher Scientific) packed column equilibrated with cobalt equilibration buffer (20 mM HEPES pH 7.5, 20 mM NaCl) and circulated at 4 ^{o}C for one hour. The column was washed with five column volumes of cobalt wash buffer (20 mM HEPES pH 7.5, 20 mM NaCl, and 0.05 % CHAPS) and eluted with 2.5 column volumes of cobalt elution buffer (20 mM HEPES pH 7.5, 20 mM NaCl, 250 mM imidazole, and 0.05 % CHAPS). For the PhLP1-mLST8-CCT complex, the HisPur column eluate was loaded onto a Strep-Tactin column equilibrated with Strep equilibration buffer (see Chapter 2 for buffer contents), washed with three column volumes of Strep wash buffer, and eluted with five column volumes of Strep elution buffer. For the mLST8-CCT complex purification, after loading the Strep column it was washed with three column volumes of high salt wash buffer and one column volume of Strep wash buffer and eluted with five column volumes of Strep elution buffer. The purpose of the high salt wash buffer was to remove PhLP1 from mLST8-CCT complex by disrupting electrostatic interactions with high ionic strength.

An HPC4 column (Roche) was used for the purification of Raptor-CCT complex. The lysate from cells over-expressing HPC4-tagged Raptor was loaded on to the HPC4 resin, and the column was washed twice with two column volumes of high salt wash buffer and once with two column-volumes of Strep wash buffer. Raptor was eluted in five elution steps, each with one column volume of HPC4 elution buffer according to the manufacturer's protocol.

The protein complexes were concentrated to ~ 2 mg/mL by centrifugation with a 30 kDa molecular weight cutoff filter (Millipore). Purity of the samples was confirmed by SDS-PAGE and immunoblotting. The concentrated samples were flash frozen with liquid nitrogen and stored at -80 ºC until use. Purified mLST8-CCT and PhLP1-mLST8-CCT complexes were further analyzed by either cryo-EM or XL-MS.

Cryo-EM

Purified mLST8-CCT and PhLP1-mLST8-CCT complexes were applied to glow discharged Quantifoil 1.2-μm holey carbon grids, blotted, and fast-frozen in liquid ethane. Low-dose images ($<10\ e^-/\text{Å}^2$) of the complexes were taken on a Titan Krios 300 kV electron microscope at 300 kV. Image classification was done with reference-free methods [187], and the selected averages were obtained to generate a reference volume using common lines [79], which was subsequently applied for the 3D reconstruction procedure [188]. Chimera was used to visualize and dock the atomic structures [74].

Transfection, immunoprecipitation, and immunoblotting

cDNAs for human mTOR, mLST8, and Raptor, mSIN1, and Rictor were purchased through Addgene and inserted into mammalian expression vectors such as pcDNA3.1 and pDEST40 by conventional cloning methods with epitope tags. DNA constructs were delivered into HEK-293T cells or HEPG2 cells growing in 6-well plates using either Lipofectamine 2000 (Thermo Fisher Scientific) or Lipofectamine 3000 (Thermo Fisher Scientific) as a transfection reagent following the manufacturer's protocol. Cells were fed with fresh media after 4 hours and were harvested 48-72 hours post-transfection. Cells were washed with PBS and lysed in lysis buffer (HEPES lysis buffer for mTORC1, PBS lysis buffer for mTORC2). Cleared lysates were immunoprecipitated with α-CCTε (AbD Serotec MCA2178), α-His$_6$ tag (Thermo Fisher Scientific MA1-21315), α-HA (Roche 11867423001), α-Flag (Sigma F3165), or α-c-Myc (Invitrogen 13-2500) antibody followed by addition of protein A/G agarose (Santa Cruz). Both the antibody and agarose incubations were conducted for 30-60 minutes at 4 ^{o}C. For the double IP experiment in **Figure 4.2 D**, the agarose was incubated with 100 µL of ProTEV protease solution for 1 hour at 25 ^{o}C between the two immunoprecipitation steps. The agarose was washed with lysis buffer and resuspended in SDS-PAGE sample loading buffer. Proteins were separated either by 5, 7, 8, 10, or 4-15 % acrylamide gradient SDS gels, transferred to nitrocellulose and incubated with antibodies including: α-CCTε, α-HA, α-Flag, α-c-Myc, α-CCTζ (Santa Cruz SC-13897), α-PhLP1 N-terminus [189], α-GFP (Abcam AB6556), or α-GAPDH (AbD Serotec MCA4740). Blots were washed and incubated with secondary antibodies including: LI-COR α-mouse (926-32210), α-rat (926-32219), α-goat (926-32214), and α-rabbit (926-32211). Blots were imaged using a LI-COR Odyssey infrared scanner, and proteins were quantified with the LI-COR software.

siRNA knockdown

siRNAs targeting PhLP1, CCT, or non-targeting negative control #1 were purchased from Ambion. The siRNAs were introduced into HEK-293T cells, which were at 30-45 % confluency, with Lipofectamine 2000 according to the manufacture's protocol. Cells were fed after three hours and transfected after 24 hours with plasmids containing mTORC components using Lipofectamine 2000 followed by feeding with fresh media three hours after addition of cDNAs. 48 hours after addition of the siRNAs, the media was replaced with fresh media, and cells were harvested for immunoprecipitation and immunoblotting 96 hours after introduction of the siRNAs.

CRISPR knockdown

A plasmid vector containing a puromycin resistance gene, the Cas9 gene, and an sgRNA was constructed. The sgRNA targeted a sequence near the 5'-end of the CCTε gene coding region, allow Cas9 to make a double strand break on the gene and inhibit gene expression by introducing insertion/deletion mutations through non-homologous end joining repair mechanisms. The same vector without the sgRNA segment was also prepared to be used as a negative control. These vectors were transfected into HEK-293T cells at 25-40 % confluency with Lipofectamine 2000. After three hours, the cells were fed and after 48 hours they were transfected with vectors containing mTORC components using Lipofectamine 2000. Three hours later the cells were fed with media containing puromycin. The concentration of the puromycin in the culture was kept at 10 μg/mL until harvest. Cells were harvested for immunoprecipitation and immunoblotting 120 hours after addition of the sgRNA vector.

Ubiquitin assay

After treating HEK-293T cells with siRNA targeting PhLP1, the cells were co-transfected with a pcDNA3 vector containing human ubiquitin with an N-terminal HA tag (Addgene) and a pDEST40 vector containing human Raptor with an N-terminal Strep tag using Lipofectamine 2000. Cells were fed with fresh media four hours post-transfection and treated with 10 μM of MG-132 (Ubiquitin-Proteasome Biotechnologies) two to four hours prior to harvest. At 48 hours post-transfection, cell lysates were prepared and immunoprecipitated with an α-HA tag antibody and immunoblotted as described above.

Insulin signaling

HEPG2 cells were treated with 40 nM of siRNA targeting CCTα/ε, PhLP1, mLST8 or Raptor using Lipofectamine 3000 following the manufacturer's protocol to knockdown the corresponding endogenous proteins. Overnight serum-starvation followed three days after the siRNA transfection. Subsequently, the cells were treated with 1 μM insulin for 30 minutes to activate mTORC1 or 50 nM insulin for 10 minutes to activate mTORC2. The effects on mTORC1 and mTORC2 signaling were analyzed by SDS-PAGE and immunoblotting the cell lysates for phosphorylation at IRS1 S636/639 and AKT S473, respectively. Total CCT, PhLP1, mLST8, Raptor, AKT and IRS1 were also immunoblotted to assess the respective knockdown and expression level.

Results

mLST8 forms a ternary complex with CCT and PhLP1

We began to test the possibility that CCT and PhLP1 contribute to the folding of mLST8, we assessed the interaction of mLST8 with CCT by co-immunoprecipitation. A Flag-tagged construct of mLST8 was transfected into HEK-293T cells and cell lysates were immunoprecipitated with an antibody to the Flag tag. Immunoblots for the CCTε subunit showed a strong band in the Flag-mLST8 sample that was not seen in the empty vector controls, indicating a robust interaction between mLST8 and CCT (**Figure 4.1 A**). Similar immunoprecipitations were performed with cells over-expressing Flag-tagged mLST8 and His_6-tagged PhLP1. Immunoblots of PhLP1 immunoprecipitates showed a prominent mLST8 band while the empty vector control with no PhLP1 over-expression did not, indicating an interaction between mLST8 and PhLP1 (**Figure 4.1 B**).

The observed binding of mLST8 to both CCT and PhLP1 and the known interaction of PhLP1 with CCT suggested that mLST8 might form a ternary complex with CCT and PhLP1. To test this notion, we measured the effect of siRNA-mediated depletion of CCT on the mLST8-PhLP1 interaction. A 60 % decrease in CCT resulted in a similar 45 % decrease in the co-immunoprecipitation of mLST8 with c-Myc-tagged PhLP1, suggesting that mLST8, PhLP1 and CCT were all part of the same complex (**Figure 4.1 C**). To confirm this finding, we performed a double immunoprecipitation from cells expressing Flag-mLST8 and PhLP1 with a C-terminal TEV protease site followed by a c-Myc tag. We first immunoprecipitated PhLP1 with a c-Myc antibody and found PhLP1, mLST8 and CCT in the immunoprecipitate as expected (**Figure 4.1 D**). We then treated the immunoprecipitate with TEV protease to release PhLP1 containing complexes from the protein A/G beads and performed a second immunoprecipitation with an antibody to CCT. All three proteins were again found in this second immunoprecipitate while none were found in the empty vector control. The only way that mLST8 could be found in both immunoprecipitates was if it was simultaneously bound to both PhLP1 and CCT in the same complex, thus these experiments demonstrate that mLST8 forms a ternary complex with both CCT and PhLP1.

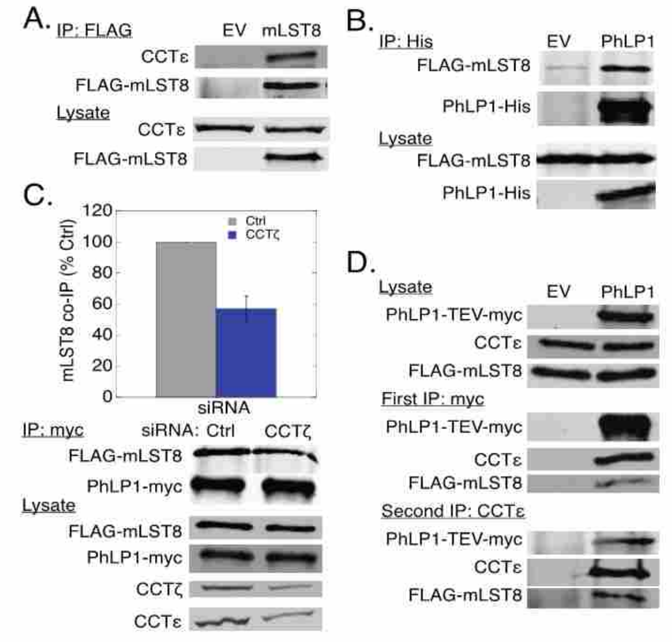

Figure 4.1 PhLP1 and mLST8 form a ternary complex with CCT A) Interaction of mLST8 with CCT. HEK-293T cells were transfected with Flag-mLST8 or empty vector (EV). Lysates were immunoprecipitated with α-Flag antibody and immunoblotted for CCT□ and Flag-mLST8. B) Interaction of mLST8 with PhLP1. Cells were co-transfected with Flag-mLST8 and PhLP1-c-Myc-His or empty vector. Lysates were immunoprecipitated with α-His_6 tag antibody and immunoblotted for Flag-mLST8 and PhLP-His. C) CCT depletion inhibited mLST8 interaction with PhLP1. Cells were treated with CCTζ or control siRNA, co-transfected with Flag-mLST8 and PhLP1-c-Myc-His and immunoprecipitated with a Myc-antibody. Immunoprecipitates and cell lysates were blotted as indicated. D) Double immunoprecipitation revealed PhLP1-mLST8-CCT ternary complex. Cells were co-transfected with Flag-mLST8 and PhLP1-TEV-c-Myc or empty vector and immunoprecipitated with a Myc antibody. Complexes were released from beads by TEV cleavage and immunoprecipitated again with a CCTε antibody and immunoblotted as indicated.

Raptor interacts with CCT and PhLP1

Raptor is a large multi-subunit protein with a β-propeller domain at its C-terminus [111], which raises the possibility that Raptor may also bind CCT via its β-propeller domain. To test this possibility, we transfected HEK-293T cells with hemagglutinin (HA)-tagged Raptor and measured both the co-immunoprecipitation of CCT with Raptor and Raptor with CCT. CCT was found in the Raptor immunoprecipitate and Raptor was found in the CCT precipitate, confirming a CCT-Raptor interaction (**Figure 4.2 A**). To determine which part of Raptor is responsible for CCT binding, we performed similar immunoprecipitation experiments with HA tagged truncated Raptor proteins, using a C-terminal construct (1020-1335) containing the β-propeller domain and an N-terminal construct containing the other domains (1-1019). The C-terminal Raptor β-propeller interacted strongly with CCT, while the N-terminal region failed to bind to CCT (**Figure 4.2 B** and **C**), indicating that CCT binds to C-terminal β-propeller of Raptor as predicted.

The Raptor-CCT interaction was also confirmed by partial purification of the complex. Raptor with N-terminal HPC4, His and Strep purification tags was transfected into HEK-293T cells and was purified from cell lysates using an HPC4 affinity column. The purified Raptor contained some CCT, but the amount was substochiometric based on the Coomassie gel staining (**Figure 4.2 D**). This finding suggests that the Raptor-CCT interaction may be transient with only a fraction of the Raptor bound to CCT in the cell or Raptor may dissociate from CCT during the purification process.

The binding of Raptor to CCT raised the possibility that Raptor might form a stable ternary complex with CCT and PhLP1 similar to mLST8. To test this notion, lysates from HEK-293T cells co-expressing HPC4-His-Strep-Raptor and PhLP1-c-Myc-His were subjected to tandem affinity purification using cobalt and strep columns. However, neither PhLP1 nor CCT was recovered in the final elution from the Strep column although they were both eluted from the cobalt column (data not shown). Thus, Raptor does not appear to form a ternary complex with PhLP1 and CCT.

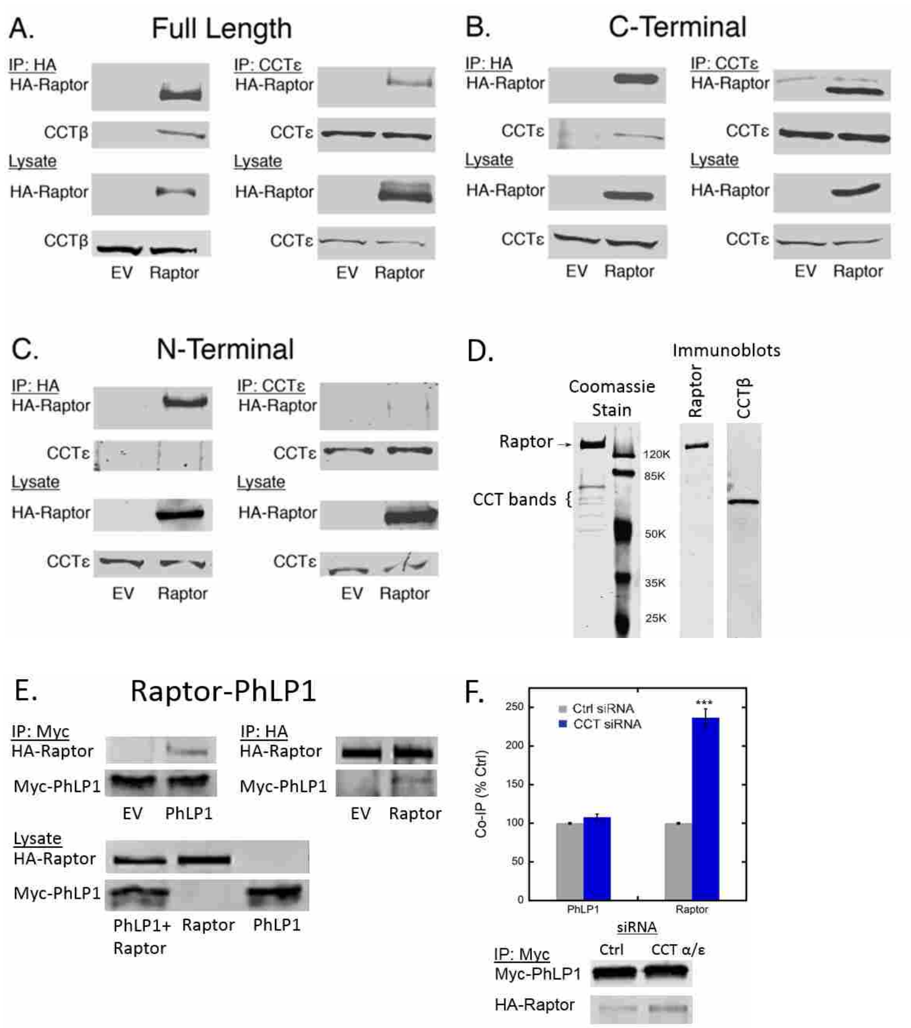

Figure 4.2 Raptor independently binds CCT and PhLP1 A) Full-length Raptor binds to CCT. HEK-293T cells were transfected with HA-Raptor or empty vector. Lysates were immunoprecipitated with an HA antibody or a CCTε antibody and immunoblotted blotted as indicated. B) Binding of the C-terminal β-propeller domain of Raptor to CCT. Immunoprecipitation experiments were performed with cells over-expressing the C-terminal □-propeller domain of Raptor (residues 1020-1335). C) No binding of the N-terminal region of Raptor to CCT. Immunoprecipitation experiments were performed with cells over-expressing the N-terminal region of Raptor (residues 1-1019). D) Purified Raptor-CCT complex. The complex was purified using an HPC4 affinity column, concentrated, run on SDS-PAGE, stained with Coomassie and immunoblotted. E) Raptor interacts with PhLP1. Immunoprecipitation experiments were performed with cells with over-expressing PhLP1 and Raptor. F) CCT depletion increases PhLP1 binding to Raptor. The PhLP1-Raptor co-immunoprecipitation experiment was performed with cells treated with siRNAs to CCTα and CCTε. The graph shows the protein in the immunoprecipitate from CCT siRNA treated cells compared to control cells. Bars represent the average ± standard error from three experiments. *** $p < 0.001$.

Despite the failure to purify a PhLP1-Raptor-CCT ternary complex, we found that PhLP1 bound to Raptor independently of CCT. Over-expressed PhLP1 and Raptor were found to coimmunoprecipitate with each other (**Figure 4.2 E**). When we siRNA-depleted CCT from cells, the amount of Raptor co-immunoprecipitating with PhLP1 increased by more than 2-fold (**Figure 4.2 F**). This finding shows that PhLP1 interacts with Raptor independently of CCT and that PhLP1 and CCT compete for Raptor binding. Thus, PhLP1 appears to have a very different role with Raptor as it does with mLST8.

CCT is required for assembly of mTORC1 and mTORC2

The binding of both mLST8 and Raptor to CCT point to a role for CCT in the folding and assembly of these subunits into mTOR complexes. We investigated this possibility by using CRISPR technology to delete CCT from cells and measure the effect on formation of mTORC1 and mTORC2. Cells were transfected with a vector containing a puromycin resistance gene, the Cas9 gene, and an sgRNA targeting CCTε. After 48 hours, cells were also transfected with mTORC1 components (V5-mLST8, HA-Raptor, and c-Myc-mTOR) or mTORC2 components (V5-mLST8, HA-mSIN1, c-Myc-Rictor, and Flag-mTOR). Cells harboring the Cas9 and sgRNA vector were selected by treating with puromycin over a 72-hour period. We chose this short term CRISPR approach because clonal selection of cells with CCTε gene deletions are not viable during long term selection because CCT is essential for cell survival. This method was able to reduce CCT expression by 70 % within the cell population that survived the puromycin selection. After selection, cell lysates were immunoblotted for mTORC components to determine their expression levels and mTOR was immunoprecipitated and immunoblotted for mTORC components to determine the degree to which mTOR complexes were assembled. With mTORC1, blotting the cell lysates showed a significant reduction of expression of mLST8 (50 %) and Raptor (50 %) and a moderate decrease in mTOR expression (25 %) compared to control cells with no sgRNA (**Figure 4.3 A**). The expression levels of exogenously transfected

GFP or endogenous GAPDH were unchanged, indicating that the CRISPR deletion effects were specific. Compared to the cell lysates, the immunoprecipitates showed similar decreases in mTOR (30 %), mLST8 (50 %) and a somewhat lower decrease in Raptor (30 %) (**Figure 4.3 B**). These results show that CRISPR-mediated depletion of CCT reduces the expression and assembly of components of mTORC1.

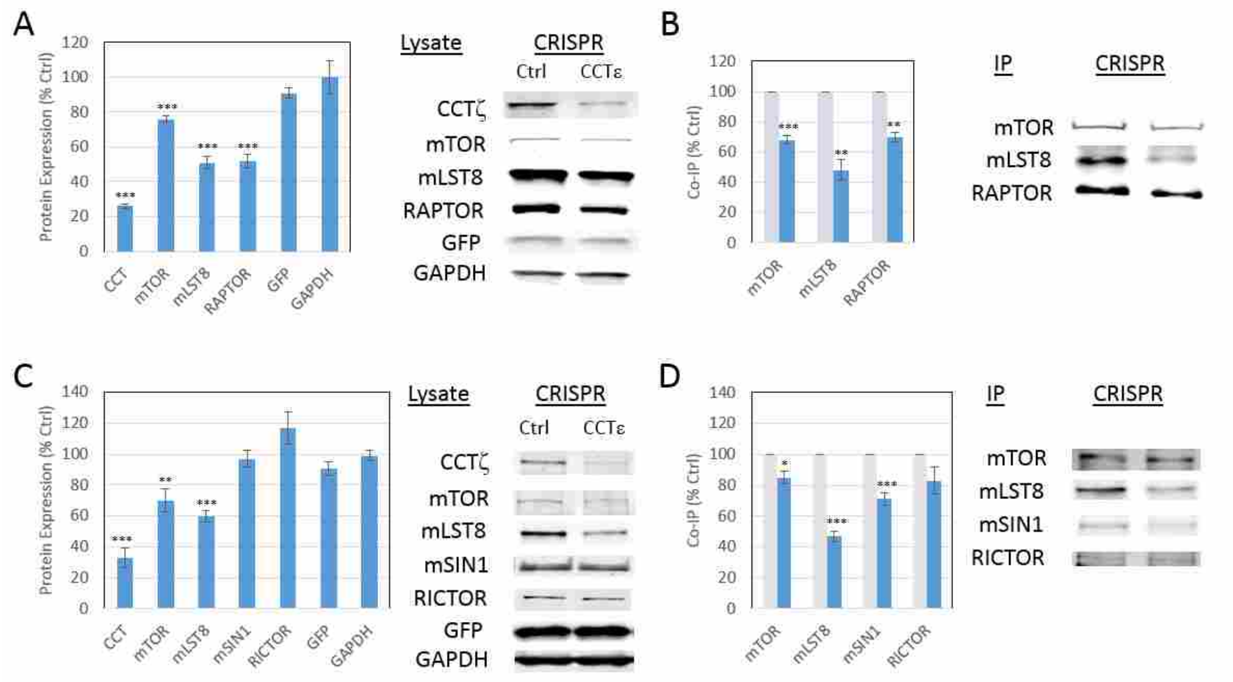

Figure 4.3 CCT contributes to mTORC formation A) Effects of CRISPR-mediated CCT depletion on mTORC1 subunit expression. HEK-293T cells were treated with CCTε sgRNA along with Cas9 and transfected with c-Myc-mTOR, V5-mLST8, HA-Raptor and GFP. mTORC1 components in the cell lysates were immunoblotted as indicated. The graph shows the relative expression level compared to control cells with non-targeting sgRNAs. B) Effects of CRISPR-mediated CCT depletion on mTORC1 assembly. c-Myc-mTOR was immunoprecipitated from the lysates and immunoblotted for c-Myc-mTOR, V5-mLST8 and HA-Raptor to assess the level mTORC1 assembly. The graph shows the relative co-immunoprecipitation of mTORC1 subunits compared to the non-targeting sgRNA control. C) Effects of CRISPR-mediated CCT depletion on mTORC1 subunit expression. Cells were treated with CCTε sgRNA along with Cas9 and transfected with Flag-mTOR, V5-mLST8 and HA-mSIN1, c-Myc-Rictor, and GFP. mTORC2 components in the cell lysates were immunoblotted as indicated. The graph shows the relative expression level compared to control cells with non-targeting sgRNAs. D) Effects of CCT depletion on mTORC2 assembly. Flag-mTOR was immunoprecipitated from the lysates and immunoblotted for Flag-mTOR, V5-mLST8, HA-mSIN1, and c-Myc-Rictor to assess the level mTORC2 assembly. The graph showed the co-immunoprecipitated mTORC2 components with the CRISPR knockdown by CCT sgRNA compared to the non-targeting sgRNA control. Bars in the graphs represent the average ± standard error from at least three biological replicates. * indicates $p < 0.05$. ** indicates $p < 0.01$. *** indicates $p < 0.001$.

With mTORC2, CCT depletion resulted in decreases in mLST8 (40 %) and mTOR (30 %) expression, but there was no change in mSIN1 and Rictor expression compared to control cells with no sgRNA (**Figure 4.3 C**). Expression of exogenous GFP and endogenous GAPDH was also unchanged, again indicating that the CRISPR deletion effects were specific. The immunoprecipitations showed small reductions in mTOR (20 %), mSIN1 (30 %) and Rictor (20 %) with a larger reduction in mLST8 (50 %) (**Figure 4.3 D**). These results suggest that the ability of mLST8 to assemble into the mTORC2 complex depends on CCT. Collectively, these results indicate that mLST8 and Raptor depend on CCT for their folding and association with mTOR, but that mSIN1 and Rictor do not.

PhLP1 contributes to mTORC1 assembly

Since we observed interactions of PhLP1with mLST8 and Raptor, we assessed the effect of PhLP1 depletion to know whether PhLP1 is contributing to mTORC signaling by supporting expression and assembly of the components. HEK-293T cells were treated with an siRNA targeting PhLP1 and were transfected with Flag-mLST8, HA-Raptor, and c-Myc-mTOR. Cell lysates were immunoblotted for mTORC1 components to determine their expression levels and mTOR was immunoprecipitated and immunoblotted for mTORC1 components to determine the degree to which mTOR complexes were assembled. The siRNA reduced PhLP1 expression by 70 % compared to cells treated with a non-targeting siRNA. mTOR expression was reduced by 50 % while mLST8 expression was reduced by 35 % compared to controls. Raptor expression was unchanged as were the exogenous GFP and endogenous GAPDH controls (**Figure 4.4 A**). Similarly, mTOR immunoprecipitation and mLST8 co-immunoprecipitation were also reduced by 40 %, while Raptor co-immunoprecipitation was unchanged (**Figure 4.4 B**). These findings imply that PhLP1 contributes to mLST8 folding, but not Raptor folding.

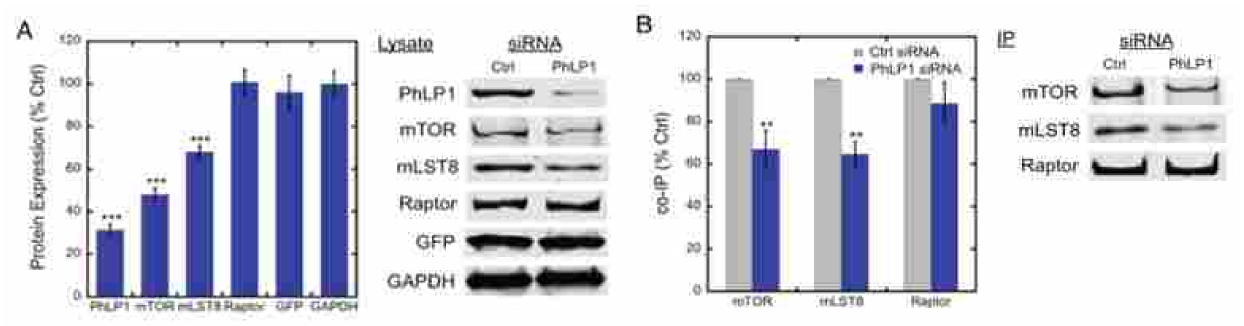

Figure 4.4 PhLP1 contributes to mTORC1 formation A) Effects of PhLP1 depletion on mTORC1 subunit expression. HEK-293T cells were treated with PhLP1 or a non-targeting control siRNA and transfected with c-Myc-mTOR, Flag-mLST8, HA-Raptor and GFP. Lysates were immunoblotted as indicated. The graph shows the relative expression level compared to control cells with non-targeting siRNAs. B) Effects of PhLP1 depletion on mTORC1 assembly. c-Myc-mTOR was immunoprecipitated from the lysates and immunoblotted for c-Myc-mTOR, Flag-mLST8 and HA-Raptor to assess the level mTORC1 assembly. The graph shows the relative co-immunoprecipitation of mTORC1 subunits compared to the non-targeting siRNA control. Bars represent the average ± standard error from 7-9 experiments. ** indicates $p < 0.01$. *** indicates $p < 0.001$.

Contributions of CCT and PhLP1 on mTOR signaling

The contributions of CCT and PhLP1 to mTOR complex assembly should carry over into mTOR signaling as well. To test this possibility, we measured the effects of CCT and PhLP1 depletion on insulin-induced mTOR activity in HEPG2 cells, a hepatocyte-derived cell line that responds robustly to insulin. We used siRNA to deplete these cells of CCT and PhLP1, and for comparison, we also siRNA-depleted mLST8 and Raptor. To assess mTORC1 signaling, we exposed siRNA-treated and serum-starved cells with 1 µM insulin for 30 min and measured phosphorylation of the mTORC1 specific substrate IRS1 S636/639 by immunoblotting with a phospho-specific antibody to this site. To assess mTORC2 signaling, we exposed siRNA-treated cells to 50 nM insulin for 10 min and measured phosphorylation of the mTORC2 specific substrate AKT S473 with a phospho-specific antibody (**Figure 4.5**).

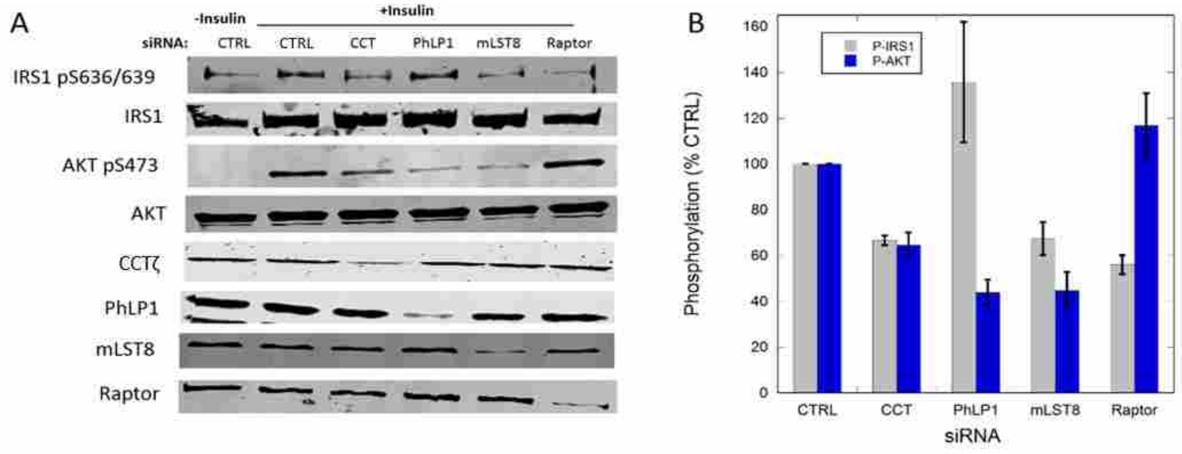

Figure 4.5 Effects of depletion of CCT and PhLP1 on mTORC1 and mTORC2 signaling HEPG2 cells were treated with siRNAs targeting CCTα/ε, PhLP1, mLST8 or Raptor. The cells were serum-starved overnight and treated with 1 μM insulin for 30 minutes to activate mTORC1 or 50 nM insulin for 10 minutes to activate mTORC2. The effects on mTORC1 and mTORC2 signaling were determined by immunoblotting the cell lysates for phosphorylation at IRS1 S636/639 and AKT S473, respectively. A) The immunoblot images of the lysates. B) Quantification of the phospho-IRS and phospho-AKT blots. Bars represent average ± standard error from 3-7 experiments.

CCT depletion caused a 40 % decrease both IRS1 and AKT phosphorylation at these sites, while PhLP1 phosphorylation resulted in small increase in IRS1 phosphorylation and a 60 % decrease in AKT phosphorylation (**Figure 4.5 A** and **B**). In comparison, mLST8 depletion caused 40 % decrease in IRS1 phosphorylation and a 60 % decrease in AKT phosphorylation, while Raptor depletion caused a 40 % decrease in IRS1 phosphorylation and no change in AKT phosphorylation. These effects of mLST8 and Raptor depletion were both consistent with mLST8 being found in both mTORC1 and mTORC2 while Raptors is only found in mTORC1. The decrease in both IRS1 and AKT phosphorylation upon CCT depletion is consistent with a role for CCT in mLST8 and Raptor folding, and the decrease in AKT phosphorylation upon PhLP1 depletion is also consistent with a role for PhLP1 in mLST8 folding. However, the increase in IRS1 phosphorylation with PhLP1 depletion is not. It is possible that there are opposing effects of loss of PhLP1 on mTORC1 signaling, possibly through PhLP1 binding to Raptor, that negate the positive role of PhLP1 on mLST8 folding.

PhLP1 contributes to Raptor degradation

To further investigate the role of PhLP1 in Raptor function, we treated cells with PhLP1 siRNA and over-expressed Raptor. Surprisingly, the expression of Raptor tripled when PhLP1 was depleted **(Figure 4.6 A)**. This result suggests that PhLP1 is somehow destabilizing Raptor rather that contributing to its folding. We tested whether the ubiquitin-proteasome system was involved in this process by measuring the effects of PhLP1 depletion on Raptor ubiquitination. PhLP1-depleted cells were co-transfected with Raptor and HA-tagged ubiquitin, and the cells were treated with MG-132 to inhibit proteasome activity 2-4 hours before harvest. The HA-ubiquitin was immunoprecipitated and the samples were immunoblotted for HA. The blots showed smear-like bands of Raptor indicating that Raptor was poly-ubiquitinated. The poly-ubiquitinated bands were decreased in the PhLP1 depleted samples (**Figure 4.6 B**).

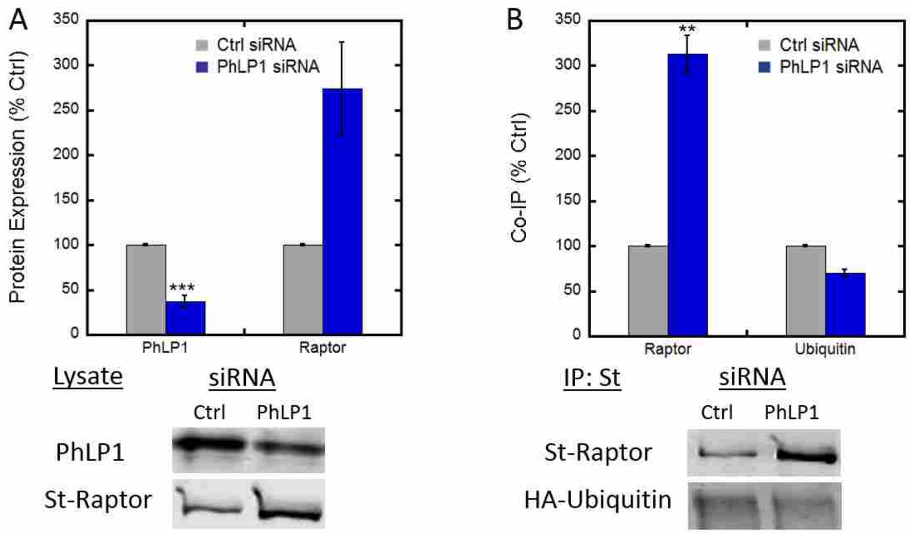

Figure 4.6 PhLP1 facilitates Raptor degradation A) Effects of PhLP1 knockdown on Raptor expression and ubiquitination. HEK-293T cells were treated with PhLP1 siRNA or a non-targeting control siRNA, and cell lysates were immunoblotted as shown. B) PhLP1 contributes to Raptor ubiquitination. HEK-293T cells were treated with PhLP1 siRNA or a non-targeting control siRNA, followed by co-transfection with Strep-Raptor and HA-ubiquitin. The cells were treated with 10 µM of the proteasome inhibitor MG-132 2-4 hours prior to harvest. Raptor was immunoprecipitated from the lysates and immunoblotted for HA-ubiquitin. Bars represent the average ± standard error from 5-6 experiments. ** indicates $p < 0.02$. *** indicates $p < 0.001$.

Though the end point difference looked moderate (30 %), when the 3-fold increase in Raptor expression upon PhLP1 depletion was taken into consideration, there was a 75 % decrease in the ubiquitinated Raptor to total Raptor ratio when PhLP1 was depleted. These results suggest that PhLP1 mediates Raptor degradation through ubiquitination and proteasomal degradation.

Purification of mLST8-CCT and PhLP1-mLST8-CCT for structural analysis

The data from **Figure 4.1** show that mLST8 binds CCT and forms a ternary complex with CCT and PhLP1. This observation let us to attempt to purify the mLST8-CCT and PhLP1-mLST8-CCT complexes. We over-expressed affinity-tagged versions of mLST8 (Strep-Flag-mLST8) and PhLP1 (PhLP1-c-Myc-His) in HEK-293T cells and purified complexes containing PhLP1 using a cobalt column for the His_6 tag and complexes containing mLST8 on a StrepTactin column for the Strep peptide tag. Washing the Strep column with low salt retained PhLP1 and allowed purification of the PhLP1-mLST8-CCT complex, while washing with high salt removed PhLP1 and allowed purification of the mLST8-CCT complex. The purified complexes were analyzed by SDS-PAGE and immunoblotting. The gel image showed the protein sample was highly purified (>90 %) and the immunoblots confirmed the presence of PhLP1, mLST8 and CCT. (**Figure 4.7 A** and **B**).

Cryo-EM analysis of mLST8-CCT and PhLP1-mLST8-CCT

The mLST8-CCT and PhLP1-mLST8-CCT complexes were sent to the laboratory of Jose Valpuesta at the Centro Nacional de Biotecnologia in Madrid, Spain where their structures were determined by cryo-EM. EM images revealed homogeneous particles of mLST8-CCT and PhLP1-mLST8-CCT. Class average images of the mLST8-CCT complex showed a mass within the CCT ring that could be attributed to mLST8 and similar images of the PhLP1-mLST8-CCT complex showed a mass spanning the top of the ring that could be attributed to PhLP1 (**Figure 4.8 A** and **B**).

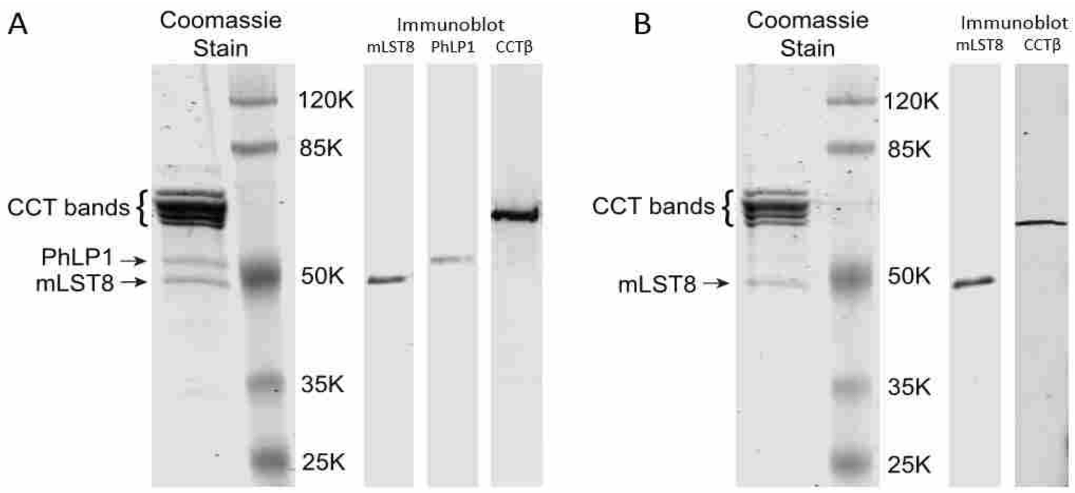

Figure 4.7 Purification of the PhLP1-mLST8-CCT and mLST8-CCT complexes A) PhLP1-mLST8-CCT, B) mLST8-CCT. The complexes were purified by cobalt-Strep tandem affinity purification. The concentrated protein complexes were run on SDS-PAGE, stained with Coomassie blue and immunoblotted as indicated. The Coomassie-stained gels show the purity of the complexes and the immunoblots identify the mLST8, PhLP1 and CCTβ bands.

The 2D cryo-EM images suggested that the purified mLST8-CCT and PhLP1-mLST8-CCT complexes were sufficiently homogeneous for cryo-EM analysis. Samples were applied to holey carbon grids, vitrified in liquid ethane and imaged on a Titan Krios 300 kV electron microscope. Interestingly, the PhLP1-mLST8-CCT sample yielded the most homogenous population of mLST8-CCT particles in which PhLP1 had dissociated. Approximately 3,000 homogeneous particles from this preparation were classified and reconstructed to generate an initial model of the mLST8-CCT complex (**Figure 4.8 C**). The reconstruction revealed the typical double-ring structure of CCT in an open conformation with an additional mass attributable to mLST8 sitting on side of the CCT folding cavity near the bottom. The Valpuesta lab is currently collecting additional images to obtain a higher resolution reconstruction to reveal the atomic details of the mLST8-CCT complex.

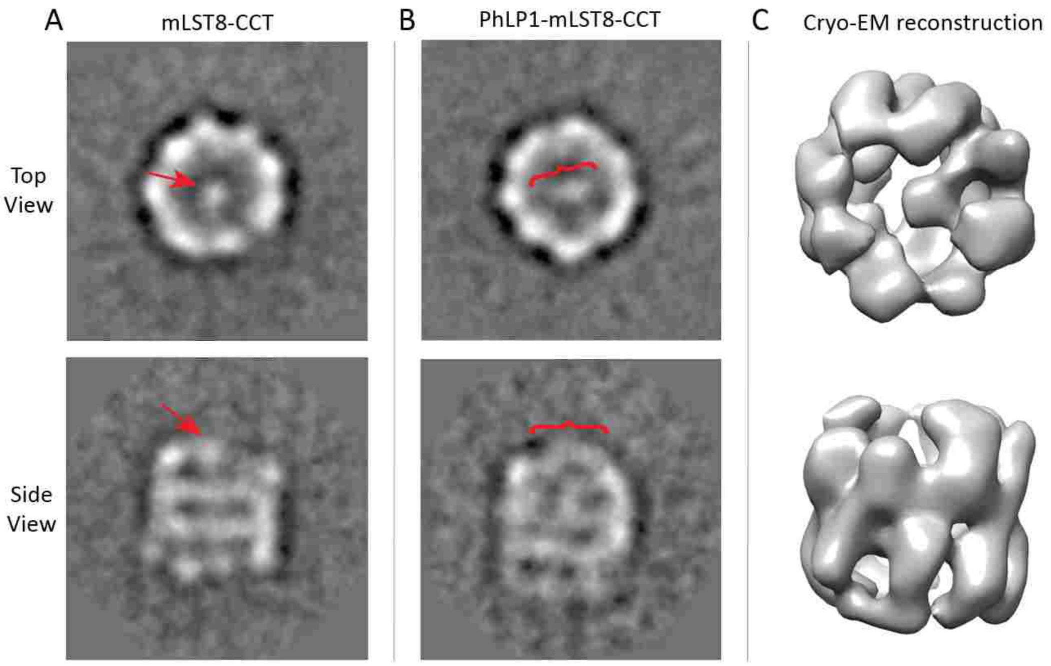

Figure 4.8 Cryo-EM analysis of the mLST8-CCT and PhLP1-mLST8-CCT complexes A) Images of cryo-EM class-averages of the mLST8-CCT complex. Top and side view images show a mass inside the CCT cavity attributable to mLST8 (red arrows). B) Images of cryo-EM class-averages of the PhLP1-mLST8-CCT. Top and side views of this complex show a mass attributable to PhLP1 spanning the top of CCT folding cavity (red brackets). C) Cryo-EM reconstruction of the mLST8-CCT complex. Top and side view images reveal that a mass of mLST8 is located in the deep inside of the CCT cavity.

XL-MS analysis of mLST8-CCT

We applied XL-MS to the mLST8-CCT complex to obtain crosslink distance constraints to orient mLST8 within the cryo-EM density. Purified mLST8-CCT complex was crosslinked with disuccinimidyl suberate (DSS), crosslinks were identified by mass spectrometry, and the structures were modeled according to the crosslink information. XL-MS of mLST8-CCT provided seven intra-protein crosslinks of mLST8 and three inter-protein crosslinks between mLST8 and CCT (**Figure 4.9 C** and **D**). We mapped the intra-protein crosslinks onto the 3.5 Å structure of mLST8 bound to the mTOR kinase domain [110] and found that four out of seven intra-protein crosslinks were within the 30 Å cutoff limit, while three crosslinks had slightly longer distances (**Figure 4.9 C**). From this result, it appears that mLST8 has achieved a near native conformation in the mLST8-CCT complex.

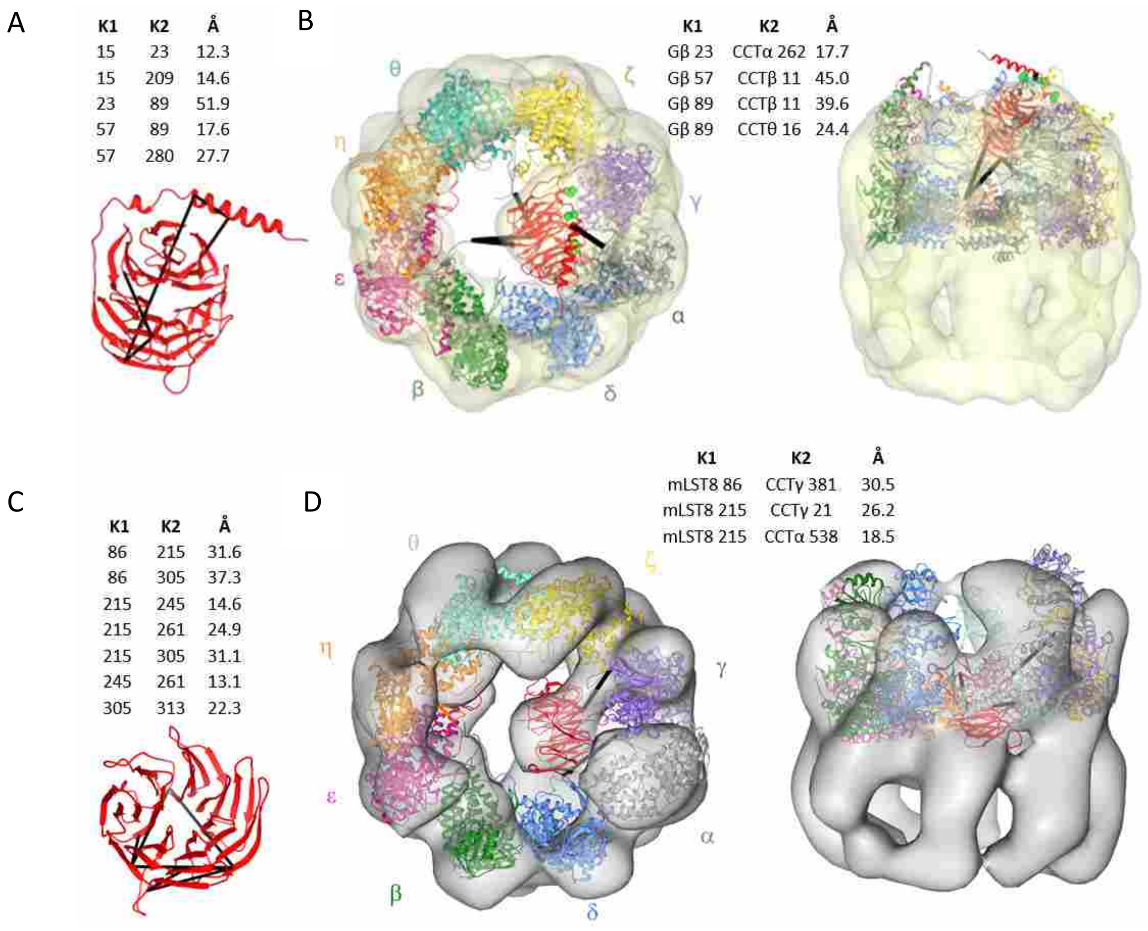

A

K1	K2	Å
15	23	12.3
15	209	14.6
23	89	51.9
57	89	17.6
57	280	27.7

B

K1	K2	Å
Gβ 23	CCTα 262	17.7
Gβ 57	CCTβ 11	45.0
Gβ 89	CCTβ 11	39.6
Gβ 89	CCTθ 16	24.4

C

K1	K2	Å
86	215	31.6
86	305	37.3
215	245	14.6
215	261	24.9
215	305	31.1
245	261	13.1
305	313	22.3

D

K1	K2	Å
mLST8 86	CCTγ 381	30.5
mLST8 215	CCTγ 21	26.2
mLST8 215	CCTα 538	18.5

Figure 4.9 Structural comparison of Gβ-CCT and mLST8-CCT A) Intra-molecular Gβ crosslinks, B) inter-protein crosslinks between Gβ and CCT and the atomic structural model of the complex. Gβ-CCT complex purified from insect cells was analyzed with XL-MS using DSS crosslinker. The atomic structures of Gβ and CCT were docked together into the cryo-EM volume guided by the crosslink information obtained by XL-MS analysis. Gβ interacts with apical domain of CCTα (gray) and CCTγ (purple). C) Intra-molecular mLST8 crosslinks, D) mLST8-CCT atomic structure built with the inter-protein crosslink information obtained by XL-MS. mLST8-CCT complex purified from HEK-293T cells were crosslinked by DSS crosslinker and analyzed by mass spectrometry. CCT and mLST8 structure were docked into a preliminary cryo-EM electron density map of mLST8-CCT. mLST8 was positioned deep in the CCT cavity near CCTα (gray) and CCTγ (purple). PDB 2XSM (B) [190]/4B2T (D) [191], 2TRC [192], and 4JSV [110] were used for CCT, Gβ, and mLST8 structures, respectively. Crosslinks were depicted by black lines. Crosslinked lysines (K1 and K2) and each distance (Å) are listed in the table.

Next, we applied the three inter-protein crosslinks to orient mLST8 on CCT. The first inter-protein crosslink was formed between K86 of mLST8 and K381 of CCTγ, and the second and third were formed between K215 of mLST8 and K21 of CCTγ and K538 of CCTα (**Figure 4.9 D**). Minimizing the crosslink distances placed mLST8 in the folding cavity near the bottom one face of the β-propeller in contact with the CCTα and CCTγ subunits. We docked the modeled atomic structures of the mLST8-CCT complex into the cryo-EM density map of mLST8-CCT (**Figure 4.9 D**). The mLST8 and CCT structures were easily superimposed within the cryo-EM volume with all of the inter-protein crosslinks within the 30 Å cutoff.

Discussion

Role of CCT in mLST8 and Raptor folding

The findings of this study point to a role for CCT in the folding of both mLST8 and Raptor prior to their assembly into mTOR complexes. This conclusion is supported by several observations. First, the mLST8 β-propeller and the C-terminal β-propeller domain of Raptor bind CCT in immunoprecipitation experiments (**Figures 4.1** and **4.2**). Second, mLST8-CCT and Raptor-CCT complexes can be purified, crosslinked and EM imaged (**Figures 4.1, 4.2, 4.7** and **4.8**). Third, cellular expression of mLST8 and Raptor are decreased upon CCT depletion (**Figure 4.3**). Fourth, assembly of mLST8 and Raptor into mTORC1 and assembly of mLST8 into mTORC2 are inhibited by CCT depletion (**Figure 4.3**). Fifth, insulin signaling downstream of mTORC1 and mTORC2 is diminished in CCT depleted cells (**Figure 4.5**). Collectively, these observations argue that mLST8 and the β-propeller domain of Raptor are CCT folding substrates and that CCT plays an important role in mTORC1 and mTORC2 assembly.

Several aspects of these findings are worth noting. First, in the mTOR complex assembly experiments, mTOR kinase expression was consistently decreased by 20-30 % in CCT depleted cells (**Figure 4.3**), yet we found no interaction between mTOR and CCT in co-immunoprecipitation experiments (data not shown), and mTOR is known to require HSP90 in conjunction with the TTT and R2TP complexes for its folding [157]. This decrease in mTOR expression likely results from the decrease in mLST8 upon CCT depletion because mLST8 has been shown to stabilize the mTOR kinase and increase its cellular expression [110]. Second, the effects of CCT depletion were only partial in both the assembly assays and the insulin signaling experiments, ranging between 30-50 %. These partial effects could be explained by the fact that our CRISPR procedure did not completely remove CCT from the cell population but left approximately 30 % of the CCT complexes intact. This incomplete reduction in CCT stems from the fact that we could not isolate a cell population in which CCT was completely deleted using conventional CRISPR selection methods because CCT is essential for cell survival. Regardless, the effects of partial CCT removal on mLST8 and Raptor were consistent and compelling.

Functional implications of the mLST8-CCT structure

The cryo-EM structure of the mLST8-CCT complex showed mLST8 deep within the CCT folding cavity and binding to CCT subunits on one side of the cavity (**Figure 4.9**). The XL-MS crosslinks confirmed this position of mLST8 and further showed that mLST8 associated with the side of the cavity containing CCTα and CCTγ. The position of mLST8 in the folding cavity is much different from that of the G protein β subunit (Gβ), which has a very similar β-propeller structure (**Figure 4.9 A**). Gβ sits on the same side of the folding cavity as mLST8 in close contact with the CCTα and CCTγ subunits (**Figure 4.9 B**). However, Gβ sits much higher, near the top of the cavity while mLST8 is found at the bottom of the cavity. The positioning of

Gβ high in the cavity is important for its interaction with PhLP1, which has been shown to sit above the folding cavity and bind Gβ, thus stabilizing the Gβ structure and allowing the release of Gβ from CCT [44, 193]. The position of mLST8 deep in the cavity does not permit it to directly bind PhLP1, despite the fact that PhLP1 and mLST8 are found in the same complexes with CCT. Thus, PhLP1 must play a different role in mLST8 folding than it does in Gβ folding.

Another conclusion from the mLST8-CCT structure is that CCT must make very different contacts with mLST8 than it does with Gβ despite the structural similarity between the two proteins. This observation provides further evidence for the diversity of interactions that CCT can employ to bind substrates [161].

Finally, the intra-molecular crosslinks within mLST8 suggest that it has achieved a near-native state in the folding cavity (**Figure 4.9 C**). Interestingly, mLST8 is found on the CCTγ side of the folding cavity. This side of the cavity harbors CCT subunits with weaker ATPase activity, and it has been proposed that substrates are preferentially released from this side of the cavity [194]. Thus, the mLST8 we isolated with CCT may have been in the final stages of folding and ready for release from CCT.

Scheme for CCT-dependent mTOR complex assembly

Based on these results, we can sketch an outline of the contributions of CCT to mTOR complex assembly (**Figure 4.10**). For mTORC1, nascent mLST8 and Raptor subunits interact with CCT and are folded by CCT into their native structures. They are then released from CCT to bind mTOR, which has been folded by the Hsp90-TTT and R2TP complex [157]. For mTORC2, mLST8 is released from CCT to bind mTOR, mSIN1 and Rictor. Whether the mLST8 and Raptor structures are stable after folding by CCT and can diffuse in the cytosol until they locate mTOR or whether other co-chaperones assist in bringing the mTORC subunits together is unknown and deserves further investigation.

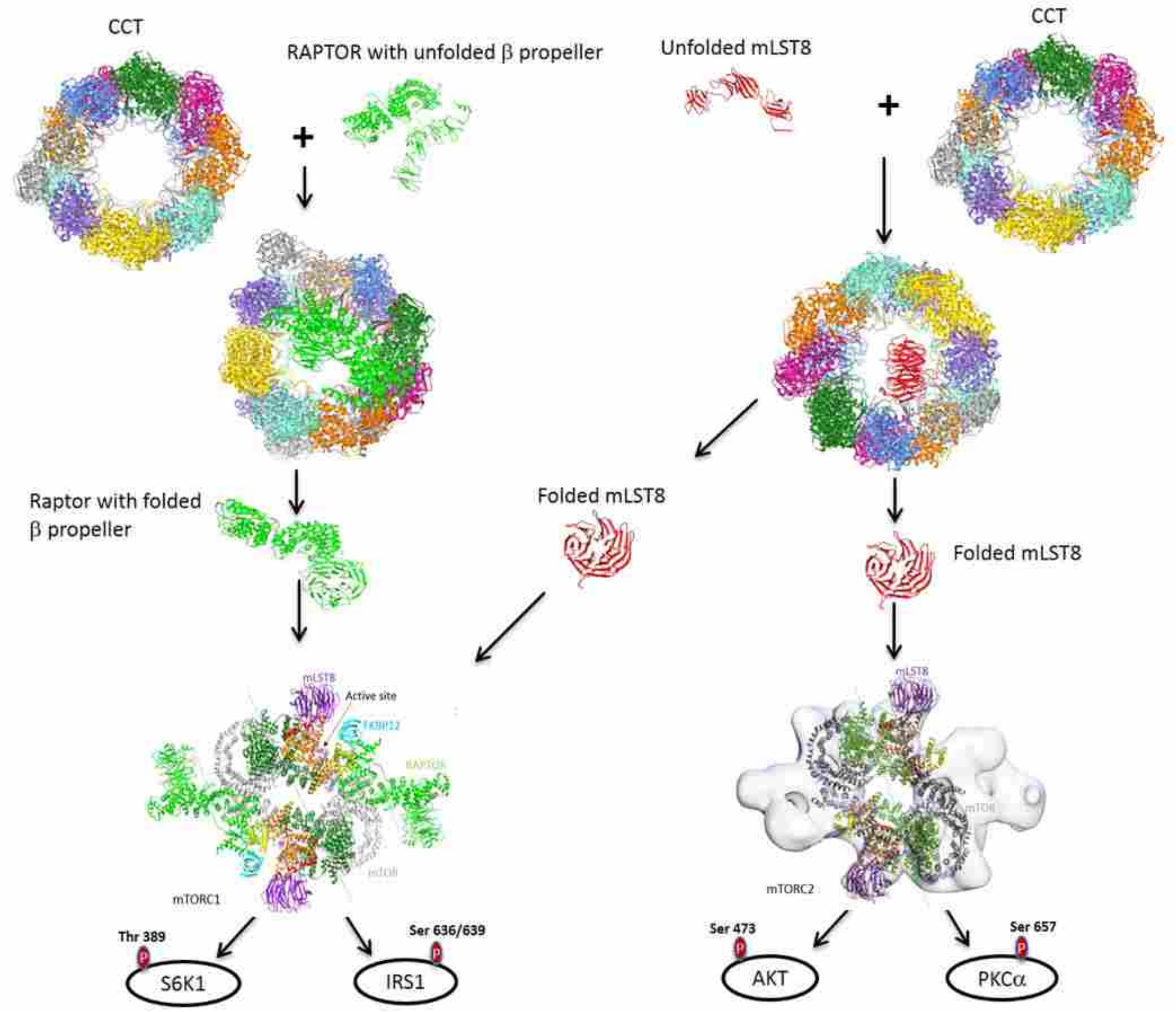

Figure 4.10 CCT contributes to mTOR signaling CCT as a chaperone for mLST8 and Raptor. Formation of both mTORC1 and mTORC2 are assisted by folding function of CCT. Nascent β-propeller of mLST8 or Raptor binds to and folded by CCT prior to mTORCs assembly. Both mLST8 and Raptor are key for proper function in mTOR signaling.

Role of PhLP1 in mLST8 and Raptor folding

The data suggest very different roles for PhLP1 in mLST8 and Raptor folding. With mLST8, the decrease in mLST8 and mTOR expression and assembly (**Figure 4.4**) as well as the decrease in mTORC2 signaling (**Figure 4.5**) upon PhLP1 deletion indicate that PhLP1 assists in mLST8 folding. These effects appear indirect because PhLP1 cannot reach deep into the CCT cavity where mLST8 is located and directly interact with mLST8 (**Figure 4.9**) [44, 193]. In the case of Raptor, the direct binding of PhLP1 to Raptor (**Figure 4.2**) coupled with the increase in Raptor expression and the decrease in Raptor ubiquitination upon PhLP1 deletion (**Figure 4.6**) point to a role for PhLP1 in Raptor degradation. These countervailing effects of PhLP1 on mLST8 and Raptor can explain the lack of effect of PhLP1 depletion on cellular expression of Raptor and association of Raptor with mTOR (**Figure 4.4**). PhLP1 depletion that resulted in decreased mLST8 and mTOR expression would be expected to result in decreased Raptor expression because of loss of its mTORC1 binding partners. However, decreased Raptor ubiquitination and degradation upon PhLP1 depletion would increase Raptor expression. Together, these opposing forces could be the reason for the lack of effect of PhLP1 depletion on Raptor expression and on IRS1 phosphorylation (**Figure 4.5**). IRS1 phosphorylation by mTORC1 depends both on mTOR activity, which decreases upon loss of mLST8 (**Figure 4.5**) [122, 195], and on Raptor recruitment of IRS1 to mTORC1 [196], which would be expected to increase with increased Raptor expression. PhLP1 participation in Raptor ubiquitination represents a new function for PhLP1 and deserves further investigation in the future.

Conclusion

This study establishes a role for CCT in mTOR complex assembly by demonstrating that CCT is required for mLST8 and Raptor folding. The mLST8-CCT structure is the second reported structure of CCT bound to an β-propeller protein, an important class of CCT folding substrates. The structure shows that CCT binds mLST8 at a different location in the folding cavity than Gβ despite their structural similarities, providing additional evidence for the specificity and diversity of substrate binding sites within the CCT folding cavity. The CCT co-chaperone PhLP1, which plays an essential role in Gβ folding and assembly with Gγ, also contributes to mLST8 folding, but by a different mechanism. A new function of PhLP1 in Raptor ubiquitination and degradation was also discovered. These findings provide new insight into the mechanism of mTOR complex assembly and can be used to develop novel pharmacological tools to control mTOR activity and better treat the many diseases associated with aberrant mTOR signaling.

REFERENCES

1. Forsythe, E. and P.L. Beales, *Bardet-Biedl syndrome.* Eur J Hum Genet, 2013. **21**(1): p. 8-13.

2. Katsanis, N., et al., *BBS4 is a minor contributor to Bardet-Biedl syndrome and may also participate in triallelic inheritance.* Am J Hum Genet, 2002. **71**(1): p. 22-9.

3. Beales, P.L., et al., *New criteria for improved diagnosis of Bardet-Biedl syndrome: results of a population survey.* J Med Genet, 1999. **36**(6): p. 437-46.

4. Hernandez-Hernandez, V. and D. Jenkins, *Advances in the understanding of the BBSome complex structure and function.* Research and Reports in Biology, 2015. **6**: p. 191.

5. Tobin, J.L. and P.L. Beales, *Bardet-Biedl syndrome: beyond the cilium.* Pediatr Nephrol, 2007. **22**(7): p. 926-36.

6. Forsythe, E. and P.L. Beales, *Bardet-Biedl Syndrome*, in *GeneReviews(R)*, R.A. Pagon, et al., Editors. 1993: Seattle (WA).

7. Sheffield, V.C., *The blind leading the obese: the molecular pathophysiology of a human obesity syndrome.* Trans Am Clin Climatol Assoc, 2010. **121**: p. 172-81; discussion 181-2.

8. Hooda, A.K., et al., *Renal transplant in a child with Bardet-Biedl syndrome: A rare cause of end-stage renal disease.* Indian J Nephrol, 2009. **19**(3): p. 112-4.

9. O'Dea, D., et al., *The importance of renal impairment in the natural history of Bardet-Biedl syndrome.* Am J Kidney Dis, 1996. **27**(6): p. 776-83.

10. Rathi, M., et al., *Bardet-Biedl syndrome with end-stage kidney disease: A case report and review of literature.* Indian J Nephrol, 2007. **17**: p. 10-3.

11. Mihai, C.M., J.D. Marshall, and R.M. Stoicescu, *Bardet-Biedl syndrome with end-stage kidney disease in a four-year-old Romanian boy: a case report.* J Med Case Rep, 2011. **5**: p. 378.

12. Adams, M., *The Primary Cilium: An Orphan Organelle Finds a Home.* Nature Education, 2010. **3**(9): p. 54.

13. Baker, K. and P.L. Beales, *Making sense of cilia in disease: the human ciliopathies.* Am J Med Genet C Semin Med Genet, 2009. **151C**(4): p. 281-95.

14. Lechtreck, K.F., *IFT-Cargo Interactions and Protein Transport in Cilia.* Trends Biochem Sci, 2015. **40**(12): p. 765-78.

15. Goetz, S.C. and K.V. Anderson, *The primary cilium: a signalling centre during vertebrate development.* Nat Rev Genet, 2010. **11**(5): p. 331-44.

16. Briscoe, J. and P.P. Therond, *The mechanisms of Hedgehog signalling and its roles in development and disease.* Nat Rev Mol Cell Biol, 2013. **14**(7): p. 416-29.

17. Falkenstein, K.N. and S.A. Vokes, *Transcriptional regulation of graded Hedgehog signaling.* Semin Cell Dev Biol, 2014. **33**: p. 73-80.

18. Katoh, Y. and M. Katoh, *Hedgehog target genes: mechanisms of carcinogenesis induced by aberrant hedgehog signaling activation.* Curr Mol Med, 2009. **9**(7): p. 873-86.

19. Seo, S., et al., *A novel protein LZTFL1 regulates ciliary trafficking of the BBSome and Smoothened.* PLoS Genet, 2011. **7**(11): p. e1002358.

20. Zhang, Q., et al., *BBS proteins interact genetically with the IFT pathway to influence SHH-related phenotypes.* Hum Mol Genet, 2012. **21**(9): p. 1945-53.

21. Green, J.A., et al., *Recruitment of beta-Arrestin into Neuronal Cilia Modulates Somatostatin Receptor Subtype 3 Ciliary Localization.* Mol Cell Biol, 2016. **36**(1): p. 223-35.

22. Berbari, N.F., et al., *Bardet-Biedl syndrome proteins are required for the localization of G protein-coupled receptors to primary cilia.* Proc Natl Acad Sci U S A, 2008. **105**(11): p. 4242-6.

23. Domire, J.S., et al., *Dopamine receptor 1 localizes to neuronal cilia in a dynamic process that requires the Bardet-Biedl syndrome proteins.* Cell Mol Life Sci, 2011. **68**(17): p. 2951-60.

24. Green, J.A., C. Gu, and K. Mykytyn, *Heteromerization of ciliary G protein-coupled receptors in the mouse brain.* PLoS One, 2012. **7**(9): p. e46304.

25. Seo, S., et al., *Requirement of Bardet-Biedl syndrome proteins for leptin receptor signaling.* Hum Mol Genet, 2009. **18**(7): p. 1323-31.

26. Datta, P., et al., *Accumulation of non-outer segment proteins in the outer segment underlies photoreceptor degeneration in Bardet-Biedl syndrome.* Proc Natl Acad Sci U S A, 2015. **112**(32): p. E4400-9.

27. Fu, Y., *Phototransduction in Rods and Cones*, in *Webvision: The Organization of the Retina and Visual System*, H. Kolb, E. Fernandez, and R. Nelson, Editors. 1995: Salt Lake City (UT).

28. Yau, K.W. and R.C. Hardie, *Phototransduction motifs and variations.* Cell, 2009. **139**(2): p. 246-64.

29. Eguether, T., et al., *IFT27 links the BBSome to IFT for maintenance of the ciliary signaling compartment.* Dev Cell, 2014. **31**(3): p. 279-90.

30. Nachury, M.V., et al., *A core complex of BBS proteins cooperates with the GTPase Rab8 to promote ciliary membrane biogenesis.* Cell, 2007. **129**(6): p. 1201-13.

31. Ou, G., et al., *Functional coordination of intraflagellar transport motors.* Nature, 2005. **436**(7050): p. 583-7.

32. Chamling, X., et al., *The centriolar satellite protein AZI1 interacts with BBS4 and regulates ciliary trafficking of the BBSome.* PLoS Genet, 2014. **10**(2): p. e1004083.

33. Lechtreck, K.F., et al., *Cycling of the signaling protein phospholipase D through cilia requires the BBSome only for the export phase.* J Cell Biol, 2013. **201**(2): p. 249-61.

34. Liew, G.M., et al., *The intraflagellar transport protein IFT27 promotes BBSome exit from cilia through the GTPase ARL6/BBS3.* Dev Cell, 2014. **31**(3): p. 265-78.

35. Su, X., et al., *Bardet-Biedl syndrome proteins 1 and 3 regulate the ciliary trafficking of polycystic kidney disease 1 protein.* Hum Mol Genet, 2014. **23**(20): p. 5441-51.

36. Yuan, X., R.A. Serra, and S. Yang, *Function and regulation of primary cilia and intraflagellar transport proteins in the skeleton.* Ann N Y Acad Sci, 2015. **1335**: p. 78-99.

37. Sung, C.H. and M.R. Leroux, *The roles of evolutionarily conserved functional modules in cilia-related trafficking.* Nat Cell Biol, 2013. **15**(12): p. 1387-97.

38. Wei, Q., et al., *The BBSome controls IFT assembly and turnaround in cilia.* Nat Cell Biol, 2012. **14**(9): p. 950-7.

39. Lechtreck, K.F., et al., *The Chlamydomonas reinhardtii BBSome is an IFT cargo required for export of specific signaling proteins from flagella.* J Cell Biol, 2009. **187**(7): p. 1117-32.

40. Zhang, Q., et al., *Bardet-Biedl syndrome 3 (Bbs3) knockout mouse model reveals common BBS-associated phenotypes and Bbs3 unique phenotypes.* Proc Natl Acad Sci U S A, 2011. **108**(51): p. 20678-83.

41. Mourao, A., et al., *Structural basis for membrane targeting of the BBSome by ARL6.* Nat Struct Mol Biol, 2014. **21**(12): p. 1035-41.

42. Zhang, Q., et al., *Intrinsic protein-protein interaction-mediated and chaperonin-assisted sequential assembly of stable bardet-biedl syndrome protein complex, the BBSome.* J Biol Chem, 2012. **287**(24): p. 20625-35.

43. Leitner, A., et al., *The molecular architecture of the eukaryotic chaperonin TRiC/CCT.* Structure, 2012. **20**(5): p. 814-25.

44. Plimpton, R.L., et al., *Structures of the Gbeta-CCT and PhLP1-Gbeta-CCT complexes reveal a mechanism for G-protein beta-subunit folding and Gbetagamma dimer assembly.* Proc Natl Acad Sci U S A, 2015. **112**(8): p. 2413-8.

45. Seo, S., et al., *BBS6, BBS10, and BBS12 form a complex with CCT/TRiC family chaperonins and mediate BBSome assembly.* Proc Natl Acad Sci U S A, 2010. **107**(4): p. 1488-93.

46. Yam, A.Y., et al., *Defining the TRiC/CCT interactome links chaperonin function to stabilization of newly made proteins with complex topologies.* Nat Struct Mol Biol, 2008. **15**(12): p. 1255-62.

47. Jin, H., et al., *The conserved Bardet-Biedl syndrome proteins assemble a coat that traffics membrane proteins to cilia.* Cell, 2010. **141**(7): p. 1208-19.

48. Faini, M., et al., *Vesicle coats: structure, function, and general principles of assembly.* Trends Cell Biol, 2013. **23**(6): p. 279-88.

49. Stagg, S.M., et al., *Structure of the Sec13/31 COPII coat cage.* Nature, 2006. **439**(7073): p. 234-8.

50. Harris, J.R. and S. De Carlo, *Negative staining and cryo-negative staining: applications in biology and medicine.* Methods Mol Biol, 2014. **1117**: p. 215-58.

51. Milne, J.L., et al., *Cryo-electron microscopy--a primer for the non-microscopist.* FEBS J, 2013. **280**(1): p. 28-45.

52. Herzog, F., et al., *Structural probing of a protein phosphatase 2A network by chemical cross-linking and mass spectrometry.* Science, 2012. **337**(6100): p. 1348-52.

53. Holding, A.N., *XL-MS: Protein cross-linking coupled with mass spectrometry.* Methods, 2015. **89**: p. 54-63.

54. Leitner, A., et al., *Crosslinking and Mass Spectrometry: An Integrated Technology to Understand the Structure and Function of Molecular Machines.* Trends Biochem Sci, 2016. **41**(1): p. 20-32.

55. Merkley, E.D., et al., *Distance restraints from crosslinking mass spectrometry: mining a molecular dynamics simulation database to evaluate lysine-lysine distances.* Protein Sci, 2014. **23**(6): p. 747-59.

56. Muller, D.R., et al., *Isotope-tagged cross-linking reagents. A new tool in mass spectrometric protein interaction analysis.* Anal Chem, 2001. **73**(9): p. 1927-34.

57. Leitner, A., et al., *Expanding the chemical cross-linking toolbox by the use of multiple proteases and enrichment by size exclusion chromatography.* Mol Cell Proteomics, 2012. **11**(3): p. M111 014126.

58. Leitner, A., et al., *Probing native protein structures by chemical cross-linking, mass spectrometry, and bioinformatics.* Mol Cell Proteomics, 2010. **9**(8): p. 1634-49.

59. Rinner, O., et al., *Identification of cross-linked peptides from large sequence databases.* Nat Methods, 2008. **5**(4): p. 315-8.

60. Chin, J.W., et al., *Addition of a photocrosslinking amino acid to the genetic code of Escherichiacoli.* Proc Natl Acad Sci U S A, 2002. **99**(17): p. 11020-4.

61. Huber, T. and T.P. Sakmar, *Chemical biology methods for investigating G protein-coupled receptor signaling.* Chem Biol, 2014. **21**(9): p. 1224-37.

62. Ray-Saha, S., T. Huber, and T.P. Sakmar, *Antibody epitopes on g protein-coupled receptors mapped with genetically encoded photoactivatable cross-linkers.* Biochemistry, 2014. **53**(8): p. 1302-10.

63. Abe, R., et al., *Mapping ultra-weak protein-protein interactions between heme transporters of Staphylococcus aureus.* J Biol Chem, 2012. **287**(20): p. 16477-87.

64. Gerdes, J.M., E.E. Davis, and N. Katsanis, *The vertebrate primary cilium in development, homeostasis, and disease.* Cell, 2009. **137**(1): p. 32-45.

65. Pearring, J.N., et al., *Protein sorting, targeting and trafficking in photoreceptor cells.* Prog Retin Eye Res, 2013. **36**: p. 24-51.

66. Schou, K.B., L.B. Pedersen, and S.T. Christensen, *Ins and outs of GPCR signaling in primary cilia.* EMBO Rep, 2015. **16**(9): p. 1099-113.

67. Singla, V. and J.F. Reiter, *The primary cilium as the cell's antenna: signaling at a sensory organelle.* Science, 2006. **313**(5787): p. 629-33.

68. Hilgendorf, K.I., C.T. Johnson, and P.K. Jackson, *The primary cilium as a cellular receiver: organizing ciliary GPCR signaling.* Curr Opin Cell Biol, 2016. **39**: p. 84-92.

69. Lancaster, M.A. and J.G. Gleeson, *The primary cilium as a cellular signaling center: lessons from disease.* Curr Opin Genet Dev, 2009. **19**(3): p. 220-9.

70. Jin, H. and M.V. Nachury, *The BBSome.* Curr Biol, 2009. **19**(12): p. R472-3.

71. Novas, R., et al., *Bardet-Biedl syndrome: Is it only cilia dysfunction?* FEBS Lett, 2015. **589**(22): p. 3479-91.

72. Xu, Q., et al., *BBS4 and BBS5 show functional redundancy in the BBSome to regulate the degradative sorting of ciliary sensory receptors.* Sci Rep, 2015. **5**: p. 11855.

73. Katoh, Y., et al., *Architectures of multisubunit complexes revealed by a visible immunoprecipitation assay using fluorescent fusion proteins.* J Cell Sci, 2015. **128**(12): p. 2351-62.

74. Pettersen, E.F., et al., *UCSF Chimera--a visualization system for exploratory research and analysis.* J Comput Chem, 2004. **25**(13): p. 1605-12.

75. Mindell, J.A. and N. Grigorieff, *Accurate determination of local defocus and specimen tilt in electron microscopy.* J Struct Biol, 2003. **142**(3): p. 334-47.

76. Marabini, R., et al., *Xmipp: An Image Processing Package for Electron Microscopy.* J Struct Biol, 1996. **116**(1): p. 237-40.

77. Sorzano, C.O., et al., *A clustering approach to multireference alignment of single-particle projections in electron microscopy.* J Struct Biol, 2010. **171**(2): p. 197-206.

78. Pascual-Montano, A., et al., *A novel neural network technique for analysis and classification of EM single-particle images.* J Struct Biol, 2001. **133**(2-3): p. 233-45.

79. Ludtke, S.J., P.R. Baldwin, and W. Chiu, *EMAN: semiautomated software for high-resolution single-particle reconstructions.* J Struct Biol, 1999. **128**(1): p. 82-97.

80. van Heel, M. and M. Schatz, *Fourier shell correlation threshold criteria.* J Struct Biol, 2005. **151**(3): p. 250-62.

81. Yang, J., et al., *The I-TASSER Suite: protein structure and function prediction.* Nat Methods, 2015. **12**(1): p. 7-8.

82. Biasini, M., et al., *SWISS-MODEL: modelling protein tertiary and quaternary structure using evolutionary information.* Nucleic Acids Res, 2014. **42**(Web Server issue): p. W252-8.

83. Knockenhauer, K.E. and T.U. Schwartz, *Structural Characterization of Bardet-Biedl Syndrome 9 Protein (BBS9).* J Biol Chem, 2015. **290**(32): p. 19569-83.

84. Biasini, M., et al., *SWISS-MODEL: modelling protein tertiary and quaternary structure using evolutionary information.* Nucleic Acids Res, 2014. **42**(Web Server issue): p. W252-8.

85. Sato, S., et al., *Crystallographic study of a site-specifically cross-linked protein complex with a genetically incorporated photoreactive amino acid.* Biochemistry, 2011. **50**(2): p. 250-7.

86. Katsanis, N., et al., *Triallelic inheritance in Bardet-Biedl syndrome, a Mendelian recessive disorder.* Science, 2001. **293**(5538): p. 2256-9.

87. Laurier, V., et al., *Pitfalls of homozygosity mapping: an extended consanguineous Bardet-Biedl syndrome family with two mutant genes (BBS2, BBS10), three mutations, but no triallelism.* Eur J Hum Genet, 2006. **14**(11): p. 1195-203.

88. Beales, P.L., et al., *Genetic interaction of BBS1 mutations with alleles at other BBS loci can result in non-Mendelian Bardet-Biedl syndrome.* Am J Hum Genet, 2003. **72**(5): p. 1187-99.

89. Fauser, S., M. Munz, and D. Besch, *Further support for digenic inheritance in Bardet-Biedl syndrome.* J Med Genet, 2003. **40**(8): p. e104.

90. Deveault, C., et al., *BBS genotype-phenotype assessment of a multiethnic patient cohort calls for a revision of the disease definition.* Hum Mutat, 2011. **32**(6): p. 610-9.

91. Harville, H.M., et al., *Identification of 11 novel mutations in eight BBS genes by high-resolution homozygosity mapping.* J Med Genet, 2010. **47**(4): p. 262-7.

92. Badano, J.L., et al., *Identification of a novel Bardet-Biedl syndrome protein, BBS7, that shares structural features with BBS1 and BBS2.* Am J Hum Genet, 2003. **72**(3): p. 650-8.

93. Najmabadi, H., et al., *Deep sequencing reveals 50 novel genes for recessive cognitive disorders.* Nature, 2011. **478**(7367): p. 57-63.

94. Nishimura, D.Y., et al., *Positional cloning of a novel gene on chromosome 16q causing Bardet-Biedl syndrome (BBS2).* Hum Mol Genet, 2001. **10**(8): p. 865-74.

95. Laplante, M. and D.M. Sabatini, *mTOR signaling at a glance.* J Cell Sci, 2009. **122**(Pt 20): p. 3589-94.

96. Guertin, D.A. and D.M. Sabatini, *Defining the role of mTOR in cancer.* Cancer Cell, 2007. **12**(1): p. 9-22.

97. Yip, C.K., et al., *Structure of the human mTOR complex I and its implications for rapamycin inhibition.* Mol Cell, 2010. **38**(5): p. 768-74.

98. Sarbassov, D.D., et al., *Prolonged rapamycin treatment inhibits mTORC2 assembly and Akt/PKB.* Mol Cell, 2006. **22**(2): p. 159-68.

99. Wullschleger, S., R. Loewith, and M.N. Hall, *TOR signaling in growth and metabolism.* Cell, 2006. **124**(3): p. 471-84.

100. Arias, E., et al., *Lysosomal mTORC2/PHLPP1/Akt Regulate Chaperone-Mediated Autophagy.* Mol Cell, 2015. **59**(2): p. 270-84.

101. Betz, C. and M.N. Hall, *Where is mTOR and what is it doing there?* J Cell Biol, 2013. **203**(4): p. 563-74.

102. Rosner, M. and M. Hengstschlager, *Cytoplasmic and nuclear distribution of the protein complexes mTORC1 and mTORC2: rapamycin triggers dephosphorylation and delocalization of the mTORC2 components rictor and sin1.* Hum Mol Genet, 2008. **17**(19): p. 2934-48.

103. Hoshii, T., et al., *Loss of mTOR complex 1 induces developmental blockage in early T-lymphopoiesis and eradicates T-cell acute lymphoblastic leukemia cells.* Proc Natl Acad Sci U S A, 2014. **111**(10): p. 3805-10.

104. Wei, J., K. Yang, and H. Chi, *Cutting edge: Discrete functions of mTOR signaling in invariant NKT cell development and NKT17 fate decision.* J Immunol, 2014. **193**(9): p. 4297-301.

105. Watanabe, R., L. Wei, and J. Huang, *mTOR signaling, function, novel inhibitors, and therapeutic targets.* J Nucl Med, 2011. **52**(4): p. 497-500.

106. Takai, H., et al., *Tel2 structure and function in the Hsp90-dependent maturation of mTOR and ATR complexes.* Genes Dev, 2010. **24**(18): p. 2019-30.

107. Baretic, D., et al., *Tor forms a dimer through an N-terminal helical solenoid with a complex topology.* Nat Commun, 2016. **7**: p. 11016.

108. Melero, R., et al., *Structures of SMG1-UPFs complexes: SMG1 contributes to regulate UPF2-dependent activation of UPF1 in NMD.* Structure, 2014. **22**(8): p. 1105-19.

109. Perry, J. and N. Kleckner, *The ATRs, ATMs, and TORs are giant HEAT repeat proteins.* Cell, 2003. **112**(2): p. 151-5.

110. Yang, H., et al., *mTOR kinase structure, mechanism and regulation.* Nature, 2013. **497**(7448): p. 217-23.

111. Aylett, C.H., et al., *Architecture of human mTOR complex 1.* Science, 2016. **351**(6268): p. 48-52.

112. Gaubitz, C., et al., *TORC2 Structure and Function.* Trends Biochem Sci, 2016. **41**(6): p. 532-45.

113. Magnuson, B., B. Ekim, and D.C. Fingar, *Regulation and function of ribosomal protein S6 kinase (S6K) within mTOR signalling networks.* Biochem J, 2012. **441**(1): p. 1-21.

114. Acosta-Jaquez, H.A., et al., *Site-specific mTOR phosphorylation promotes mTORC1-mediated signaling and cell growth.* Mol Cell Biol, 2009. **29**(15): p. 4308-24.

115. Ekim, B., et al., *mTOR kinase domain phosphorylation promotes mTORC1 signaling, cell growth, and cell cycle progression.* Mol Cell Biol, 2011. **31**(14): p. 2787-801.

116. Cheng, S.W., et al., *Thr2446 is a novel mammalian target of rapamycin (mTOR) phosphorylation site regulated by nutrient status.* J Biol Chem, 2004. **279**(16): p. 15719-22.

117. Holz, M.K. and J. Blenis, *Identification of S6 kinase 1 as a novel mammalian target of rapamycin (mTOR)-phosphorylating kinase.* J Biol Chem, 2005. **280**(28): p. 26089-93.

118. Copp, J., G. Manning, and T. Hunter, *TORC-specific phosphorylation of mammalian target of rapamycin (mTOR): phospho-Ser2481 is a marker for intact mTOR signaling complex 2.* Cancer Res, 2009. **69**(5): p. 1821-7.

119. Soliman, G.A., et al., *mTOR Ser-2481 autophosphorylation monitors mTORC-specific catalytic activity and clarifies rapamycin mechanism of action.* J Biol Chem, 2010. **285**(11): p. 7866-79.

120. Miller, S., et al., *Shaping development of autophagy inhibitors with the structure of the lipid kinase Vps34.* Science, 2010. **327**(5973): p. 1638-42.

121. Walker, E.H., et al., *Structural insights into phosphoinositide 3-kinase catalysis and signalling.* Nature, 1999. **402**(6759): p. 313-20.

122. Kim, D.H., et al., *GbetaL, a positive regulator of the rapamycin-sensitive pathway required for the nutrient-sensitive interaction between raptor and mTOR.* Mol Cell, 2003. **11**(4): p. 895-904.

123. Kakumoto, K., et al., *mLST8 Promotes mTOR-Mediated Tumor Progression.* PLoS One, 2015. **10**(4): p. e0119015.

124. Guertin, D.A., et al., *Ablation in mice of the mTORC components raptor, rictor, or mLST8 reveals that mTORC2 is required for signaling to Akt-FOXO and PKCalpha, but not S6K1.* Dev Cell, 2006. **11**(6): p. 859-71.

125. Kim, D.H., et al., *mTOR interacts with raptor to form a nutrient-sensitive complex that signals to the cell growth machinery.* Cell, 2002. **110**(2): p. 163-75.

126. Wiza, C., E.B. Nascimento, and D.M. Ouwens, *Role of PRAS40 in Akt and mTOR signaling in health and disease.* Am J Physiol Endocrinol Metab, 2012. **302**(12): p. E1453-60.

127. Zoncu, R., A. Efeyan, and D.M. Sabatini, *mTOR: from growth signal integration to cancer, diabetes and ageing.* Nat Rev Mol Cell Biol, 2011. **12**(1): p. 21-35.

128. Zhou, P., et al., *Defining the Domain Arrangement of the Mammalian Target of Rapamycin Complex Component Rictor Protein.* J Comput Biol, 2015. **22**(9): p. 876-86.

129. Yuan, Y., et al., *Characterization of Sin1 Isoforms Reveals an mTOR-Dependent and Independent Function of Sin1gamma.* PLoS One, 2015. **10**(8): p. e0135017.

130. Cameron, A.J., et al., *mTORC2 targets AGC kinases through Sin1-dependent recruitment.* Biochem J, 2011. **439**(2): p. 287-97.

131. Cheng, J., et al., *Mip1, an MEKK2-interacting protein, controls MEKK2 dimerization and activation.* Mol Cell Biol, 2005. **25**(14): p. 5955-64.

132. Liu, P., et al., *PtdIns(3,4,5)P3-Dependent Activation of the mTORC2 Kinase Complex.* Cancer Discov, 2015. **5**(11): p. 1194-209.

133. Schroder, W., G. Bushell, and T. Sculley, *The human stress-activated protein kinase-interacting 1 gene encodes JNK-binding proteins.* Cell Signal, 2005. **17**(6): p. 761-7.

134. Laplante, M. and D.M. Sabatini, *mTOR signaling in growth control and disease.* Cell, 2012. **149**(2): p. 274-93.

135. Castilho, R.M., et al., *mTOR mediates Wnt-induced epidermal stem cell exhaustion and aging.* Cell Stem Cell, 2009. **5**(3): p. 279-89.

136. Ma, L., et al., *Phosphorylation and functional inactivation of TSC2 by Erk implications for tuberous sclerosis and cancer pathogenesis.* Cell, 2005. **121**(2): p. 179-93.

137. Populo, H., J.M. Lopes, and P. Soares, *The mTOR signalling pathway in human cancer.* Int J Mol Sci, 2012. **13**(2): p. 1886-918.

138. Groenewoud, M.J. and F.J. Zwartkruis, *Rheb and Rags come together at the lysosome to activate mTORC1.* Biochem Soc Trans, 2013. **41**(4): p. 951-5.

139. Dibble, C.C. and L.C. Cantley, *Regulation of mTORC1 by PI3K signaling.* Trends Cell Biol, 2015. **25**(9): p. 545-55.

140. Martin, D., et al., *Accumulation of dephosphorylated 4EBP after mTOR inhibition with rapamycin is sufficient to disrupt paracrine transformation by the KSHV vGPCR oncogene.* Oncogene, 2014. **33**(18): p. 2405-12.

141. Ali, S.M. and D.M. Sabatini, *Structure of S6 kinase 1 determines whether raptor-mTOR or rictor-mTOR phosphorylates its hydrophobic motif site.* J Biol Chem, 2005. **280**(20): p. 19445-8.

142. Dennis, P.B., et al., *Mammalian TOR: a homeostatic ATP sensor.* Science, 2001. **294**(5544): p. 1102-5.

143. DeYoung, M.P., et al., *Hypoxia regulates TSC1/2-mTOR signaling and tumor suppression through REDD1-mediated 14-3-3 shuttling.* Genes Dev, 2008. **22**(2): p. 239-51.

144. Feng, Z., et al., *The regulation of AMPK beta1, TSC2, and PTEN expression by p53: stress, cell and tissue specificity, and the role of these gene products in modulating the IGF-1-AKT-mTOR pathways.* Cancer Res, 2007. **67**(7): p. 3043-53.

145. Hardie, D.G., *AMP-activated/SNF1 protein kinases: conserved guardians of cellular energy.* Nat Rev Mol Cell Biol, 2007. **8**(10): p. 774-85.

146. Charest, P.G., et al., *A Ras signaling complex controls the RasC-TORC2 pathway and directed cell migration.* Dev Cell, 2010. **18**(5): p. 737-49.

147. Chen, C.H., et al., *Autoregulation of the mechanistic target of rapamycin (mTOR) complex 2 integrity is controlled by an ATP-dependent mechanism.* J Biol Chem, 2013. **288**(38): p. 27019-30.

148. Chen, C.H., et al., *ER stress inhibits mTORC2 and Akt signaling through GSK-3beta-mediated phosphorylation of rictor.* Sci Signal, 2011. **4**(161): p. ra10.

149. Humphrey, S.J., et al., *Dynamic adipocyte phosphoproteome reveals that Akt directly regulates mTORC2.* Cell Metab, 2013. **17**(6): p. 1009-20.

150. Treins, C., et al., *Rictor is a novel target of p70 S6 kinase-1.* Oncogene, 2010. **29**(7): p. 1003-16.

151. Gan, X., et al., *Evidence for direct activation of mTORC2 kinase activity by phosphatidylinositol 3,4,5-trisphosphate.* J Biol Chem, 2011. **286**(13): p. 10998-1002.

152. Heikamp, E.B., et al., *The AGC kinase SGK1 regulates TH1 and TH2 differentiation downstream of the mTORC2 complex.* Nat Immunol, 2014. **15**(5): p. 457-64.

153. Sarbassov, D.D., et al., *Rictor, a novel binding partner of mTOR, defines a rapamycin-insensitive and raptor-independent pathway that regulates the cytoskeleton.* Curr Biol, 2004. **14**(14): p. 1296-302.

154. Goschzik, T., et al., *PTEN mutations and activation of the PI3K/Akt/mTOR signaling pathway in papillary tumors of the pineal region.* J Neuropathol Exp Neurol, 2014. **73**(8): p. 747-51.

155. Kim, Y.E., et al., *Molecular chaperone functions in protein folding and proteostasis.* Annu Rev Biochem, 2013. **82**: p. 323-55.

156. David-Morrison, G., et al., *WAC Regulates mTOR Activity by Acting as an Adaptor for the TTT and Pontin/Reptin Complexes.* Dev Cell, 2016. **36**(2): p. 139-51.

157. Pal, M., et al., *Structural basis for phosphorylation-dependent recruitment of Tel2 to Hsp90 by Pih1.* Structure, 2014. **22**(6): p. 805-18.

158. Camasses, A., et al., *The CCT chaperonin promotes activation of the anaphase-promoting complex through the generation of functional Cdc20.* Mol Cell, 2003. **12**(1): p. 87-100.

159. Miyata, Y., et al., *The molecular chaperone TRiC/CCT binds to the Trp-Asp 40 (WD40) repeat protein WDR68 and promotes its folding, protein kinase DYRK1A binding, and nuclear accumulation.* J Biol Chem, 2014. **289**(48): p. 33320-32.

160. Valpuesta, J.M., et al., *Structure and function of a protein folding machine: the eukaryotic cytosolic chaperonin CCT.* FEBS Lett, 2002. **529**(1): p. 11-6.

161. Willardson, B.M. and C.M. Tracy, *Chaperone-mediated assembly of G protein complexes.* Subcell Biochem, 2012. **63**: p. 131-53.

162. Kabir, M.A., et al., *Physiological effects of unassembled chaperonin Cct subunits in the yeast Saccharomyces cerevisiae.* Yeast, 2005. **22**(3): p. 219-39.

163. Behrends, C., et al., *Network organization of the human autophagy system.* Nature, 2010. **466**(7302): p. 68-76.

164. Abe, Y., et al., *p90 ribosomal S6 kinase and p70 ribosomal S6 kinase link phosphorylation of the eukaryotic chaperonin containing TCP-1 to growth factor, insulin, and nutrient signaling.* J Biol Chem, 2009. **284**(22): p. 14939-48.

165. Joachimiak, L.A., et al., *The structural basis of substrate recognition by the eukaryotic chaperonin TRiC/CCT.* Cell, 2014. **159**(5): p. 1042-55.

166. Bouhouche, A., et al., *Mutation in the epsilon subunit of the cytosolic chaperonin-containing t-complex peptide-1 (Cct5) gene causes autosomal recessive mutilating sensory neuropathy with spastic paraplegia.* J Med Genet, 2006. **43**(5): p. 441-3.

167. Minegishi, Y., et al., *CCT2 Mutations Evoke Leber Congenital Amaurosis due to Chaperone Complex Instability.* Sci Rep, 2016. **6**: p. 33742.

168. Feldman, D.E., et al., *Tumorigenic mutations in VHL disrupt folding in vivo by interfering with chaperonin binding.* Mol Cell, 2003. **12**(5): p. 1213-24.

169. Kasembeli, M., et al., *Modulation of STAT3 folding and function by TRiC/CCT chaperonin.* PLoS Biol, 2014. **12**(4): p. e1001844.

170. Tracy, C.M., et al., *Programmed cell death protein 5 interacts with the cytosolic chaperonin containing tailless complex polypeptide 1 (CCT) to regulate beta-tubulin folding.* J Biol Chem, 2014. **289**(7): p. 4490-502.

171. Trinidad, A.G., et al., *Interaction of p53 with the CCT complex promotes protein folding and wild-type p53 activity.* Mol Cell, 2013. **50**(6): p. 805-17.

172. Arndt, V., et al., *Chaperone-assisted selective autophagy is essential for muscle maintenance.* Curr Biol, 2010. **20**(2): p. 143-8.

173. Arndt, V., C. Rogon, and J. Hohfeld, *To be, or not to be--molecular chaperones in protein degradation.* Cell Mol Life Sci, 2007. **64**(19-20): p. 2525-41.

174. Yokota, S., et al., *Proteasome-dependent degradation of cytosolic chaperonin CCT.* Biochem Biophys Res Commun, 2000. **279**(2): p. 712-7.

175. Zhang, T., et al., *Global Analysis of Cellular Protein Flux Quantifies the Selectivity of Basal Autophagy.* Cell Rep, 2016. **14**(10): p. 2426-39.

176. Kubota, H., G. Hynes, and K. Willison, *The chaperonin containing t-complex polypeptide 1 (TCP-1). Multisubunit machinery assisting in protein folding and assembly in the eukaryotic cytosol.* Eur J Biochem, 1995. **230**(1): p. 3-16.

177. Zhang, J., et al., *Mechanism of folding chamber closure in a group II chaperonin.* Nature, 2010. **463**(7279): p. 379-83.

178. Tang, Y.C., et al., *Essential role of the chaperonin folding compartment in vivo.* EMBO J, 2008. **27**(10): p. 1458-68.

179. Reissmann, S., et al., *A gradient of ATP affinities generates an asymmetric power stroke driving the chaperonin TRIC/CCT folding cycle.* Cell Rep, 2012. **2**(4): p. 866-77.

180. Willardson, B.M. and A.C. Howlett, *Function of phosducin-like proteins in G protein signaling and chaperone-assisted protein folding.* Cell Signal, 2007. **19**(12): p. 2417-27.

181. Lukov, G.L., et al., *Mechanism of assembly of G protein betagamma subunits by protein kinase CK2-phosphorylated phosducin-like protein and the cytosolic chaperonin complex.* J Biol Chem, 2006. **281**(31): p. 22261-74.

182. Lukov, G.L., et al., *Phosducin-like protein acts as a molecular chaperone for G protein betagamma dimer assembly.* EMBO J, 2005. **24**(11): p. 1965-75.

183. Sarbassov, D.D. and D.M. Sabatini, *Redox regulation of the nutrient-sensitive raptor-mTOR pathway and complex.* J Biol Chem, 2005. **280**(47): p. 39505-9.

184. Sengupta, S., T.R. Peterson, and D.M. Sabatini, *Regulation of the mTOR complex 1 pathway by nutrients, growth factors, and stress.* Mol Cell, 2010. **40**(2): p. 310-22.

185. Hendrick, J.P. and F.U. Hartl, *The role of molecular chaperones in protein folding.* FASEB J, 1995. **9**(15): p. 1559-69.

186. Hay, N. and N. Sonenberg, *Upstream and downstream of mTOR.* Genes Dev, 2004. **18**(16): p. 1926-45.

187. Scheres, S.H., et al., *Maximum-likelihood multi-reference refinement for electron microscopy images.* J Mol Biol, 2005. **348**(1): p. 139-49.

188. Frank, J., et al., *SPIDER and WEB: processing and visualization of images in 3D electron microscopy and related fields.* J Struct Biol, 1996. **116**(1): p. 190-9.

189. Thulin, C.D., et al., *The immunolocalization and divergent roles of phosducin and phosducin-like protein in the retina.* Mol Vis, 1999. **5**: p. 40.

190. Munoz, I.G., et al., *Crystal structure of the open conformation of the mammalian chaperonin CCT in complex with tubulin.* Nat Struct Mol Biol, 2011. **18**(1): p. 14-9.

191. Kalisman, N., G.F. Schroder, and M. Levitt, *The crystal structures of the eukaryotic chaperonin CCT reveal its functional partitioning.* Structure, 2013. **21**(4): p. 540-9.

192. Martin-Benito, J., et al., *Structure of the complex between the cytosolic chaperonin CCT and phosducin-like protein.* Proc Natl Acad Sci U S A, 2004. **101**(50): p. 17410-5.

193. Martín-Benito, J., et al., *Structure of the complex between the cytosolic chaperonin CCT and phosducin-like protein.* Proc Natl Acad Sci U.S.A., 2004. **101**: p. 17410-17415.

194. Lopez, T., K. Dalton, and J. Frydman, *The Mechanism and Function of Group II Chaperonins.* J Mol Biol, 2015. **427**(18): p. 2919-30.

195. Chen, E.J. and C.A. Kaiser, *LST8 negatively regulates amino acid biosynthesis as a component of the TOR pathway.* J Cell Biol, 2003. **161**(2): p. 333-47.

196. Tzatsos, A., *Raptor binds the SAIN (Shc and IRS-1 NPXY binding) domain of insulin receptor substrate-1 (IRS-1) and regulates the phosphorylation of IRS-1 at Ser-636/639 by mTOR.* J Biol Chem, 2009. **284**(34): p. 22525-34.